공학박사 학위논문

불평형 그리드전압 상태에서 교류-직류 변환 매트릭스컨버터의 고성능 제어기법

Advanced Control Strategies for AC-DC Matrix Converter under Unbalanced Grid Voltage Conditions

울산대학교 대학원

전기공학부

NGUYEN THANH LUAN

공학박사 학위논문

불평형 그리드전압 상태에서 교류-직류 변환 매트릭스컨버터의 고성능 제어기법

Advanced Control Strategies for AC-DC Matrix Converter under Unbalanced Grid Voltage Conditions

지도교수 이홍희

이 논문을 공학박사 학위논문으로 제출함

2020 년 12 월

울산대학교 대학원

전기공학부

NGUYEN THANH LUAN

NGUYEN THANH LUAN 의 공학박사위 논문을 인준함

심사위원장	전태원	(인)
심사위원	이홍희	(인)
심사위원	최성진	(인)
심사위원	이동춘	(인)
심사위원	정의헌	(인)

울산대학교 대학원

2020 년 12 월

UNIVERSITY OF ULSAN

Advanced Control Strategies for AC-DC Matrix Converter under Unbalanced Grid Voltage Conditions

by

NGUYEN THANH LUAN

A dissertation submitted in partial fulfillment of the requirements for

the degree of Doctor of Philosophy

in the

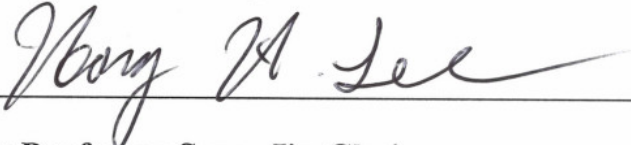School of Electrical Engineering

University of Ulsan

December 2020

This certifies that the dissertation of NGUYEN THANH LUAN is approved by:

Committee Chair: **Professor Tae-Won Chun**

Signature:

Committee Member: **Professor Hong-Hee Lee**

Signature:

Committee Member: **Professor Sung-Jin Choi**

Signature:

Committee Member: **Professor Dong-Choon Lee**

Signature:

Committee Member: **Doctor Eui-Heon Jung**

Signature:

School of Electrical Engineering

University of Ulsan

December 2020

I would like to dedicate this dissertation to my beloved parents, my sister and my lovely girlfriend:

Nguyễn Tiến Thăng
Đinh Thị Viễn
Nguyễn Thị Thuý Quỳnh
Phạm Thị Huế

Acknowledgements

First of all, I would like to respectfully thank to my supervisor, Professor Hong-Hee Lee for his valuable guidance, encouragement and support during my Ph.D. study at the University of Ulsan. It has been my great happiness to complete my Ph.D study under his guidance.

I would like to express my sincere thanks to my thesis committee members: Professor Tae-Won Chun (University of Ulsan), Professor Sung-Jin Choi (University of Ulsan), Professor Dong-Choon Lee (Yeungnam University), and Dr. Eui-Heon Jung (University of Ulsan) for their valuable time, insightful comments and suggestions on my Ph.D thesis.

I would like to thank all Professors in University of Ulsan for their lectures and supports during my courses.

I express my grateful for the financial supports of Brain Korea 21 Plus (BK21+) and Network-based Automation Research Center (NARC).

I would like to express my warm gratitude to my labmates in the Industrial Networks and Power Electronics Laboratory (INPEL) for the useful discussions, encouragement, help, and memorable moments during the course of my study.

Last but not least, I would like to thank my beloved parents, my sister, my lovely girlfriend, and all my relatives for their encouragement, support, and love.

Ulsan, December 2020

Nguyen Thanh Luan

Abstract

In recent years, AC-DC Matrix Converters (MCs) have received much interest in research for AC-DC power conversion due to its significant advantages such as bidirectional power flow, sinusoidal grid current, controllable input power factor, tight DC voltage regulation over a wide range, compact design, and long life. All of these advantages make AC-DC MCs promising for industrial applications such as energy storage systems, AC-DC microgrids, and vehicle-to-grid systems. In practical applications, the three-phase grid voltage are often under unbalanced conditions, which deteriorate the performance of the AC-DC MCs due to the ripple on the DC side and low-order harmonics in the grid current.

This thesis presents the development of various advanced control strategies based on space vector modulation (SVM) and model predictive control (MPC) to drive the AC-DC MCs under unbalanced conditions with high performance in term of the output current and voltage ripples, grid current harmonics, and grid power factor. The first approach is based on the SVM technique; an enhanced control strategy is developed based on an independent control scheme for the active and reactive powers. The input current reference is directly synthesized from instantaneous power analysis in a stationary frame, and a constant DC voltage and current and a sinusoidal grid current are obtained without any input current controller. Additionally, a near unity power factor is simply achieved by using an average grid reactive power-based PI controller. The average grid reactive power is obtained through a notch filter without using the grid voltage sequence components, so the proposed control strategy is implemented easily without large storage requirement.

The second approach is based on the MPC technique. MPC is applied to AC-DC MCs to achieve fast dynamic response and simple implementation. In spite of these advantages, the conventional MPC (C-MPC) for an AC-DC MC still has various issues to be solved. This thesis present three advanced MPC schemes to deal with various issues of the C-MPC such as computational burden, active damping function, steady state performance improvement, and voltage sensor reduction. First, the thesis presents a simplified MPC (S-MPC) scheme with active damping function. The grid current reference is generated by analyzing the instantaneous power model in a stationary frame without information about the grid voltage sequence components. The prediction process is simplified by computing only one required

input current vector (RICV) instead of nine grid current predictions. In addition, a novel method is proposed to realize the active damping function without increasing the computational burden by integrating the damping current into the RICV. Thus, the execution time of the S-MPC is significantly reduced compared with that of the C-MPC, and the system performance is easily improved by shortening the sampling period.

Second, a virtual-flux-based MPC (VF-MPC) scheme is developed to remove the grid voltage sensor and enhance the grid current performance. By modeling the power flow in terms of the virtual flux (VF) and its 90° lagging signal, the grid current reference and grid voltage are obtained simply without the extraction of the VF positive and negative sequence components. Furthermore, the number of current vectors is increased from 9 to 39 vectors by generating 30 virtual current vectors to minimize the grid current tracking error. Especially, to reduce the computational burden due to the increased number of current vectors, a preselection method is presented to reduce the number of candidate current vectors from 39 to 8.

Third, the thesis develops an improved MPC (I-MPC) scheme to simultaneously compensate the power ripple in the input filter and reduce the grid current distortion by taking into account the power ripple in the input filter under unbalanced grid voltage conditions, which is normally ignored in the MPC of an AC-DC MC. The power ripple is calculated based on the grid voltage and its 90° lagging signal, which makes the implementation simple without grid voltage components extraction or digital filter design. Furthermore, a closed-loop current controller is developed based on a resonant controller (RC) to reduce the grid current harmonic caused by power ripple under imbalanced grid voltage conditions.

All control strategies are successfully tested by simulation in PSIM and experiments on prototype AC-DC MC. Proper comparisons are also given to verify the effectiveness of the proposed control strategies.

Contents

List of Figures

List of Tables

Abbreviations

AC	Alternating Current
BESS	Battery Energy Storage System
C-MPC	Conventional-Model Predictive Control
DC	Direct Current
ECS-PFC	Enhanced Control Strategy-Power Factor Control
EV	Electric Vehicle
FFT	Fast Fourier Transform
HFT	High-Frequency Transformer
IGBT	Insulated-Gate Bipolar Transistor
I-MPC	Improved-Model Predictive Control
IPF	Input Power Factor
LPF	Low-Pass Filter
MC	Matrix Converter
MOSFET	Metal Oxide Silicon Field Effect Transistor
MPC	Model Predictive Control
PI	Proportional Integral
PLL	Phase-Locked Loop
P-NSC	Positive-Negative Sequence Component
RC	Resonant Controller
RICV	Required Input Current Vector
RMS	Root Mean Squared
SMC	Sliding Mode Control
S-MPC	Simplified-Model Predictive Control
SOGI	Second-Order Generalized Integrator
SVM	Space Vector Modulation
THD	Total Harmonic Distortion
V2G	Vehicle-to-Grid
VF	Virtual Flux
VF-MPC	Virtual Flux-Model Predictive Control
VSC	Voltage Source Converter
VVVF	Variable Voltage Variable Frequency

Nomenclatures

$\mathbf{v_s}, \mathbf{v_i}$	Grid and input voltage vectors
v_s, v_i	Instantaneous grid and input phase voltages
V_{sm}, V_{im}	Grid and input voltage amplitudes
f_i, ω	Grid frequency and grid angular frequency
$\mathbf{i_s}, \mathbf{i_i}$	Grid and input current vector
i_s, i_i	Instantaneous grid and input currents
i_{dc}, v_o	Output current and voltage of AC-DC MC
v_{dc}	Instantaneous voltage of DC load
V_{DC}	Rated voltage of DC load
$I_{dc}^{ref}, V_{dc}^{ref}$	References of output current and DC load voltage
m_i	Modulation index of SVM
φ_v, φ_i	Phase angle of grid voltage and current
φ_{vi}	Input power factor angle
$\mathbf{\psi_s}$	Grid virtual flux vector
ψ_s	Instantaneous grid virtual flux
p_s, q_s	Instantaneous grid active and reactive powers
p_i, q_i	Instantaneous input active and reactive powers
P_0, Q_0	Average values of active and reactive powers
$P_{c2}, P_{s2}, Q_{c2}, Q_{s2}$	Ripple components of active and reactive powers
P_{dc}	Output power
$\mathbf{S}$	Switching matrix
S_{xy}	State of bidirectional switch
L_f, C_f, R_f	Input filter parameters
R_d	Virtual damping resistor
$\mathbf{i_{damp}}$	Damping current vector
$\mathbf{i_C}$	Input capacitor current vector
L	Output inductor filter
R	Output resistor load
η	Converter efficiency

f_s	Switching frequency of SVM
T_s	Sampling period
λ	Weighting factor of MPC
f_{avg}	Average switching frequency of MPC
P_{sw}	Switching loss
D	Modulation vector

Superscripts

ref	Reference values
*	Conjugate of a complex vector
'	90 electrical degrees delay signal
.	Differential operator in time domain
h	Harmonic component

Subscripts

a,b,c	Three phase stationary axes
α,β	αβ stationary axes
p,n	Positive and negative sequence components

Chapter 1

Introduction

1.1 AC-DC Matrix Converter, State of the Art

The bidirectional AC-DC converter is an essential part of various emerging applications, such as battery energy storage systems (BESS) [1], [2], chargers for electric vehicles (EVs) [3], [4], uninterruptible power supplies (UPS) [5], hybrid AC-DC microgrids [6], and vehicle-to-grid (V2G) systems [7]. Voltage source converters (VSCs) are commonly used, which have advantages of bidirectional power flow, sinusoidal grid current, controllable power factor, and tight DC voltage regulation capability. However, VSCs have an inherent limitation in that the DC voltage must be higher than the peak AC voltage. For many applications, the DC voltage is generally below the peak AC voltage and may vary over a wide range. Therefore, an additional bidirectional DC-DC converter stage is needed to match the desired DC bus voltage as shown in Figure 1.1. However, this two-stage power conversion increases the weight and cost while reducing the efficiency of the converter system [4], [8]. Furthermore, the reliability and power density of the VSCs are poor due to the bulky electrolytic capacitor across the DC bus [9].

To overcome these drawbacks, the AC-DC matrix converter (MC) was introduced as a bidirectional single-stage converter without any intermediate energy storage element [10]. The topology of an AC-DC MC is shown in Figure 1.2. It provides many advantages such as sinusoidal grid current, controllable power factor, compact design, and long life [11], [12]. The AC-DC MC also provides direct input current synthesis and tight DC voltage regulation over a wide range. Thus, for applications with low DC voltage, the AC-DC MC is an
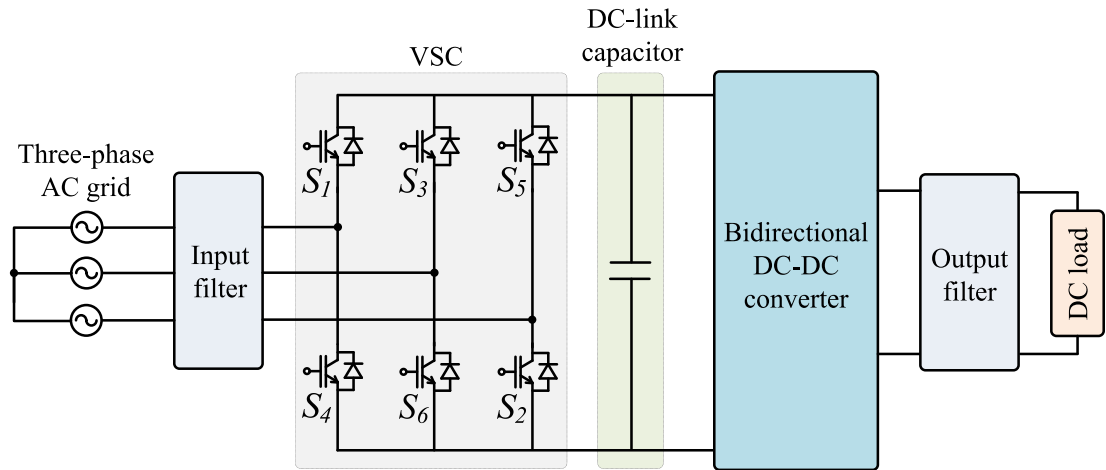
Figure 1.1 Two-stage bidirectional AC-DC power conversion based on VSC.
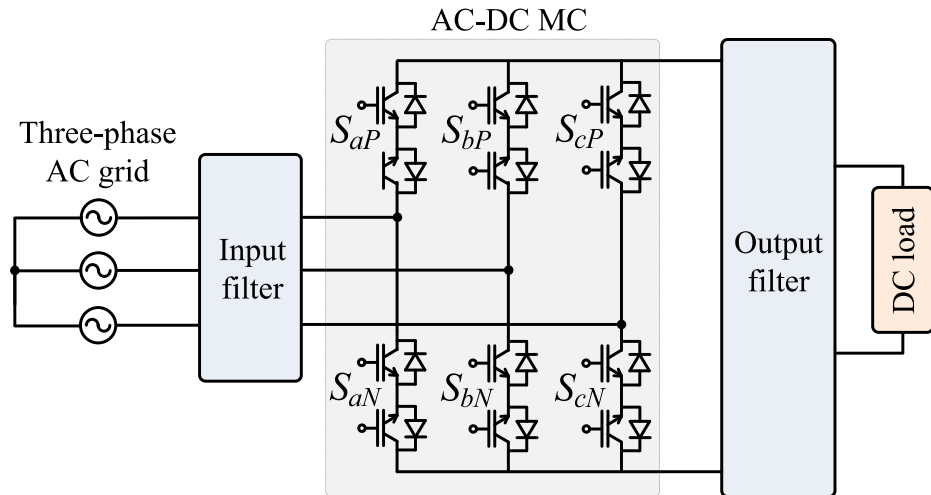
Figure 1.2 Single-stage bidirectional AC-DC power conversion based on AC-DC MC.

attractive alternative to VSC-based topologies [13], [14].

1.2 Review of AC-DC MC Developments

MCs are one of the most interesting families of converters [15]. The primary base of MC theories was initially proposed by Gyugyi and Pelly in 1976 [16]. However, the intensive research on MCs starts with the work of Venturini and Alesina in 1980 [17], [18]. They presented the power circuit that enables AC-AC power conversion without any intermediate energy storage element by employing a converter as a matrix of bidirectional power
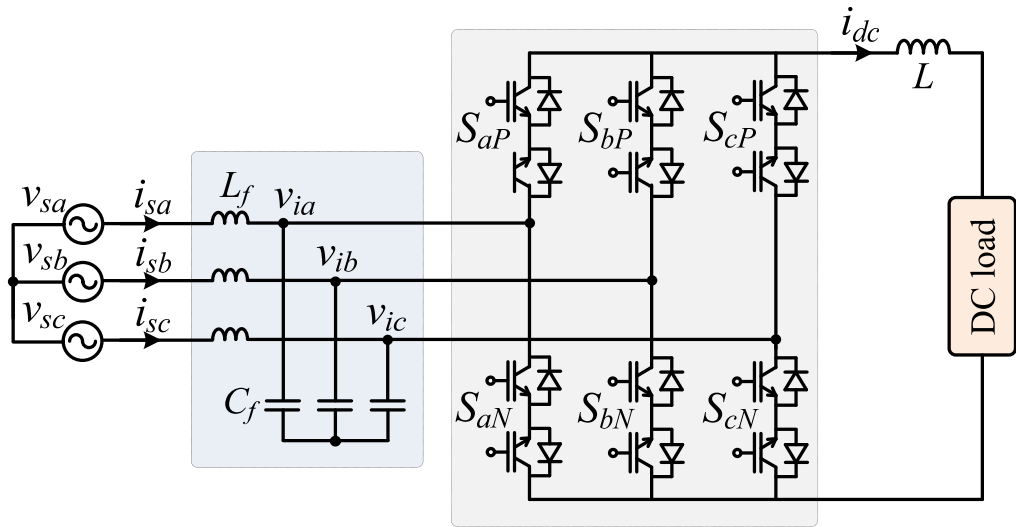
Figure 1.3 Topology of an AC-DC MC

switches and they introduced the name "matrix converter." In 1992, the AC-DC MC was first derived by Holmes and Lipo based on reduction from three-to-three phase MC to three-to-one phase MC to realize the bidirectional AC-DC power conversion [10]. During the last decades, AC-DC MC has received considerable interest in research due to its significant advantages. The research on the AC-DC MC is mainly focused on topology development, modulation and control methods, operation under abnormal conditions.

1.2.1 AC-DC MC-based Topologies

The conventional topology of an AC-DC MC with a second-order LC input filter and an output filter L is shown in Figure 1.3 [11]–[14], [19]–[21]. The power circuit consists of six bidirectional switches; it realizes the AC-DC buck conversion and DC-AC boost conversion. This topology was widely applied for applications where the low and variable DC voltage is required such as V2G [13], [14], BESS [20], [21].

For lower output voltage, the conventional AC-DC MC must be operated at lower modulation index which in turn increases switch RMS current and reduces power conversion efficiency. To solve this problem, the AC-DC MC followed by a current doubler rectifier (CDR) is realized as shown in Figure 1.4 [22]. For the same modulation index, this topology reduces the output DC voltage by half of the voltage gain achieved by the conventional AC-DC MC without compromising the input power quality and power
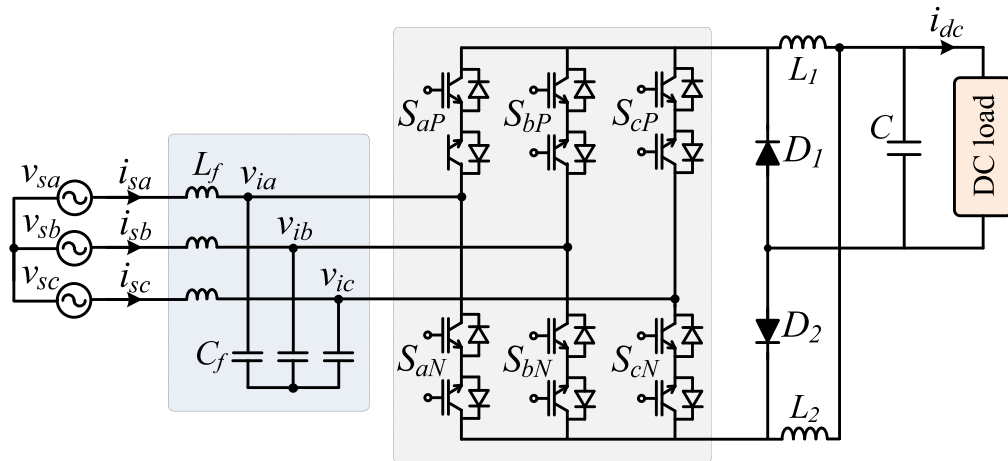
Figure 1.4 The AC-DC MC with Current Doubler Rectifier.
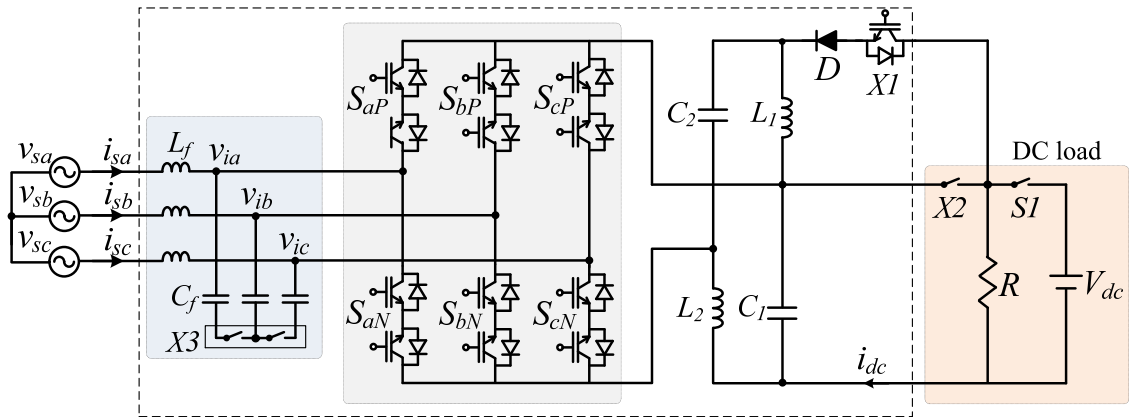
Figure 1.5 The AC-DC Matrix-Z-Source Converter.

conversion efficiency. This topology is of high interest for applications such as telecommunication, power supplies for process technology and More Electric Aircraft (MEA) systems.

In [23] and [24], an AC-DC Matrix-Z-Source Converter (MZC) is presented for the integrated starter/alternator (ISA) system, as shown in Figure 1.5. The MZC inherits both advantages of the AC–DC MC and Z-source inverter. This topology provides capability of wide range variable-voltage–variable-frequency (VVVF) DC–AC inversion and AC–DC rectification without extra close-loop control or large energy-storage devices.

For applications where the isolation is required, the AC-DC MC utilizing high-frequency link transformer (HFT) has the merits of compact size, low weight, low cost, high efficiency, and high power density [25]. The HFT provides isolation, voltage transformation and noise
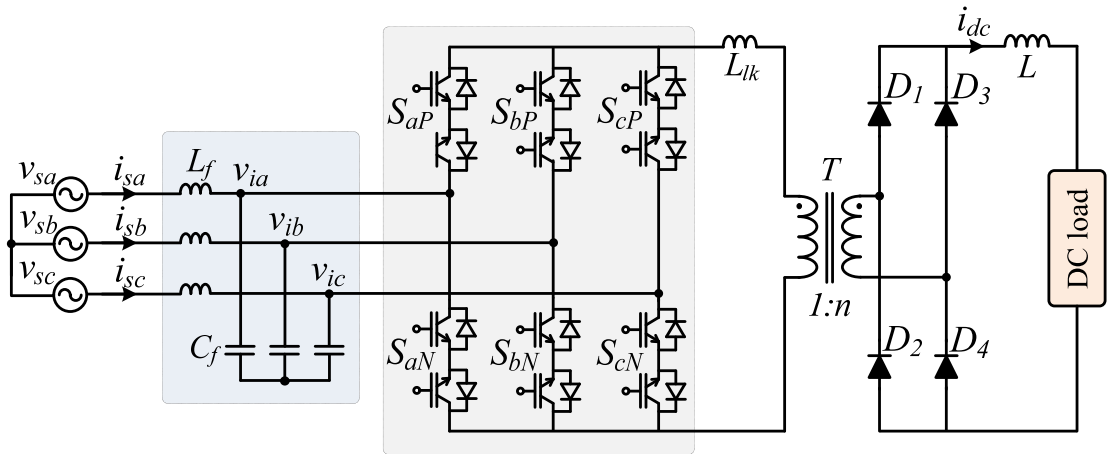
Figure 1.6 The unidirectional isolated AC-DC Matrix Rectifier.
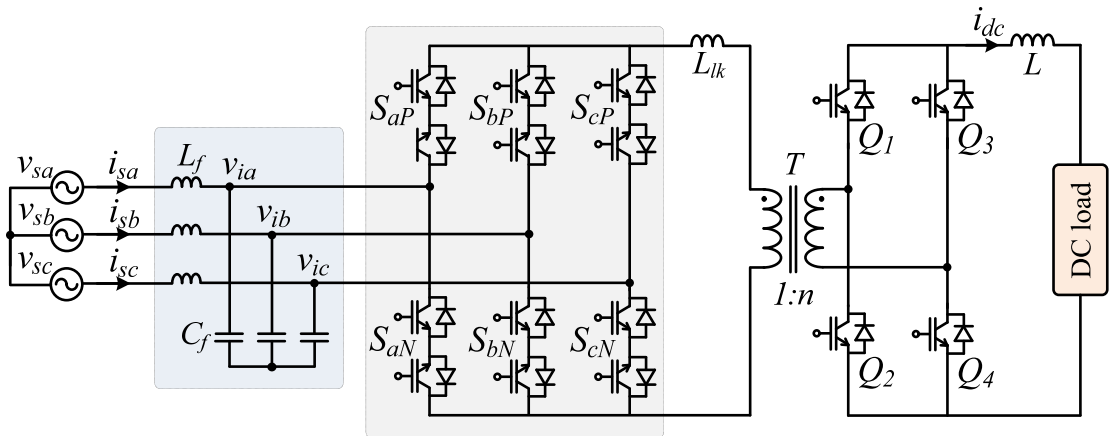
Figure 1.7 The bidirectional isolated AC-DC Matrix Converter.

decoupling. This isolated AC-DC MC type can be classified into two major topologies: unidirectional and bidirectional topologies. Figure 1.6 shows the topology of an unidirectional isolated AC-DC Matrix Rectifier [26]–[31]. It consists of an input LC filter, a three-to-one phase MC, a HFT, a diode bridge rectifier and an output L filter. This topology is considered promising in AC-DC applications such as front-end power converters for typical telecommunication and high voltage direct current (HVDC) [26], [29]. For application where the bidirectional power conversion is required such as on-board EV charger for V2G applications [32]–[35], BESS [25], [36]–[38], hybrid AC-DC microgrids [39], the diode bridge rectifier is replaced with a full-bridge converter using IGBT or MOSFET, as shown in Figure 1.7.

1.2.2 Modulation and Control Methods

A variety of pulse width modulation (PWM) switching techniques has been developed for AC–DC MC. The first modulation is presented based on the Alesina–Venturini (A-V) optimum modulation [10]. This modulation method can provide a tight DC voltage regulation, but the input power factor compensation is not achieved. Up to now, the space vector modulation (SVM) is the most widely used for AC-DC MC due to its easy implementation and additional freedom to optimize the performance and to minimize the switching losses [11]–[13], [19], [20], [40]–[42]. To reduce the output current ripple, the active vectors are properly selected according to the output range [12], [13], and the zero vectors are optimally utilized according to the switching pattern [20], [42]. In [43], the optimal segmental switching pattern is proposed to eliminate narrow pulse, which causes grid current distortion and even switches commutation failure. For other purposes, the SVM has been modified to reduce the common-mode voltage [19], and to minimize switching loss [40], [41].

Many linear control methods have been presented to drive the AC-DC MC based on the SVM. In [13], [44], a dual-loop control scheme with outer DC voltage and inner DC current loops is proposed based on proportional integral (PI) controller. The AC input current is set to be in phase with the grid voltage, while its amplitude is indirectly controlled. To control input power factor (IPF), a PI controller is realized for the input current displacement angle [11]. A control method to fully control of the grid and output side of an AC-DC MC is presented in [20]. The grid side active and reactive power is controlled independently through controlling the grid current in *dq* synchronous frame. And, the output side is utilized to control a battery in three operation modes, namely, constant power charging/discharging mode (CP), constant current charging mode (CC) and constant voltage charging mode (CV).

Aside from linear control methods, modern control methods have recently been presented to control the input and output side of an AC-DC MC. In [45], the DC voltage controller sets the d-axis AC input current reference and then the AC input current is directly controlled using a one-cycle control (OCC) method without a modulator. Various sliding mode control (SMC) strategy are presented to achieve both a tight DC voltage regulation and a power factor control by applying the Reaching Law Sliding Mode Control (RL-SMC)

[46], and a global sliding mode control (GSMC) based on a hyperbolic tangent function [47]. In [48], a fuzzy controller is adopted to improve the dynamic performance of battery charger using an AC-DC Matrix Rectifier. Lately, model predictive control (MPC) is emerging as the most widely used modern method for AC-DC MC to achieve fast dynamic response and simple implementation [21], [49], [50]. Thanks to the discrete nature of the converter, a discrete model is used to select the optimal switching state by minimizing the cost function. Therefore, only one switching state is applied to drive the converter in each sampling period, and no modulation stage is needed.

1.2.3 Operation under Abnormal Conditions

The abnormal grid voltage conditions including unbalance and distortion occur frequently in practical due to various asymmetrical grid faults and nonlinear loads. Any abnormal condition in the grid voltage will give rise to ripple on the DC side and harmonic distortion in the grid current [51]–[53]. The feedforward control is known as the most common and simplest method to compensate the effects of the abnormal grid voltage conditions on the output performance by regulating the instantaneous modulation index [53]. However, this causes severe harmonics in the grid current. The control methods for AC-DC MC under abnormal grid voltage conditions have been less studied. However, some control methods that are used for AC–AC MCs under abnormal conditions can be properly applied to enhance both the output and grid sides performance for AC-DC MCs [54]–[60].

1.3   Frameworks and Objectives of the Thesis

The target of this thesis is to propose advanced control strategies to drive the AC-DC MCs under unbalanced grid voltage conditions. The proposed control strategies are developed based on two widely used techniques: SVM and MPC. The control objectives are provided to achieve constant output voltage and current, sinusoidal grid current, and a near unity grid power factor. Theoretical analysis, simulation, and experiments have been investigated to demonstrate the advanced performances of the proposed control strategies. The main contributions of the thesis are:

- Development of an enhanced control strategy based on an independent control scheme for the active and reactive powers. The input current reference is generated from instantaneous power analysis in a stationary frame, then directly synthesized to obtain sinusoidal grid current and constant DC voltage and current without any input current controller. Furthermore, an average grid reactive power-based PI controller is developed to achieve a near unity grid power factor. The average grid reactive power is obtained through a notch filter without using the grid voltage sequence components, so the proposed control strategy is implemented easily without large storage requirement.

- Development of a simplified MPC (S-MPC) scheme with active damping function. The grid current reference is generated by analyzing the instantaneous power model in a stationary frame without the grid voltage components extraction. The prediction process is simplified by computing only one required input current vector (RICV) instead of nine grid current predictions. Additionally, the active damping function is realized without increasing the computational burden by integrating the damping current into the RICV. Thus, the execution time of the S-MPC is significantly reduced, and the system performance is easily improved by shortening the sampling period.

- Development of a virtual-flux-based MPC (VF-MPC) scheme to remove the grid voltage sensor and enhance the grid current performance. The grid current reference and grid voltage are obtained in terms of the virtual flux (VF) and its 90° lagging signal. Furthermore, the number of current vectors is increased from 9 to 39 vectors by generating 30 virtual current vectors to minimize the grid current tracking error. To reduce the computational burden due to the increased number of current vectors, a preselection method is developed to reduce the number of candidate current vectors from 39 to 8.

- Development of an improved MPC (I-MPC) scheme to simultaneously compensate the power ripple in the input filter and reduce the grid current distortion. The power ripple is obtained based on the grid voltage and its 90° lagging signal, which makes the implementation simple without grid voltage components extraction or digital

filter design. In addition, a closed-loop current controller is developed based on a resonant controller (RC) to reduce the grid current harmonic caused by power ripple under unbalanced grid voltage conditions.

1.4 Outline of the Thesis

Following this introduction, the fundamentals of AC-DC MC are introduced in Chapter 2.

Chapter 3 presents an enhanced control strategy for AC-DC MCs based on an independent control scheme for the active and reactive powers using SVM.

Chapter 4 presents a simplified MPC scheme with active damping function for AC-DC MCs.

Chapter 5 presents a virtual-flux-based MPC scheme for AC-DC MCs to remove the grid voltage sensor and enhance the grid current performance.

Chapter 6 presents an improved MPC scheme for AC-DC MCs to simultaneously compensate the power ripple in the input filter and reduce the grid current distortion.

Chapter 7 concludes the work in this thesis and provides feasible recommendations for future research.

Chapter 2

Fundamentals of AC-DC Matrix Converter

2.1   Basic Operation of AC-DC MC

The basic circuit of an AC-DC MC is shown in Figure 2.1. It consists of a three-phase AC supply, an second-order input LC filter, a power circuit with six bidirectional power switches, an inductor output L filter, and a DC load. The input LC filter is used to eliminate the high-frequency current harmonics, and the output L filter is used to mitigate the output current ripple.
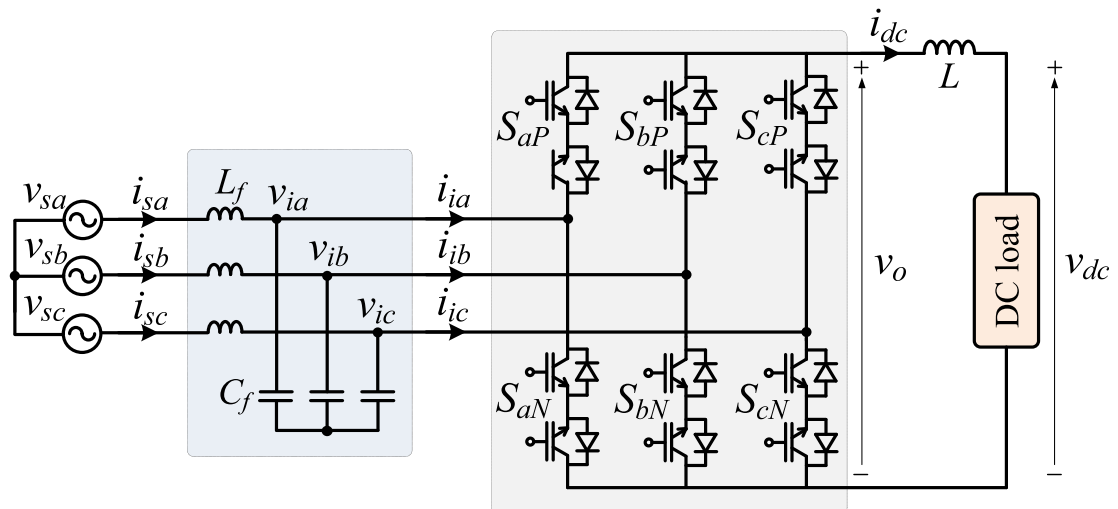
Figure 2.1 Basic circuit of an AC-DC MC.
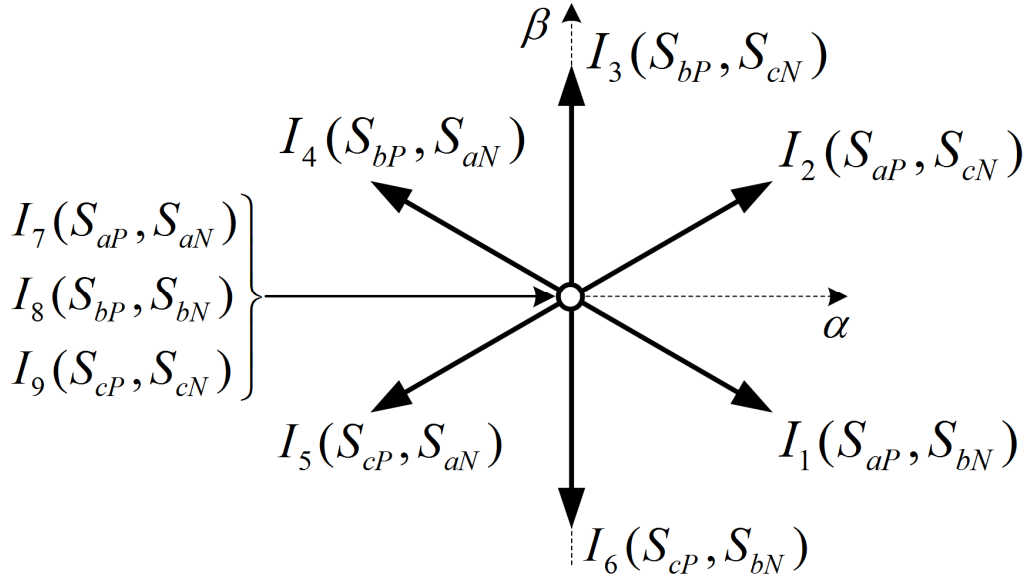
Figure 2.2 Space vector diagram of input current vector for AC-DC MC.

With the relevant symbols shown in Figure 2.1, the input currents i_{ia}, i_{ib}, and i_{ic} and the output current i_{dc} have the following relationship:

$$\begin{bmatrix} i_{ia} \\ i_{ib} \\ i_{ic} \end{bmatrix} = \begin{bmatrix} S_{aP} - S_{aN} \\ S_{bP} - S_{bN} \\ S_{cP} - S_{cN} \end{bmatrix} i_{dc} = \mathbf{S}i_{dc},$$ (2.1)

where $\mathbf{S}$ is the switching state matrix, and S_{xy} is the state of each six bidirectional power switches ($x \in \{a,b,c\}$ and $y \in \{P,N\}$). The state is equal to 1 when S_{xy} is turned on and 0 when S_{xy} is turned off.

Let the space vector $\mathbf{x}$ be defined as follows:

$$\mathbf{x} = x_\alpha + jx_\beta = 2\left(x_a + x_b e^{j2\pi/3} + x_c e^{j4\pi/3}\right)/3$$ (2.2)

where x_α and x_β are the components in the $\alpha\beta$ stationary frame, and x_a, x_b, and x_c are the components in the three-phase *abc* stationary frame.

Considering the prohibitions of the short circuit on the input side and the open circuit on the output side, there are nine possible switching states to control the AC/DC MC. With these states, the input current vector are limited to six active vectors I_1-I_6 and three zero vectors I_7-I_9, as shown in Figure 2.2. The four-quadrant operation of the AC-DC MC is shown in Figure 2.3. Both polarities of voltages and currents may be controlled during the bidirectional operation.
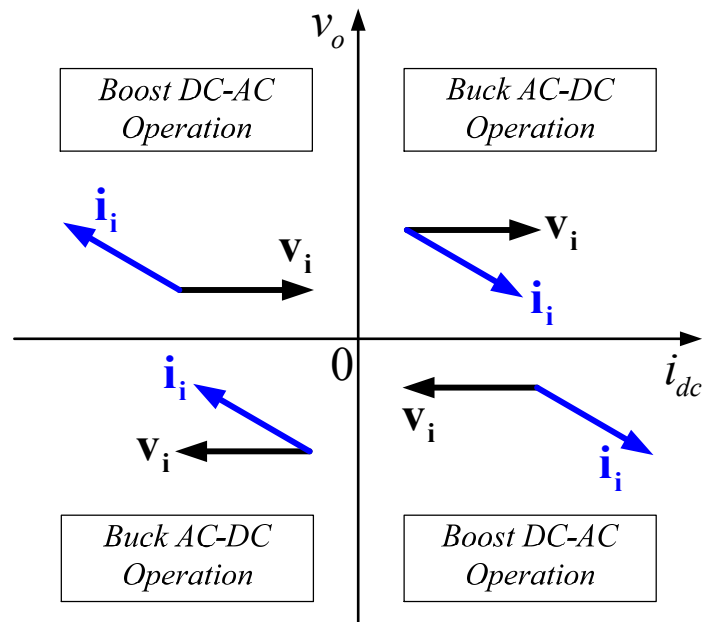
Figure 2.3 Four-quadrant operation of the AC-DC MC.

2.2 Input Filter

The input filter is a critical part to eliminate the high frequency switching ripple in the input current of the AC/DC MC. Several research works have concerned with the problem of the input filter, such as filter topology and filter design [61]–[66]. A properly designed filter must also ensure the following: 1) minimum voltage drop; 2) high-quality voltage at the converter input; 3) high grid power factor, and 4) stability. The input filter design also affects the weight and volume of the overall converter and, hence, the cost of equipment.

From cost and weight considerations, the single-stage LC filter has been found to be the most appropriate topology [65]. The LC filter is usually realized with the damping resistors in parallel or series with the inductors to avoid resonance, as shown in Figure 2.4. This method is easy to implement, but results in excessive power losses. To overcome this drawback, several active damping methods have been realized without affecting the converter efficiency by emulating a virtual resistor in parallel with the filter capacitor [67]–[71].
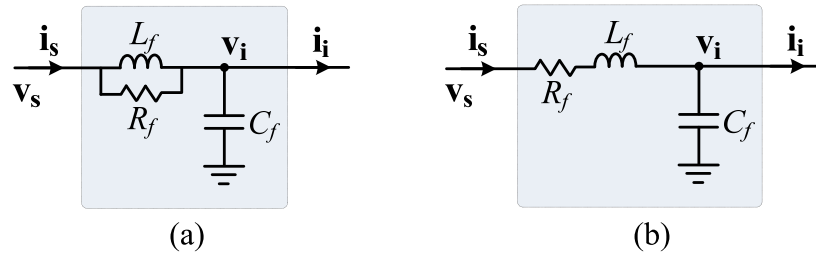
Figure 2.4 LC input filter with damping resistor in (a) parallel, and (b) series with inductor.
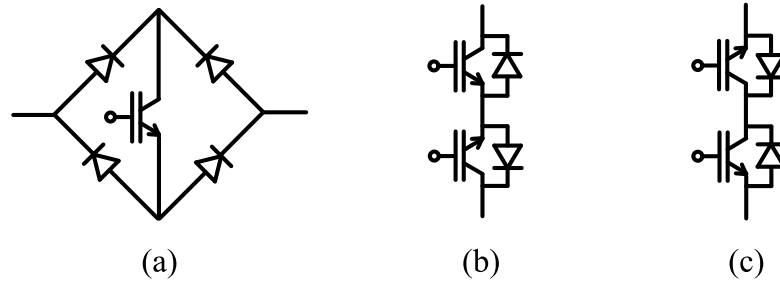
Figure 2.5 Bidirectional switch arrangements: (a) Diode bridge arrangement, (b) common
emitter arrangement, and (c) common collector arrangement.

2.3   Bidirectional Switches

The power circuit of an AC-DC MC is realized by six bidirectional switches. Currently, bidirectional switches must be constructed from available unidirectional devices. Most MC applications use IGBT devices and diodes to create the bidirectional switch [15], [72]. Some typical arrangements are shown in Figure 2.5.

The diode bridge arrangement is the simplest bidirectional switch, which uses only one IGBT as shown in Figure 2.5(a). This arrangement requires only one gate drive per bidirectional switch. However, the conduction losses are higher than other arrangements since the current flows through one IGBT and two diodes.

The common emitter and common collector arrangements are the two most commonly used bidirectional switch. Both these switches are realized from two IGBTs and two diodes as shown in Figure 2.5(b) and (c). They allow the current direction to be controlled, and this allows greater flexibility when performing the commutation of current between input phases.
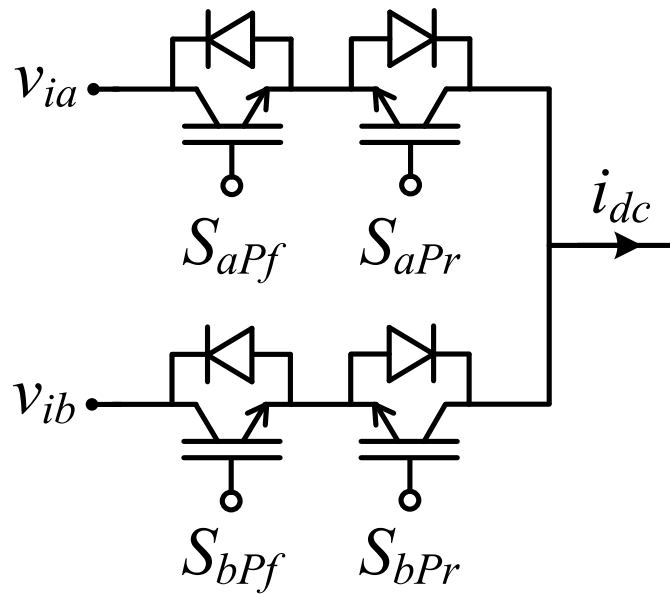
Figure 2.6 A simplified two-phase to single-phase AC-DC MC.

2.4   Bidirectional Switch Commutations

Bidirectional switch commutation is an important issue for the reliable and safe operation of AC-DC MCs. The commutation should be achieved without causing both short circuits on the input side and the open circuits on the output side. Any mistake in commutation may lead to overcurrent and overvoltage that will destroy the converter and the systems. For the two most commonly used bidirectional switch in Figure 2.5(b) and (c), several commutation techniques have been proposed in literature either based on output current or input voltage sign measurement, or both output current and input voltage sign measurements [73]–[77]. Among them, the most common commutation technique which is generally used by researchers is the four-step output-current-based commutation technique [77].

Figure 2.6 shows a simplified two-phase to single-phase AC/DC MC to explain the four-step output-current-based commutation technique. The commutation proceeds from input phase a to input phase b when the output current i_{dc} is positive is shown in Figure 2.7(a). The IGBTs that control the positive output current are forward switches (i.e., S_{aPf}, S_{bPf}), and those for the negative output current are reverse switches (i.e., S_{aPr}, S_{bPr}). Before the
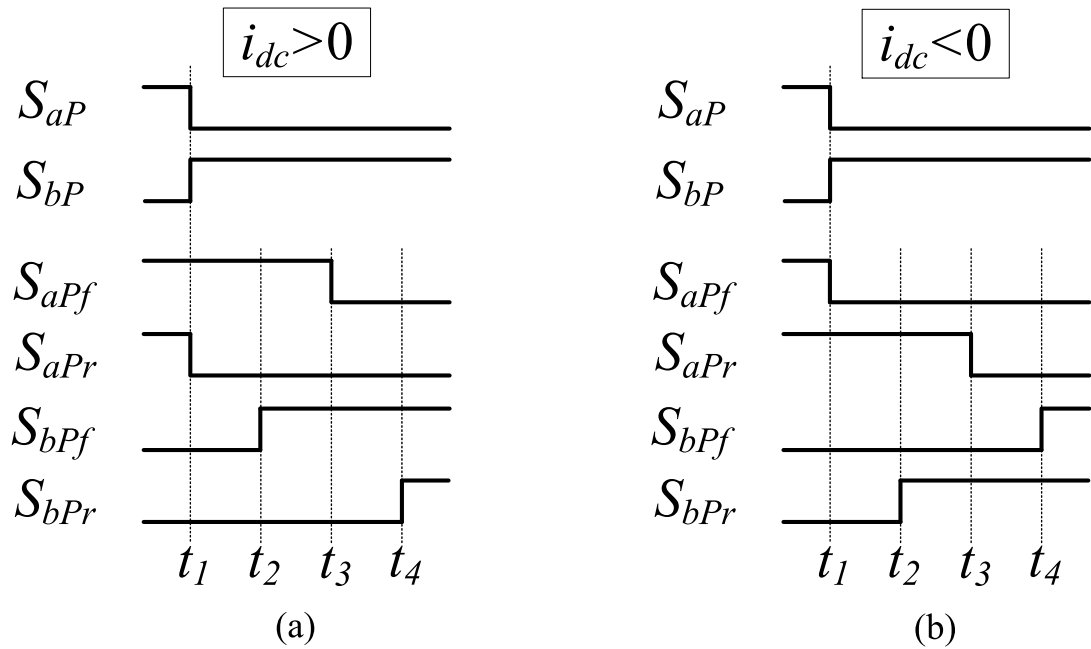
Figure 2.7 Four-step commutation sequence: (a) possitve output current, (b) negative output current.

commutation process, both two switches S_{aPf} and S_{aPr} are turned on. The four-step commutation with the sequence turn-on and turn-off of 4 switches S_{aPf}, S_{aPr}, S_{bPf}, and S_{bPr} is:

- Step 1: At t_1, the switch S_{aPr} that is not conducting the output current is turned off.

- Step 2: At t_2, the switch S_{bPf} that will conduct the output current within the on-coming bidirectional switch is turned on.

- Step 3: At t_3, the switch S_{aPf} that is conducting the output current within the off-going bidirectional switch is turned off.

- Step 4: At t_4, the switch S_{bPr} that will not conduct the output current within the on-coming bidirectional switch is turned on.

After the step 2, the two switches S_{aPf} and S_{bPf} can provide a path for the positive output current. If $v_{ia} < v_{ib}$, the output current is naturally transferred from S_{aP} to S_{bP} at step 2. If $v_{ia} > v_{ib}$, the output current is forcedly transferred from S_{aP} to S_{bP} at step 3. Similarly, the four-step commutation from input phase a to input phase b when the output current i_{dc} is negative is shown in Figure 2.7(b).

2.5   Summary

The fundamentals of AC-DC MC have been presented in this chapter. First, the basic operation of the AC-DC MC has been introduced. The converter is modeled based on the switching matrix. There are nine possible switching states to satisfy the requirement for safe operation. Then, the basic hardware implementation of AC-DC MC such as input filter, bidirectional switch arrangements are presented. Subsequently, the switch commutation techniques for safe operation are also provided in this chapter.

Chapter 3

An Enhanced Control Strategy with Space Vector Modulation

Under unbalanced grid voltage conditions, an AC-DC MC induces ripple on the DC side, as well as severe grid current harmonics. To overcome these problems, an enhanced control strategy for an AC-DC MC is proposed based on an independent control scheme for the active and reactive power. The generated current reference is directly synthesized from instantaneous power analysis in a stationary frame, and a constant DC voltage and current and sinusoidal grid current are obtained. Moreover, the input power factor becomes almost unity due to the reactive power control, in spite of unbalanced grid voltage conditions. There is no need to extract grid voltage components such as the positive and negative sequences, and a controller for the grid current is not required, in contrast to previous methods. Thus, the proposed control method can be implemented easily without a large storage requirement. Simulation and experimental results are presented to verify the effectiveness of the proposed control strategy.

3.1   Introduction

To drive the AC/DC MC effectively, many control methods with balanced grid voltage have been presented [11]–[13], [19]–[21], [41]–[43]. However, unbalanced grid voltage occurs frequently due to various grid faults or disturbances. Unbalanced grid voltage gives rise to ripple on the DC side and low-order harmonics in the grid current, so it should be managed properly. In [53] and [78], the DC voltage feedback control and the feedforward methods are presented to compensate the effects of the unbalanced grid voltage on the output performance by regulating instantaneous modulation index. However, they cause severe harmonics in the grid current. To enhance both the DC-side and AC-side performance under unbalanced grid voltage, some AC/DC MCs use control methods that are used for AC/AC MCs [54]–[58]. In [54], the angle of the modulated input current vector was dynamically calculated as a function of the positive and negative sequence components of the grid voltage to suppress the undesirable harmonics in the grid currents. This has been widely adopted in many studies to obtain a sinusoidal grid current with the SVM [55], [56], double-line voltage synthesis algorithm [57], and online optimization of duty cycles [58]. However, all these methods need to extract the positive and negative sequence components of the grid voltage, which is usually complicated and requires a large amount of storage.

Some advanced control methods have been presented to avoid the difficulty of extracting the grid voltage components [52], [59], [60]. In [59], the expected input power factor angle is simply constructed with a notch filter. Even though a sinusoidal grid current is achieved, it is hard for this method to control the input reactive power. In another study [60], a resonant controller (RC) was used for the input current and active power controllers to suppress the grid current harmonics and ensure constant grid active power. However, because of the instantaneous active power in the input filter, the grid active power is not completely transferred to the load under unbalanced grid voltages. Consequently, the output voltage and output power still contain some ripple, although the grid active power is constant. To solve this problem, a proportional integral (PI) controller was introduced to ensure constant output power along with the RC to control the input current [52]. However, the current references

are highly distorted under unbalanced grid-voltage conditions because the input active and reactive power flow were not quantitative analyzed. Therefore, the grid current performance significantly depends on the gains of the RC [52], [60].

To overcome the problems mentioned, the input current reference is directly synthesized by means of an independent control scheme for active and reactive power to achieve three main goals: 1) constant DC voltage and current, 2) sinusoidal grid current, and 3) near unity input power factor. The input current reference is generated by analyzing the instantaneous power model of the AC/DC MC based on the voltage and current in a stationary frame and their 90° lagging signals without extracting the grid voltage sequence components. Thanks to the inherent capability of direct input current synthesis, the sinusoidal grid current is obtained without any input current controller. Additionally, a near unity power factor is simply achieved by using an average grid reactive power-based PI controller. The average grid reactive power is obtained through a notch filter without using the grid voltage sequence components, so the input power factor is controlled easily without large storage requirements compared to a previous method [79]. The proposed control strategy was verified by simulation and experimental results.

3.2　Modulation and Control of AC-DC MC

3.2.1　Feedforward Compensation Method Using SVM

Figure 3.1 shows the AC-DC MC configuration. The conventional SVM algorithm is used to control the AC-DC MC. The modulation index m_i and the input current vector angle φ_v are used to implement the SVM [52]. The modulation index m_i is defined as the ratio of the input current reference amplitude I_{im} and output current i_{dc}; i.e., $m_i = I_{im} / i_{dc} \ (0 \le m_i \le 1)$.

Ignoring the power losses of the switching matrix, the instantaneous input active power to the converter is equal to the output power to the load since there is no energy storage element in the AC-DC MC:

$$p_i = p_{out} = \frac{3}{2} V_{im} I_{im} \cos \varphi_{vi} = i_{dc} v_{dc}, \tag{3.1}$$
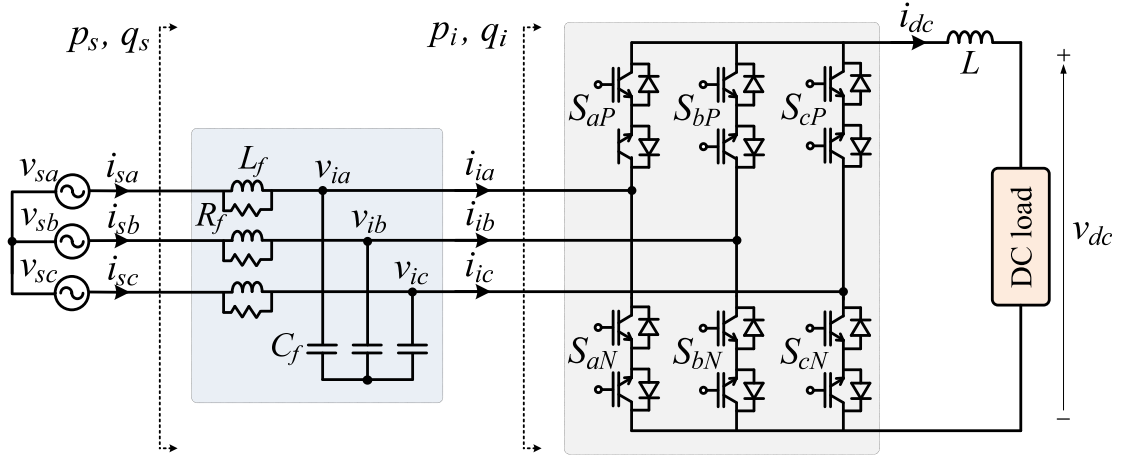
Figure 3.1 AC-DC MC configuration.

where V_{im} is the amplitude of the input voltage vector, v_{dc} is the output voltage, and φ_{vi} is the input power factor angle. From (3.1), the output voltage is expressed as follows:

$$v_{dc} = \frac{3}{2} V_{im} m_i \cos \varphi_{vi}. \tag{3.2}$$

Under unbalanced input voltage, the amplitude of the input voltage V_{im} includes double grid-frequency ripple [56]. Therefore, the conventional SVM with a fixed value of m_i and φ_{vi} results in double grid-frequency ripple in the output voltage, which makes the grid current distorted. The feedforward method has been commonly used to overcome the degradation in output performance due to the unbalanced input voltage [53].

Figure 3.2 shows the feedforward compensation method for an AC-DC MC. The instantaneous grid voltage is sampled to calculate the voltage vector amplitude V_{sm} and phase angle φ_v. The modulation index m_i is adjusted according to the instantaneous voltage vector amplitude V_{sm} to provide constant output voltage. Assuming that the input voltage is same as the grid voltage since the voltage drop across the filter inductor is negligible. From (3.2), the modulation index is calculated as follows:

$$m_i = \frac{2V_{dc}^{ref}}{3V_{sm} \cos \varphi_{vi}}, \tag{3.3}$$

where V_{dc}^{ref} is the output voltage reference.

The input current vector phase angle φ_i is calculated as follows:

$$\varphi_i = \varphi_v - \varphi_{vi}. \tag{3.4}$$
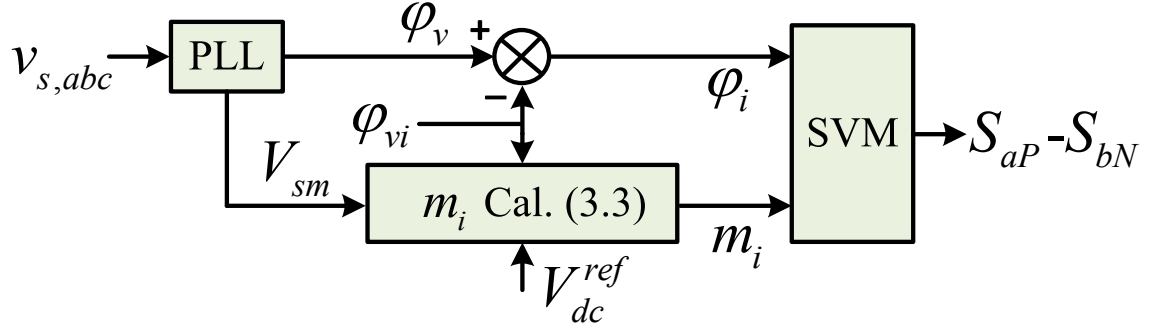
Figure 3.2 Feedforward compensation for AC-DC MC using SVM.

Since the input current is directly synthesized by the output current, the active power is controlled by regulating the modulation index m_i. And, the reactive power is controlled by the input power factor angle φ_{vi}.

3.2.2 Independent Control Scheme for Active and Reactive Powers

As shown in Figure 3.2, φ_{vi} depends on both the active power and the reactive power, so the active and reactive powers cannot be independently controlled to obtain the desired input power factor. Figure 3.3 shows the modified control scheme to control the active and reactive power of the AC-DC MC independently. The expected output current i_{dc}^{ref} is generated by the PI controller to control the output voltage. Then, the output power reference is obtained as follows:

$$P_{dc}^{ref} = i_{dc}^{ref} v_{dc}. \tag{3.5}$$

Based on instantaneous power theory, the input current reference is calculated as [52]:

$$\begin{bmatrix} i_{i\alpha}^{ref} \\ i_{i\beta}^{ref} \end{bmatrix} = \frac{2}{3} \frac{P_{dc}^{ref}}{V_{sm}^2} \begin{bmatrix} v_{s\alpha} \\ v_{s\beta} \end{bmatrix} + \frac{2}{3} \frac{Q^{ref}}{V_{sm}^2} \begin{bmatrix} v_{s\beta} \\ -v_{s\alpha} \end{bmatrix}, \tag{3.6}$$

where $v_{s\alpha}$ and $v_{s\beta}$ are the α and β components of the grid voltage in the stationary frame, and Q^{ref} is the input reactive power reference. By synthesizing the input current reference (3.6), the active and reactive power of the AC-DC MC can be controlled independently.

By using $i_{i\alpha}^{ref}$ and $i_{i\beta}^{ref}$, the modulation index m_i in (3.3) and the input current vector angle φ_i in (3.4) become:
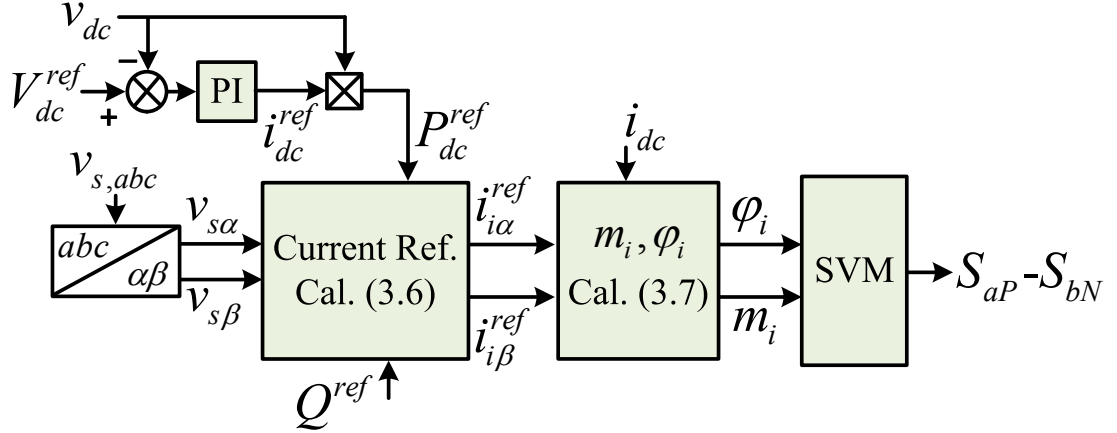
Figure 3.3 Independent control scheme for active and reactive powers.

$$\begin{cases} m_i = \sqrt{\left(\dfrac{i_{i\alpha}^{ref}}{i_{dc}}\right)^2 + \left(\dfrac{i_{i\beta}^{ref}}{i_{dc}}\right)^2} \\ \varphi_i = \arctan\left(i_{i\beta}^{ref} / i_{i\alpha}^{ref}\right) \end{cases} \tag{3.7}$$

The modified control scheme has the same input-output transfer function as the feedforward compensation method. Although constant output voltage is obtained, the input current reference with a fixed value of Q^{ref} leads to severe low-order harmonics in the grid current when the grid voltage is unbalanced, particularly third- and fifth-order harmonics [52]. To overcome this problem, this chapter develops a new method to calculate the input current reference based on a quantitative analysis of the active and reactive power flow.

3.3   Proposed Control Strategy with SVM

3.3.1 Instantaneous Power Analysis in the Stationary Frame

In unbalanced grid voltage operation, the input voltage and current vectors of the AC/DC MC can be expressed as:

$$\mathbf{v_i} = \mathbf{V_p}\, e^{j\omega t} + \mathbf{V_n}\, e^{-j\omega t}, \tag{3.8}$$

$$\mathbf{i_i} = \mathbf{I_p}\, e^{j\omega t} + \mathbf{I_n}\, e^{-j\omega t}, \tag{3.9}$$

where $\mathbf{V_p}$, $\mathbf{V_n}$, $\mathbf{I_p}$, and $\mathbf{I_n}$ are the time phasors of the positive and negative sequence components of the input voltage and current, and ω is the input angular frequency.

The instantaneous active and reactive powers at the input side of converter are expressed as:

$$p_i = \frac{3}{2}\text{Re}(\mathbf{v_i}\mathbf{i_i^*}) = \frac{3}{2}\text{Re}\left((\mathbf{V_p}\,e^{j\omega t} + \mathbf{V_n}\,e^{-j\omega t})(\mathbf{I_p}\,e^{j\omega t} + \mathbf{I_n}\,e^{-j\omega t})^*\right)$$
$$= P_0 + P_{c2}\cos(2\omega t) + P_{s2}\sin(2\omega t), \tag{3.10}$$

$$q_i = \frac{3}{2}\text{Im}(\mathbf{v_i}\mathbf{i_i^*}) = \frac{3}{2}\text{Im}\left((\mathbf{V_p}\,e^{j\omega t} + \mathbf{V_n}\,e^{-j\omega t})(\mathbf{I_p}\,e^{j\omega t} + \mathbf{I_n}\,e^{-j\omega t})^*\right)$$
$$= Q_0 + Q_{c2}\cos(2\omega t) + Q_{s2}\sin(2\omega t), \tag{3.11}$$

where

$$\begin{cases} P_0 = \frac{3}{2}\text{Re}(\mathbf{V_p}\mathbf{I_p^*} + \mathbf{V_n}\mathbf{I_n^*}) \\ P_{c2} = \frac{3}{2}\text{Re}(\mathbf{V_p}\mathbf{I_n^*} + \mathbf{V_n}\mathbf{I_p^*}) \\ P_{s2} = \frac{3}{2}\text{Re}(j\mathbf{V_p}\mathbf{I_n^*} - j\mathbf{V_n}\mathbf{I_p^*}) \\ Q_0 = \frac{3}{2}\text{Im}(\mathbf{V_p}\mathbf{I_p^*} + \mathbf{V_n}\mathbf{I_n^*}) \\ Q_{c2} = \frac{3}{2}\text{Im}(\mathbf{V_p}\mathbf{I_n^*} + \mathbf{V_n}\mathbf{I_p^*}) \\ Q_{s2} = \frac{3}{2}\text{Im}(j\mathbf{V_p}\mathbf{I_n^*} - j\mathbf{V_n}\mathbf{I_p^*}). \end{cases} \tag{3.12}$$

P_0 and Q_0 are the average values of the active and reactive power, and P_{c2}, P_{s2}, Q_{c2} and Q_{s2} are the ripples of the active and reactive power.

To eliminate the positive and negative sequence components of the input voltage and current in (3.12), the instantaneous power of an AC-DC MC is analyzed in the stationary frame (αβ frame) using the input voltage and current and their 90° lagging signals [80], [81]. In this chapter, *x'* denotes the signal that lags behind *x* by 90°. The lagging signals of the input voltage and current vectors are expressed as follows:

$$\mathbf{v_i'} = \mathbf{V_p}\,e^{j(\omega t - \frac{\pi}{2})} + \mathbf{V_n}\,e^{-j(\omega t - \frac{\pi}{2})} = -j\mathbf{V_p}\,e^{j\omega t} + j\mathbf{V_n}\,e^{-j\omega t}, \tag{3.13}$$

$$\mathbf{i_i'} = \mathbf{I_p}\,e^{j(\omega t - \frac{\pi}{2})} + \mathbf{I_n}\,e^{-j(\omega t - \frac{\pi}{2})} = -j\mathbf{I_p}\,e^{j\omega t} + j\mathbf{I_n}\,e^{-j\omega t}. \tag{3.14}$$

From (3.8), (3.9), (3.13), and (3.14), the relationships between time phasors of the positive and negative sequence components and the signals in αβ frame are:

$$\begin{bmatrix} \mathbf{V_p} \\ \mathbf{V_n} \end{bmatrix} = \frac{1}{2}\begin{bmatrix} e^{-j\omega t} & je^{-j\omega t} \\ e^{j\omega t} & -je^{j\omega t} \end{bmatrix}\begin{bmatrix} \mathbf{v_i} \\ \mathbf{v_i'} \end{bmatrix}, \tag{3.15}$$

$$\begin{bmatrix} \mathbf{I_p} \\ \mathbf{I_n} \end{bmatrix} = \frac{1}{2} \begin{bmatrix} e^{-j\omega t} & je^{-j\omega t} \\ e^{j\omega t} & -je^{j\omega t} \end{bmatrix} \begin{bmatrix} \mathbf{i_i} \\ \mathbf{i_i'} \end{bmatrix}. \tag{3.16}$$

Noting that $\mathbf{v_i} \approx \mathbf{v_s} = v_{s\alpha} + jv_{s\beta}$, $\mathbf{v_i'} \approx \mathbf{v_s'} = v_{s\alpha}' + jv_{s\beta}'$, $\mathbf{i_i} = i_{i\alpha} + ji_{i\beta}$, and $\mathbf{i_i'} = i_{i\alpha}' + ji_{i\beta}'$, the active and reactive powers are obtained by substituting (3.15) and (3.16) into (3.12):

$$\begin{cases} P_0 = \dfrac{3}{4}(v_{s\alpha}i_{i\alpha} + v_{s\beta}i_{i\beta} + v_{s\alpha}'i_{i\alpha}' + v_{s\beta}'i_{i\beta}') \\ P_{c2} = \dfrac{3}{4}(k_1 \cos(2\omega t) + k_2 \sin(2\omega t)) \\ P_{s2} = \dfrac{3}{4}(-k_2 \cos(2\omega t) + k_1 \sin(2\omega t)) \\ Q_0 = \dfrac{3}{4}(v_{s\beta}i_{i\alpha} - v_{s\alpha}i_{i\beta} + v_{s\beta}'i_{i\alpha}' - v_{s\alpha}'i_{i\beta}') \\ Q_{c2} = \dfrac{3}{4}(k_3 \cos(2\omega t) + k_4 \sin(2\omega t)) \\ Q_{s2} = \dfrac{3}{4}(-k_4 \cos(2\omega t) + k_3 \sin(2\omega t)) \end{cases} , \tag{3.17}$$

where

$$\begin{cases} k_1 = (v_{s\alpha}i_{i\alpha} + v_{s\beta}i_{i\beta} - v_{s\alpha}'i_{i\alpha}' - v_{s\beta}'i_{i\beta}') \\ k_2 = (v_{s\alpha}'i_{i\alpha} + v_{s\beta}'i_{i\beta} + v_{s\alpha}i_{i\alpha}' + v_{s\beta}i_{i\beta}') \\ k_3 = (v_{s\beta}i_{i\alpha} - v_{s\alpha}i_{i\beta} - v_{s\beta}'i_{i\alpha}' + v_{s\alpha}'i_{i\beta}') \\ k_4 = (v_{s\beta}'i_{i\alpha} - v_{s\alpha}'i_{i\beta} + v_{s\beta}i_{i\alpha}' - v_{s\alpha}i_{i\beta}'), \end{cases} , \tag{3.18}$$

$v_{s\alpha}$, $v_{s\beta}$, $i_{s\alpha}$, $i_{s\beta}$, $v_{s\alpha}'$, $v_{s\beta}'$, $i_{i\alpha}'$, and $i_{i\beta}'$ are the $\alpha\beta$ components of the grid voltage, input current, and their 90° lagging signals, respectively.

3.3.2 Proposed Input Current Reference

The input current reference used to control the active and reactive power flows is determined by solving the set of power equations in (3.17). Since there are four controllable degrees of freedom ($i_{i\alpha}$, $i_{i\beta}$, $i_{i\alpha}'$, and $i_{i\beta}'$) for the current reference, four of the six power components in (3.17) can be controlled. The control objectives are to provide constant active power in the load and to obtain sinusoidal grid current under unbalanced grid voltage conditions. To achieve this goal, the average active power P_0 should be equal to the output power reference P_{dc}^{ref}, while the ripples of the active power P_{c2} and P_{s2} should be zero. The reactive power reference Q^{ref} is set to be the average reactive power Q_0 to flexibly regulate the average input power factor. The remaining ripples of the reactive power Q_{c2} and Q_{s2} are

left to be uncontrolled, so reactive power ripples appear under unbalanced grid voltage operations. Finally, the following relationships are applied to satisfy the desired control objectives:

$$\begin{cases} P_0 = P_{dc}^{ref} \\ Q_0 = Q^{ref} \\ P_{c2} = 0 \\ P_{s2} = 0 \end{cases}. \tag{3.19}$$

Equation (3.19) is equivalently solved using (3.20) to find the four controllable variables ($i_{i\alpha}$, $i_{i\beta}$, $i'_{i\alpha}$, and $i'_{i\beta}$).

$$\begin{bmatrix} v_{s\alpha} & v_{s\beta} & v'_{s\alpha} & v'_{s\beta} \\ v_{s\beta} & -v_{s\alpha} & v'_{s\beta} & -v'_{s\alpha} \\ v_{s\alpha} & v_{s\beta} & -v'_{s\alpha} & -v'_{s\beta} \\ v'_{s\alpha} & v'_{s\beta} & v_{s\alpha} & v_{s\beta} \end{bmatrix} \begin{bmatrix} i_{i\alpha} \\ i_{i\beta} \\ i'_{i\alpha} \\ i'_{i\beta} \end{bmatrix} = \begin{bmatrix} \frac{4}{3} P_{dc}^{ref} \\ \frac{4}{3} Q^{ref} \\ 0 \\ 0 \end{bmatrix} \tag{3.20}$$

From (3.20), the input current reference in the αβ frame is obtained as follows:

$$\begin{cases} i_{i\alpha}^{ref} = \frac{2P_{dc}^{ref}}{3} \frac{v'_{s\beta}}{(v'_{s\beta}v_{s\alpha} - v_{s\beta}v'_{s\alpha})} + \frac{4Q^{ref}}{3} \frac{v_{s\beta}}{(v_{s\alpha}^2 + v_{s\beta}^2 + v_{s\alpha}'^2 + v_{s\beta}'^2)} \\ i_{i\beta}^{ref} = -\frac{2P_{dc}^{ref}}{3} \frac{v'_{s\alpha}}{(v'_{s\beta}v_{s\alpha} - v_{s\beta}v'_{s\alpha})} - \frac{4Q^{ref}}{3} \frac{v_{s\alpha}}{(v_{s\alpha}^2 + v_{s\beta}^2 + v_{s\alpha}'^2 + v_{s\beta}'^2)} \end{cases}. \tag{3.21}$$

In (3.21), the denominators become constant from (3.22), and the numerators ($v_{s\alpha}$, $v_{s\beta}$, $v'_{s\alpha}$, and $v'_{s\beta}$) are sinusoidal:

$$\begin{cases} (v'_{s\beta}v_{s\alpha} - v_{s\beta}v'_{s\alpha}) = |\mathbf{V_n}|^2 - |\mathbf{V_p}|^2 \\ (v_{s\alpha}^2 + v_{s\beta}^2 + v_{s\alpha}'^2 + v_{s\beta}'^2) = 2(|\mathbf{V_n}|^2 + |\mathbf{V_p}|^2) \end{cases} \tag{3.22}$$

Therefore, sinusoidal grid current is obtained with the given constant values P_{dc}^{ref} and Q^{ref}. However, it is unbalanced because the grid voltage is unbalanced.

Figure 3.4 shows the control block diagram of the proposed control strategy for the AC-DC MC to achieve a ripple-free DC voltage and current and sinusoidal grid current. The rectifier and inverter modes of the AC-DC MC are selected by the output power reference obtained from output controller in Figure 3.4(a). DC output side utilizes the constant voltage or current consuming mode and the constant current generating mode to absorb or supply active power, respectively, with the output controllers in Figure 3.4(b). A second-order
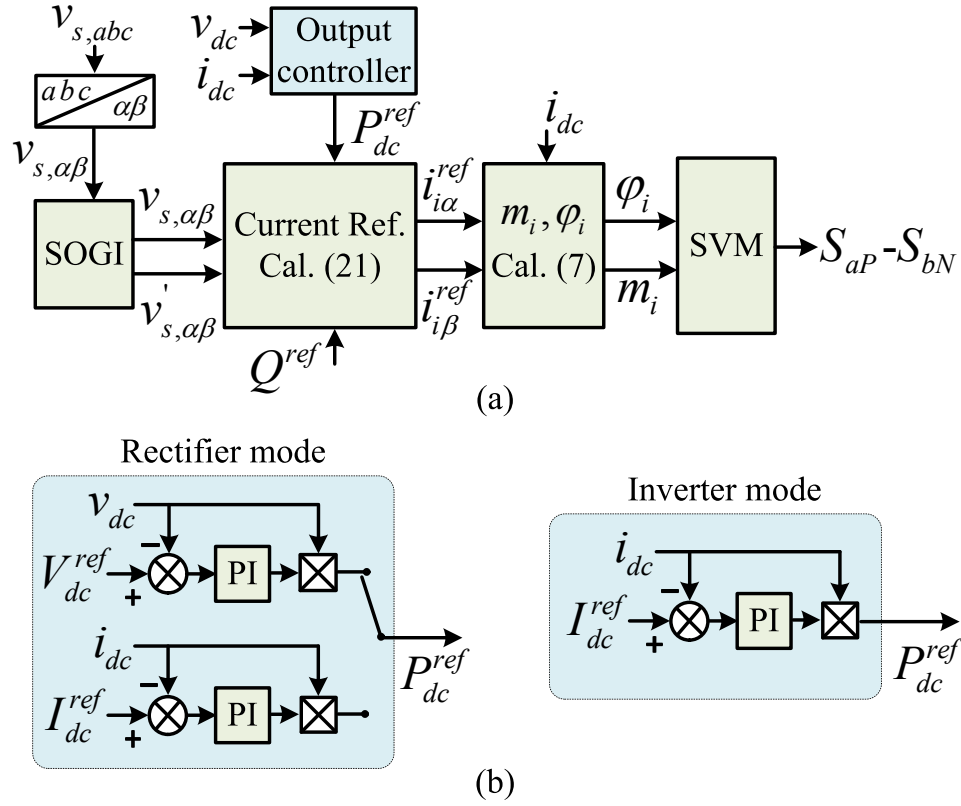
Figure 3.4 Enhanced control strategy for AC-DC MC: (a) Overall control block diagram, (b) Output-side controller for rectifier mode and inverter mode.

generalized integrator (SOGI) is adopted to obtain the lagging signal of the grid voltage because it can track the fundamental component of the grid voltage with zero error, even if the grid voltage is disturbed [82]. The modulation index m_i and the input current vector angle φ_i are obtained from the input current reference in (3.21) by using (3.7)

3.3.3 Maximum Controllable Output Voltage

Under the unbalanced grid voltage conditions, the input voltage vector $\mathbf{v_i}$ in (3.8) is rotating in an elliptical trajectory. Therefore, the amplitude V_{im} is time varying, and its minimum and maximum values become:

$$V_{im}^{\min} = \left|\mathbf{V_p}\right| - \left|\mathbf{V_n}\right|, \tag{3.23}$$

$$V_{im}^{\max} = \left|\mathbf{V_p}\right| + \left|\mathbf{V_n}\right|. \tag{3.24}$$

Substituting (3.23) into (3.2) and noting that the maximum modulation index $m_i^{\max} = 1$,

the maximum controllable output voltage is obtained as follows:

$$V_{dc}^{max} = \frac{3}{2}|\mathbf{V_p}|(1-\mu)\cos\varphi_{vi}, \tag{3.25}$$

where $\mu = |\mathbf{V_n}|/|\mathbf{V_p}|$ is the unbalanced degree.

3.3.4 Comparison with Conventional Methods to Achieve Sinusoidal Grid Currents

There are two typical approaches to obtain sinusoidal grid current under unbalanced grid voltage conditions. One is based on the modulated input current vector direction by using positive and negative sequence components of the grid voltage [54]–[59], and the other is based on a closed-loop controller to regulate the input current without using grid voltage components [52], [60]. To obtain sinusoidal grid current when the expected average input reactive power is zero, previous studies [54]–[59] assigned the direction of the input current vector to that of a modulation vector **D**, which is defined as:

$$\mathbf{D} = \mathbf{V_p}\,e^{j\omega t} - \mathbf{V_n}\,e^{-j\omega t}. \tag{3.26}$$

$j\mathbf{v}'_\mathbf{i}$ is used to find **D**, and (3.27) is obtained from (3.13):

$$j\mathbf{v}'_\mathbf{i} = j(-j\mathbf{V_p}\,e^{j\omega t} + j\mathbf{V_n}\,e^{-j\omega t}) = \mathbf{V_p}\,e^{j\omega t} - \mathbf{V_n}\,e^{-j\omega t}. \tag{3.27}$$

From (3.26) and (3.27), the modulation vector **D** is directly detected from grid voltage components $v'_{s\alpha}$, and $v'_{s\beta}$:

$$\mathbf{D} = j\mathbf{v}'_\mathbf{i} = j(v'_{s\alpha} + jv'_{s\beta}) = -v'_{s\beta} + jv'_{s\alpha}. \tag{3.28}$$

Then, the input current vector angle φ_i is obtained from (3.28):

$$\varphi_i = \arctan\left(-v'_{s\alpha}/v'_{s\beta}\right). \tag{3.29}$$

The input current vector with the phase angle in (3.29) is sinusoidal under the condition of zero average input reactive power on the AC side of the converter.

However, as shown in (3.21), the proposed control strategy provides sinusoidal grid current regardless of the average input reactive power. Furthermore, the input current vector angle in (3.7) becomes the same angle in (3.29) by substituting $Q^{ref} = 0$ into (3.21):

$$\varphi_i = \arctan\left(i_{i\beta}^{ref}/i_{i\alpha}^{ref}\right) = \arctan\left(-v'_{s\alpha}/v'_{s\beta}\right). \tag{3.30}$$
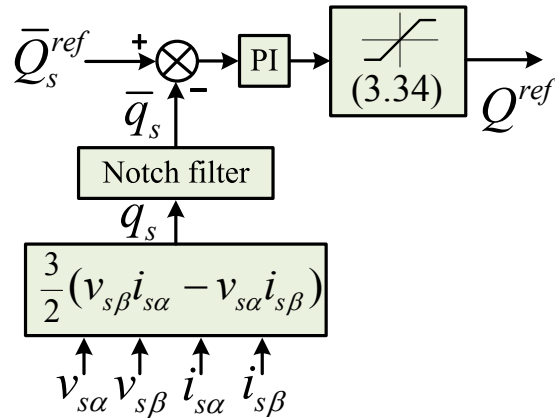
Figure 3.5 Input power factor control for AC-DC MC.

Therefore, the proposed control strategy is much more flexible to obtain sinusoidal grid current because the conventional methods [54]–[59] are limited to zero average input reactive power.

Regarding to the previous methods used in [52] and [60], the input current was regulated by using a closed-loop controller. Therefore, the converter performance significantly depends on controller parameters. Furthermore, the current control loop suffers from problems with system stability. However, the proposed control strategy uses an open-loop method without any controller and is simpler than the previous methods in [52] and [60].

3.4   Reactive Power To Control Input Power Factor

An LC input filter is required to eliminate the high-order harmonics in the input current of the AC-DC MC. However, the input filter usually results in a leading power factor on the grid side, especially in light load conditions. As shown in section 3.3.2, the proposed control strategy can flexibly control the input power factor by regulating the input reactive power reference in (3.21). Figure 3.5 shows the principle of the proposed input power factor control method. The average grid reactive power is regulated to control the input power factor through a PI controller. The output of the PI controller is used to calculate the input current reference in (3.21). Because the grid reactive power includes double grid-frequency

Table 3.1 Simulation and Experimental Parameters

Parameter	Value
Power supply	$\mathbf{V_p} = 70\text{V}\angle 0^0$, $f_i = 60$ Hz
Input filter	$L_f = 1.5$ mH, $C_f = 20~\mu\text{F}$, $R_d = 27~\Omega$
Output	$L = 10$ mH, $R = 10~\Omega$, $V_{dc} = 50$ V
Switching frequency	$f_s = 10$ kHz

oscillations, a notch filter is used to obtain the average value of the grid reactive power. The transfer function of the notch filter is:

$$F(s) = \frac{s^2 + \omega_n^2}{s^2 + 2\xi\omega_n s + \omega_n^2}, \tag{3.31}$$

where ω_n is set to twice the grid frequency, and ξ is set to 0.707 to obtain a good dynamic response and good filter performance.

To achieve an average input power factor of unity, the average grid reactive power reference $\overline{Q}_s^{ref}$ is set to zero. However, the controllable input reactive power is restricted according to the required output power P_{out}^{ref}:

$$\left| q_i^{max} \right| = P_{dc}^{ref} \left| (\tan\varphi_{vi})^{max} \right| = P_{dc}^{ref} \sqrt{\frac{1}{\left(\cos^2\varphi_{vi}\right)^{min}} - 1}. \tag{3.32}$$

The minimum input power factor becomes (3.33) by substituting (3.24) into (3.3):

$$(\cos\varphi_{vi})^{min} = \frac{2V_{dc}^{ref}}{3V_{im}^{max} m_i^{max}} = \frac{2V_{dc}^{ref}}{3\left(\left|\mathbf{V_p}\right| + \left|\mathbf{V_n}\right|\right)}. \tag{3.33}$$

By substituting (3.33) into (3.32), the maximum reactive power becomes:

$$\left| q_i^{max} \right| = P_{dc}^{ref} \sqrt{\frac{9\left|\mathbf{V_p}\right|^2 (1+\mu)^2}{4(V_{dc}^{ref})^2} - 1}. \tag{3.34}$$

3.5   Simulation Results
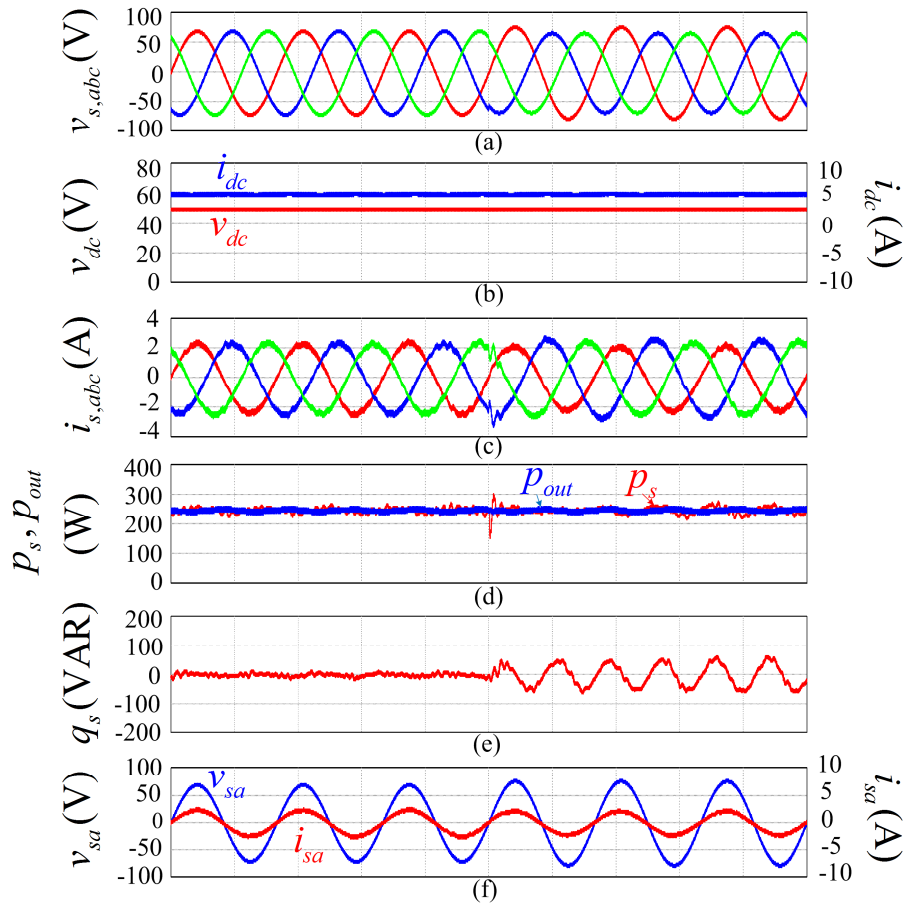
Figure 3.6 Performances of proposed ECS-PFC for rectifier mode of the AC-DC MC (time: 10 ms/div): (a) Grid voltages, (b) output voltage and output current, (c) grid currents, (d) grid and output active powers, (e) grid reactive power, and (f) grid phase-*a* current and voltage.

Simulation was carried out to verify the effectiveness of the proposed control strategy using PSIM software. A degree of unbalance of 10% was performed by injecting a negative and positive sequence voltage, V_p = 70V $\angle$ 0° and V_n = 7V $\angle$ 0°, respectively. When the gird voltage is balanced, V_n is zero. To provide regenerative inverter operation along with power consuming rectifier operation, battery is used as an active load with voltage rating V_{dc} = 50 V. The constant current rectifier/inverter modes are utilized to control the battery. The other parameters are listed in Table 3.1.

Figures 3.6 and 3.7 show the performance of the enhanced control strategy with input power factor control (ECS-PFC) for rectifier mode and inverter mode, respectively, when the balanced grid voltage becomes unbalanced at t = 0.05 s. In the rectifier mode, three-phase grid voltage is shown in Figure 3.6(a) when the output current reference is set at 5 A.
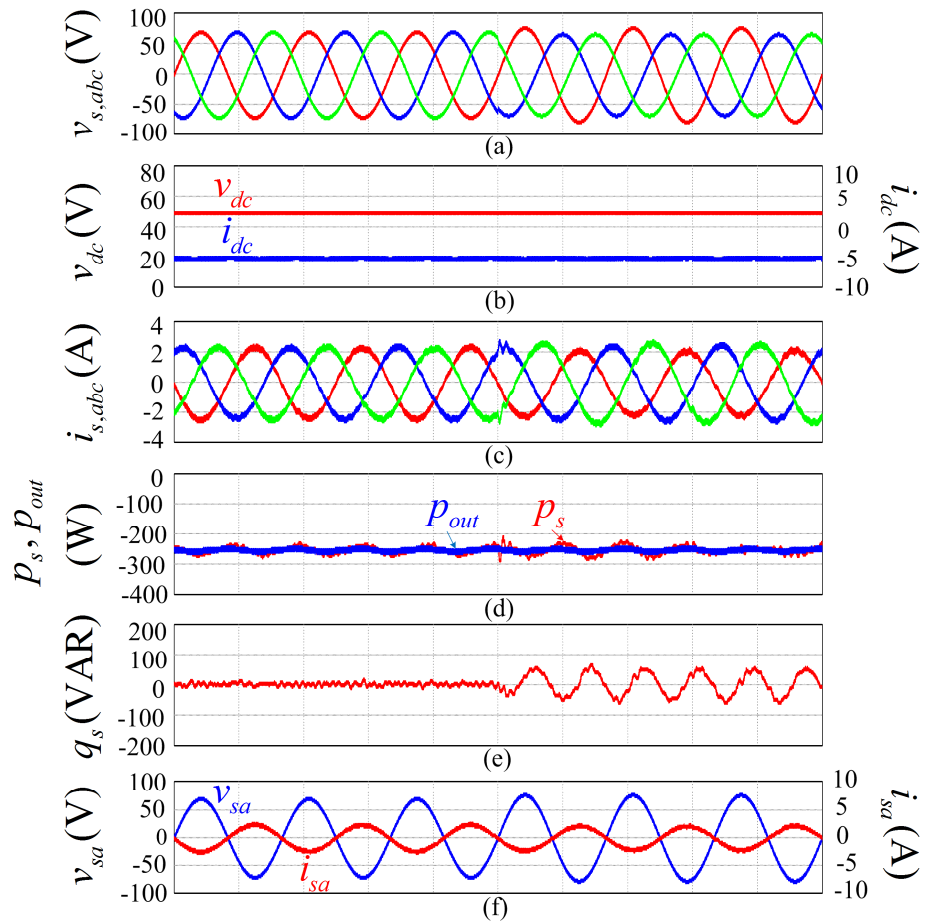
Figure 3.7 Performances of proposed ECS-PFC for inverter mode of the AC-DC MC (time: 10 ms/div): (a) Grid voltages, (b) output voltage and output current, (c) grid currents, (d) grid and output active powers, (e) grid reactive power, and (f) grid phase-*a* current and voltage.

As shown in Figure 3.6(b), the output voltage and output current are both constant no matter that the input voltage is balanced or not. Figure 3.6(c) shows that the grid current remains sinusoidal with THDs of 3.79% and 3.88% under the balanced and unbalanced grid voltage conditions, respectively. As shown in Figure 3.6(d), the converter provides constant output power even though the grid voltage becomes unbalanced. But, the instantaneous grid active power includes some ripples due to the input filter. Figure 3.6(e) shows that the average grid reactive power is kept at zero irrespective of its oscillation, which means that near unity input power factor is achieved under unbalanced grid voltage. And the grid current is in phase with the grid voltage as shown in Figure 3.6(f).

When the output current reference becomes -5 A, the AC-DC MC is changed to the inverter mode. Simulated results for the inverter mode are shown in Figure 3.7, which
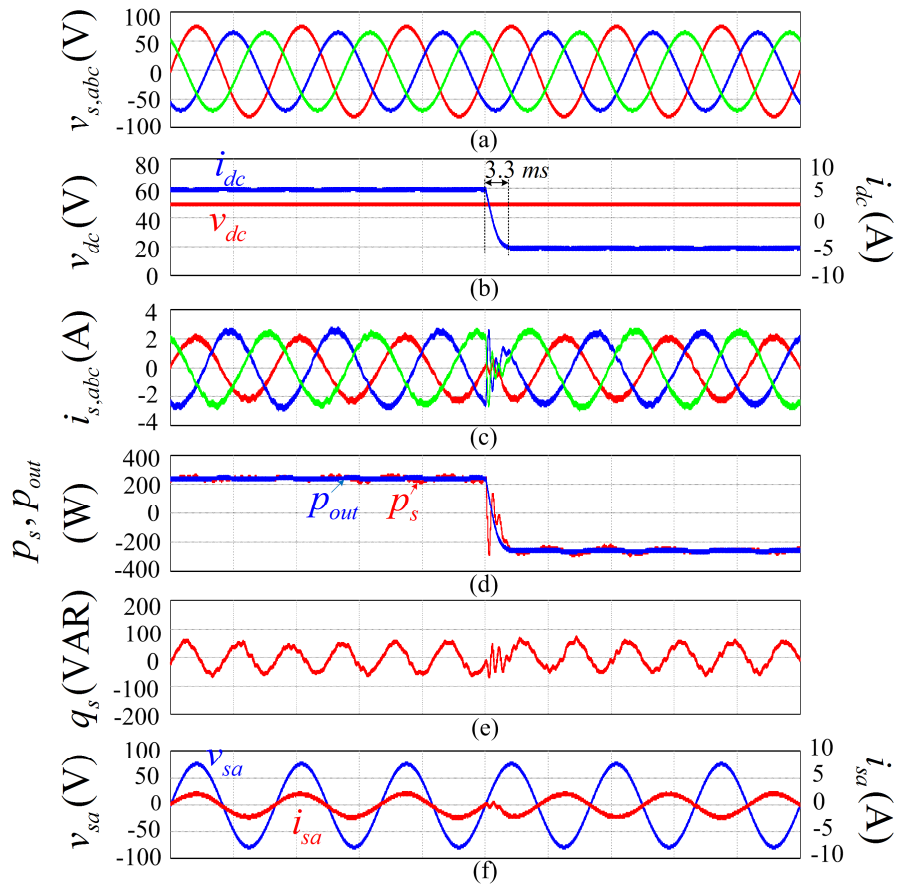
Figure 3.8 Performances of proposed ECS-PFC for mode change from rectifier to inverter of the AC-DC MC (time: 10 ms/div): (a) Grid voltages, (b) output voltage and output current, (c) grid currents, (d) grid and output active powers, (e) grid reactive power, and (f) grid phase-*a* current and voltage.

correspond with those in Figure 3.6 for the rectifier mode. In Figure 3.7(b), the output current becomes negative while the output voltage remains positive to supply active power to the grid. As shown in Figures 3.7(d) and (e), the output power is inverted with a near unity power factor by keeping zero average grid reactive power. As a result, the phase angle difference between the grid voltage and current becomes 180° in Figure 3.7(f). Similarly to the rectifier mode, Figure 3.7(c) shows the sinusoidal grid current with the THDs of 3.83% and 3.95% under the balanced and unbalanced grid voltage conditions, respectively. From Figures 3.6 and 3.7, it is clear that the proposed control strategy works well in both rectifier and inverter modes regardless of the grid voltage conditions.

Figure 3.8 shows the dynamic performance of the proposed control strategy for the mode change between the rectifier and inverter under unbalanced grid voltage conditions.
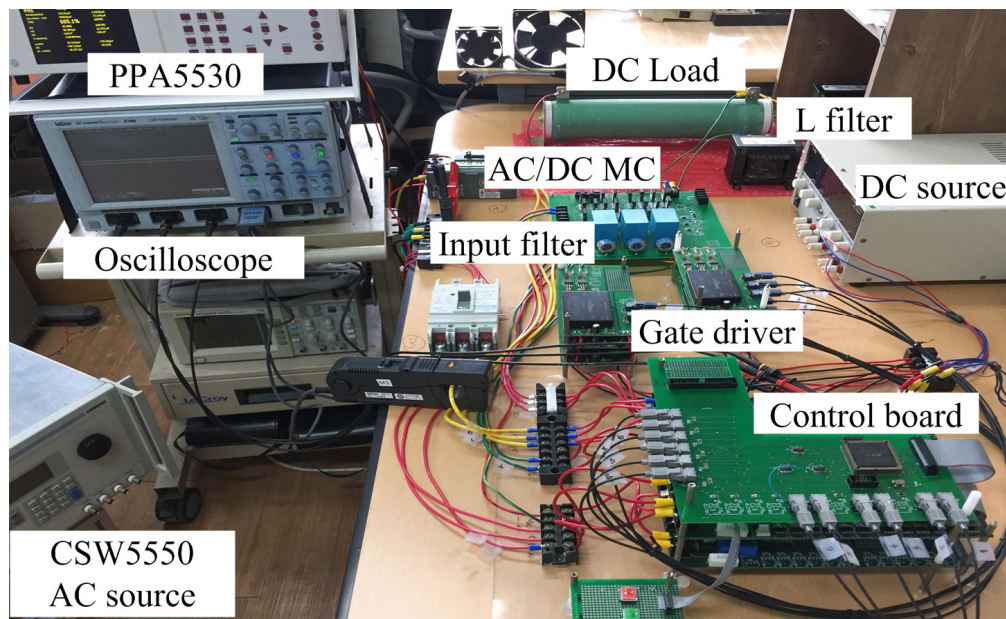
Figure 3.9 Experimental setup for AC-DC MC.

The output current reference is changed from 5 A to -5 A at 0.05 s. Figure 3.8(b) shows that the output current is tracked accurately within a very short time (3.3 ms), and the active power flow is changed quickly as shown in Figure 3.8(d). The grid current is kept sinusoidal in both operation modes as shown in Figure 3.8(c), and its THD is 3.87% in the rectifier mode and 3.97% in the inverter mode. In Figures 3.8(e) and (f), we can see that the average grid reactive power is kept at zero, and the near unity power factor is achieved regardless of the operation modes of the AC-DC MC.

3.6   Experimental Results

The prototype AC-DC MC in Figure 3.9 was implemented for experimental verification. The control system was realized using a 32-bit floating DSP TMS320F28335, and a EPM7128SLC84-15 was used to perform the four-step commutation. The AC/DC MC power system is configured by 12 IRG4PF50WD IGBTs, and the unbalanced grid voltage is provided by an Ametek CSW5550 programmable AC power source with positive and negative voltage sequences of $\mathbf{V_p} = 70\text{V} \angle 0^\text{o}$ and $\mathbf{V_n} = 7\text{V} \angle 0^\text{o}$, which results an unbalance level of 10%. The negative voltage sequence $\mathbf{V_n}$ is zero in the balanced case. Since the rectifier and inverter modes of the AC/DC MC are controlled by the same controllers
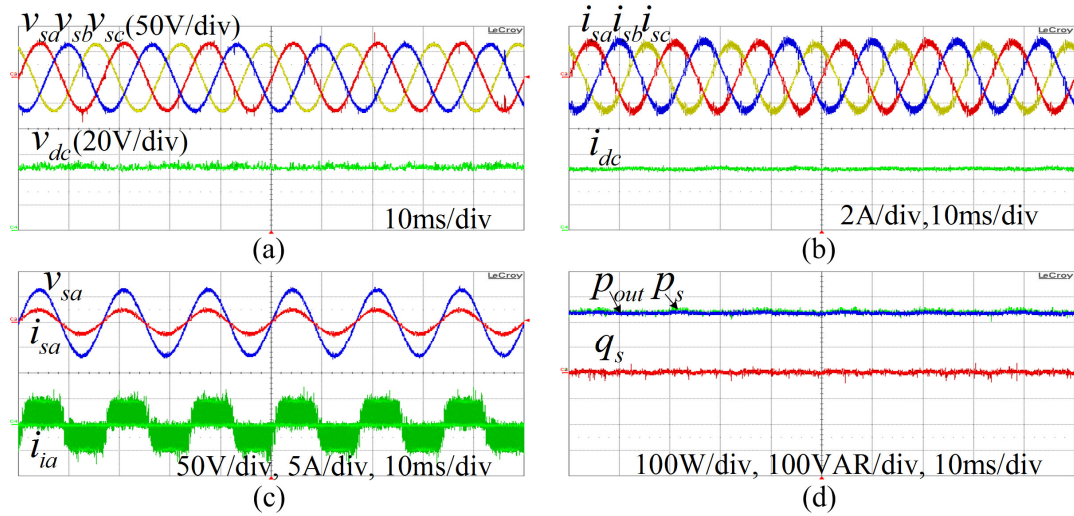
Figure 3.10 Experiment results of the proposed ECS-PFC under balanced grid voltage: (a) grid and output voltages, (b) grid and output currents, (c) phase-a input current, grid voltage, and grid current, and (d) grid active power, output power, and grid reactive power.

depending on the output current reference, they have similar performance as shown in simulated results. In experiment, the performance of the rectifier mode is effectively investigated with passive resistance load. The parameters in the experiment were the same as those used in the simulation as listed in Table 3.1.

Figure 3.10 shows the experimental waveforms of the proposed ECS-PFC for the AC/DC MC under balanced grid voltage conditions. The output voltage reference is 50 V. In Figures 3.10(a) and (b), the output voltage and current are constant, and the grid current is balanced and sinusoidal under the balanced grid voltage. Figure 3.10(c) shows that the grid current is in phase with the grid phase voltage; that is, unity input power factor (IPF) is achieved, although the input current is lags behind the grid voltage. As shown in Figure 3.10(d), the grid reactive power is controlled to be zero, and the grid active power is equal to the output power with constant values. From Figure 3.10, it is clear that the proposed control strategy for the AC/DC MC works well under balanced grid voltage conditions.

Figures 3.11 and 3.12 show experimental comparisons of the proposed ECS-PFC with two conventional methods that use conventional SVM (Method I) and feedforward compensation (Method II) under unbalanced grid voltage conditions. The output voltage reference is 50 V, and the THDs were measured by using a PPA5530 Precision Power Analyzer. In the case of Method I, the output voltage and current contain double grid-
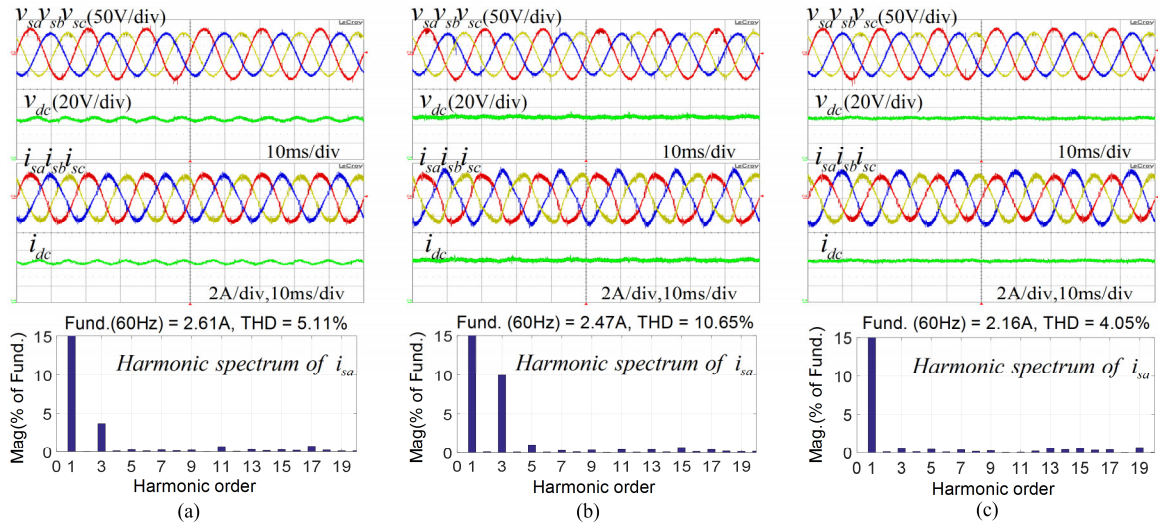
Figure 3.11 Experimental comparisons of grid, output voltage and current for three control methods under unbalanced grid voltages: (a) Method I, (b) Method II, and (c) proposed ECS-PFC.
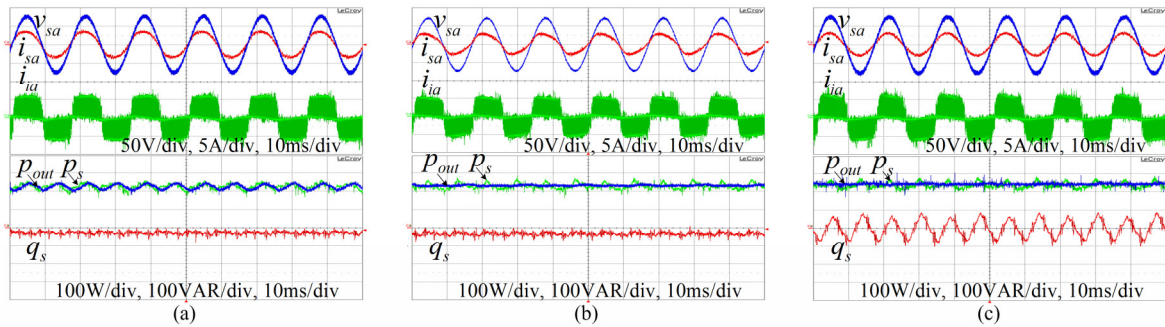
Figure 3.12 Experimental comparisons of IPF and powers for three control methods under unbalanced grid voltages: (a) Method I, (b) Method II, and (c) proposed ECS-PFC.

frequency ripples, and the grid current is highly distorted with THD of 5.11%, as shown in Figure 3.11(a). Method II shows severely distorted grid current with THD up to 10.65%, even though the output voltage and current are kept constant, as shown in Figure 3.11(b). In contrast, the output voltage and current with ECS-PFC are constant with almost sinusoidal grid current, as shown in Figure 3.11(c). The THD of the grid current is reduced to 4.05%, which complies with the IEEE Std 519 – 2014 standard [83], and the third- and fifth-order harmonic components are suppressed to 0.42% and 0.54%, respectively.

Figure 3.12 shows the experimental comparison for the IPF control performance for each control method. As shown in Figures 3.12 (a) and (b), the input current is controlled in phase

Table 3.2 Performance Comparison Corresponding to Output Voltage

Output voltage references V_{dc}^{ref}	Methods	Grid phase					
		a		*b*		*c*	
		THD of i_{sa} (%)	IPF	THD of i_{sb} (%)	IPF	THD of i_{sc} (%)	IPF
60V	Method I	4.70	0.990	5.05	0.985	4.86	0.986
	Method II	10.97	0.982	10.33	0.972	10.96	0.984
	ECS-PFC	3.53	0.999	2.89	0.987	3.24	0.989
50V	Method I	5.11	0.982	5.37	0.972	5.21	0.980
	Method II	10.65	0.969	10.43	0.957	10.85	0.987
	ECS-PFC	4.05	0.999	3.42	0.989	3.99	0.988
40V	Method I	5.62	0.954	5.47	0.939	5.87	0.955
	Method II	10.21	0.936	10.29	0.924	10.72	0.960
	ECS-PFC	4.81	0.996	4.17	0.990	4.63	0.985

with the input voltage with Method I and Method II by keeping the input power factor angle at zero. However, because of the input filter effect, the grid current leads in front of its corresponding grid voltage, and negative grid reactive power occurs. Consequently, the unity IPF is not achieved with Method I and Method II. In contrast, the average grid reactive power is always kept at zero with the proposed ECS-PFC, as shown in Figure 3.12(c), and a near unity IPF is achieved. As shown in Figure 3.12, the instantaneous grid and output active power oscillate with double fundamental frequency in Method I. But the output power with Method II and ECS-PFC is constant in spite of the instantaneous grid active power ripple due to the input filter. Thus, the proposed ECS-PFC shows superior performance in controlling the IPF compared to the conventional methods under unbalanced grid voltage conditions.

To evaluate the performance corresponding to the output voltage references, Table 3.2 shows the comparative analysis results of the THD and IPF with respect to the output voltage references of 40, 50, and 60 V. For all output voltage references, the proposed ECS-PFC has the lowest THD in the grid current. As the output voltage reference decreases, the IPF with Method I and Method II also decreases due to the increased displacement angle of
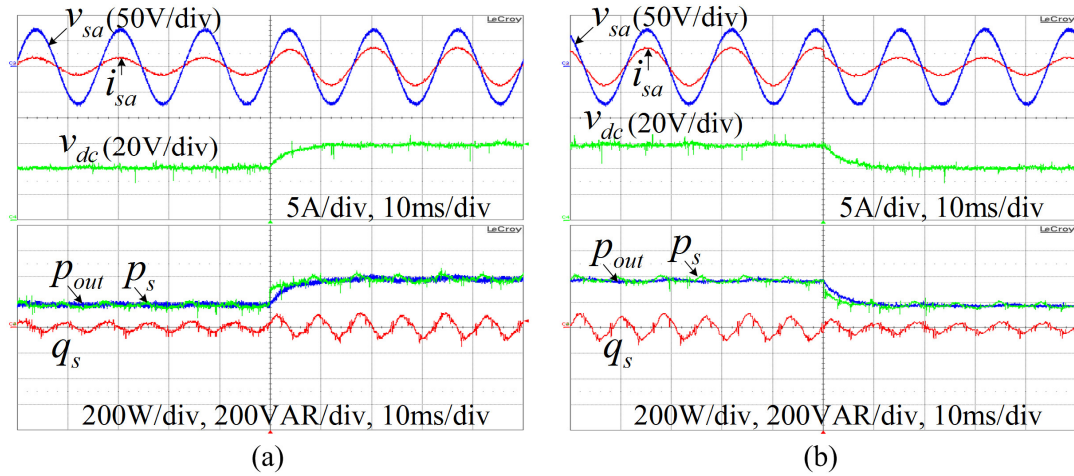
Figure 3.13 Experimental results of phase-*a* grid voltage, grid current, output voltage, grid active power, output power and grid reactive power for the proposed ECS-PFC with step change of output voltage reference: (a) from 40 to 60 V, (b) from 60 to 40 V.
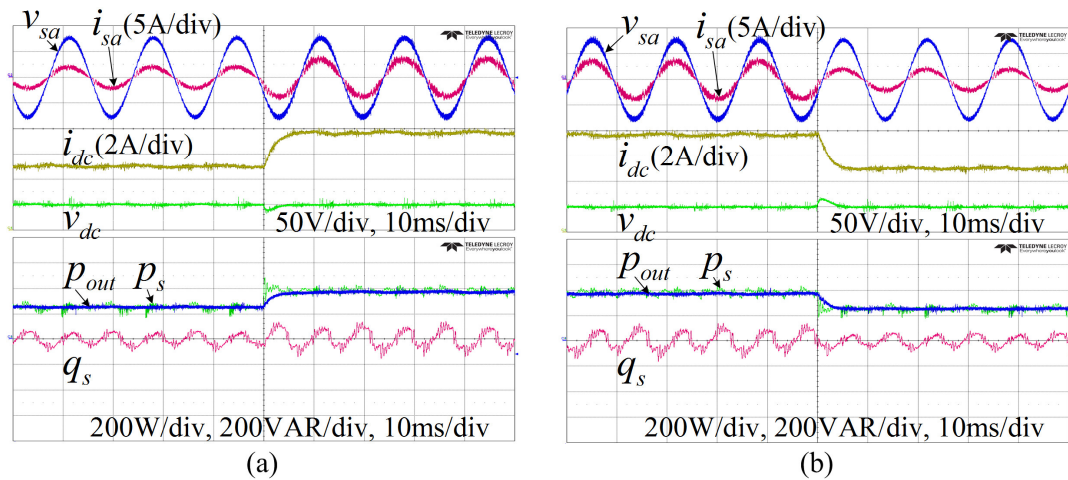
Figure 3.14 Experimental results of phase-*a* grid voltage, grid current, output current, output voltage, grid active power, output power and grid reactive power for the proposed ECS-PFC with the change of resistance load: (a) from 10 to 6.67 Ω, (b) from 6.67 to 10 Ω.

the input current [11]. From Table 3.2, it is clear that the proposed ECS-PFC has the best IPF performance, irrespective of the magnitude of the output voltage.

Figures 3.13(a) and (b) show the dynamic performance of the proposed ECS-PFC when the reference output voltage suddenly changes from 40 V to 60 V and then from 60 V to 40 V. The output voltage quickly tracks its reference value, and the average grid reactive power is always kept at zero during the transient period. Hence, the grid current is almost in phase

(a)   (b)
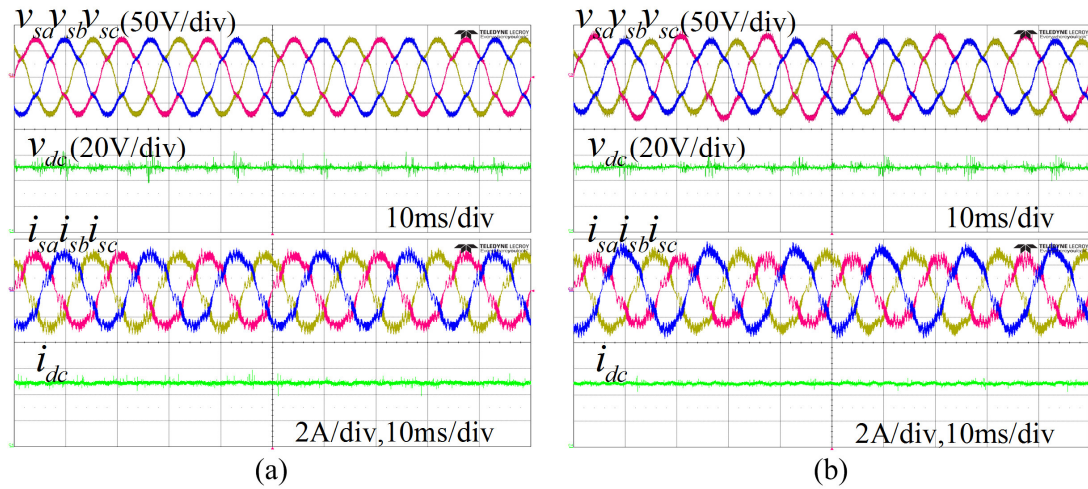
Figure 3.15 Experimental results of grid voltage, output voltage, grid current, and output current for the proposed ECS-PFC under: (a) balanced and distorted grid voltages, (b) unbalanced and distorted grid voltages.
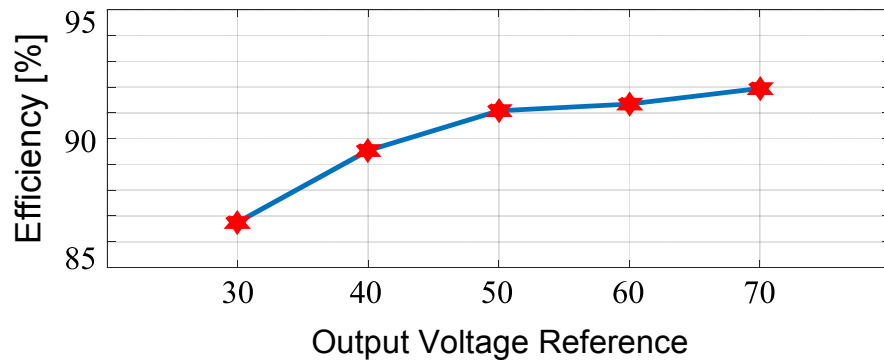
Figure 3.16 Overall efficiency under different output conditions.

with the grid voltage, and the IPF is near unity during the transient condition.

Figures 3.14(a) and (b) show the dynamic performance of the proposed ECS-PFC at the output voltage reference 50 V when the load resistance decreases from 10 Ω to 6.67 Ω and then increases from 6.67 Ω to 10 Ω, respectively. As we can see, the output voltage quickly tracks its reference value. Moreover, the grid current is almost in phase with the grid voltage with zero average grid reactive power. Thus, we can say that the near unity IPF is achieved in spite of the load variation.

Figures 3.15(a) and (b) show the performance of the proposed ECS-PFC under balanced/distorted and unbalanced/distorted grid voltage, respectively; the grid voltage is distorted

with fifth- and seventh-order harmonic components of 3.00% and 1.95%, respectively, and unbalanced with the unbalanced degree of 10%. Thanks to the output voltage-based PI controller, the output voltage and current are always kept constant in spite of the distorted grid voltage. The grid currents are distorted with the THDs of 6.27% and 6.76% under balanced/unbalanced and distorted grid voltage conditions.

In order to evaluate the efficiency of the proposed system, the grid active power and the output power have been experimentally measured for the various output voltage references of 30, 40, 50, 60, and 70 V as shown in Figure 3.16.

3.7 Summary

This chapter presented an effective control strategy for an AC/DC MC under unbalanced grid voltage to achieve constant output voltage, sinusoidal grid current, and near unity input power factor. The proposed control strategy provides an independent control scheme for the active and reactive power to realize constant active and average reactive power control for the AC/DC MC. By analyzing the instantaneous power model in a stationary frame, the input current reference was sinusoidally generated in spite of the unbalanced grid voltage. Therefore, the proposed method easily obtains sinusoidal grid current by directly synthesizing the input current reference. Furthermore, the input power factor becomes almost near unity by adjusting the zero average grid reactive power. The proposed method does not require extraction of the grid voltage sequence components or the controller of input current, so the control scheme can be implemented easily without large storage. The effectiveness of the proposed control strategy was verified by simulation and experimental results.

Chapter 4

Simplified MPC Scheme with Active Damping Function

The MPC is applied to AC-DC MCs to achieve fast dynamic response and simple implementation. However, the large number of calculations required for a conventional MPC (C-MPC) is an obstacle for its wide application. Moreover, active damping is used to mitigate LC resonance on the input side, which increases the computational burden of the C-MPC. The control performance of the C-MPC also deteriorates under unbalanced grid voltage conditions. To overcome these problems, this chapter presents a simplified MPC (S-MPC) for AC-DC MCs to reduce the computational burden. A novel method is proposed to realize the active damping function, which involves a damping function in the S-MPC without increasing the calculation time. Thus, the system performance is easily improved by shortening the sampling period. Furthermore, the grid current reference is generated based on a quantitative analysis of the power flow to achieve constant output current, sinusoidal grid current, and an input power factor near unity under unbalanced grid voltage. A simulation and experiment were done to verify the effectiveness of the proposed control method.

4.1   Introduction

Recently, MPC is emerging as an attractive method to control power converters due to its simple and intuitive concept, fast dynamic response, and easy inclusion of nonlinearities and constraints [84], [85]. Because of the discrete nature of the converter, a discrete model is used to select the optimal switching state by minimizing the cost function. Therefore, only one switching state is applied to drive the converter in each sampling period, and no modulation stage is needed.

In spite of these advantages, the conventional MPC (C-MPC) for an AC-DC MC still has some issues to be solved. An LC filter is required on the input side of the AC-DC MC to reduce the high-frequency input current harmonics caused by the switching operation and the pollution from the AC supply. However, the MPC can easily cause LC resonance due to the wide input current harmonic spectrum. To design an LC input filter effectively, it is very important to damp the LC resonance. In case of the passive damping method, a physical resistor is commonly inserted in parallel or series with filter inductor [21], [86]. This method is easy to implement, but results in excessive power losses. To overcome this drawback, several active damping methods have been realized without affecting the converter efficiency by emulating a virtual resistor in parallel with the filter capacitor [67]–[71]. In [67] and [68], the output current reference is modified by adding the damping current which is calculated in the *dq* synchronous frame based on the high-frequency components of the capacitor voltage. In another study, the *dq*-axis damping current is directly controlled with the aid of the cost function for the MPC [70]. However, these methods in [67], [68], and [70] need complicated *dq*-transformation, and their transient responses are degraded since DC-blocker or high-pass digital filter is used to obtain the high-frequency components of the capacitor voltage. To avoid these problems, the damping current was calculated in the αβ stationary frame without a digital filter [71]. Because the calculated damping current in [71] includes all high-frequency components of the capacitor voltage, the grid current waveform quality may be deteriorated. In order to reduce the high-frequency components included on damping current, a low-pass filter is incorporated in damping current calculation to

compromise with the decreased damping performance [69]. Even though the system performance is enhanced, the computational burden of the C-MPC with the active damping function is significantly increased due to the additional calculations for the damping current.

To reduce the computational burden, some simplified MPC methods have been proposed for converter under balanced grid voltage conditions [87]–[91]. In [87] and [88], the number of candidate vectors to evaluate the cost function was reduced by using a lookup table. In [89], the required voltage vector is introduced to simplify the MPC for the VSC and three-level neutral point clamped converter. This idea has been extended for MPC of MC to eliminate the prediction of the control variable and to reduce the number of candidate vectors for the cost function evaluation [90], [91]. The converter performance was improved due to the shorter sampling period.

Unbalanced grid voltage causes ripple on the DC side and low-order harmonics on the grid current of the AC-DC MC. The harmonic currents containing on the input current result in voltage distortion, increasing power losses and heat in the electrical equipment, torque pulsation and noise in motors, and causing malfunction and failure of electronic equipment [92]. Thus, it should be managed properly to keep the desired input and output power quality. To drive the MC normally through unbalanced grid voltages, most studies have focused on SVM [52], [55]–[60]. However, only a few works have considered the control problem under unbalanced grid voltages for MPC, in spite of its superiority. The grid current has been controlled to be balanced and sinusoidal, regardless of the unbalanced grid voltage [93], [94]. However, according to the power balance principle, it is impossible to simultaneously achieve a balanced sinusoidal grid current and ripple-free on the DC side of the AC-DC MC under unbalanced grid voltages. By generating different grid current references for the MPC, another study achieved various control targets, such as instantaneous active-reactive power, balanced sinusoidal grid current, or unbalanced sinusoidal grid current and ripple-free active power [95]. However, only simulation verification is given and the grid current reference generation needs to extract the positive and negative sequence components of the grid voltage, which increases the computational burden.

To solve these problems, this chapter proposes a simplified MPC (S-MPC) with an active damping function for an AC-DC MC under unbalanced grid voltage conditions. The

control objectives are provided to achieve sinusoidal grid current, an input power factor near unity, and constant output current. The grid current reference is generated by analyzing the instantaneous power model of the AC-DC MC in a stationary frame without information about the positive and negative sequence components of the grid voltages. Furthermore, the prediction process is simplified by computing only one required input current vector (RICV) instead of nine grid current predictions. In addition, a novel method is proposed to realize the active damping function without increasing the computational burden by integrating the damping current into the RICV. Therefore, the damping current predictions are not required for all possible switching states of the AC-DC MC. Thus, the execution time of the S-MPC is significantly reduced compared to that of the C-MPC, which improves the system performance thanks to the reduced sampling period. Simulation and experimental results are presented to demonstrate the effectiveness of the proposed S-MPC method.

4.2 Conventional MPC for AC-DC MC

4.2.1 Predictive Model of AC-DC MC

Figure 4.1 shows the configuration of the AC-DC MC studied in this chapter. It consists of a three-phase AC supply, input LC filter, an AC-DC MC with six bidirectional power switches, an output L filter, and a resistance load R. The input-side dynamic model of the AC-DC MC has the following space-state representation:

$$\begin{bmatrix} \dot{\mathbf{v}}_i \\ \dot{\mathbf{i}}_s \end{bmatrix} = A \begin{bmatrix} \mathbf{v}_i \\ \mathbf{i}_s \end{bmatrix} + B \begin{bmatrix} \mathbf{v}_s \\ \mathbf{i}_i \end{bmatrix}, \tag{4.1}$$

with $A = \begin{bmatrix} 0 & 1/C_f \\ -1/L_f & -R_f/L_f \end{bmatrix}$, $B = \begin{bmatrix} 0 & -1/C_f \\ 1/L_f & 0 \end{bmatrix}$,

where $\mathbf{v_i}$, $\mathbf{i_i}$, $\mathbf{v_s}$, and $\mathbf{i_s}$ are the input voltage, input current, grid voltage, and grid current vectors, respectively, and L_f, C_f, and R_f are the input filter parameters.

The dynamic model in (4.1) is discretized with a sampling period T_s:

$$\begin{bmatrix} \mathbf{v}_i(k+1) \\ \mathbf{i}_s(k+1) \end{bmatrix} = \Phi \begin{bmatrix} \mathbf{v}_i(k) \\ \mathbf{i}_s(k) \end{bmatrix} + \Gamma \begin{bmatrix} \mathbf{v}_s(k) \\ \mathbf{i}_i(k) \end{bmatrix}, \tag{4.2}$$
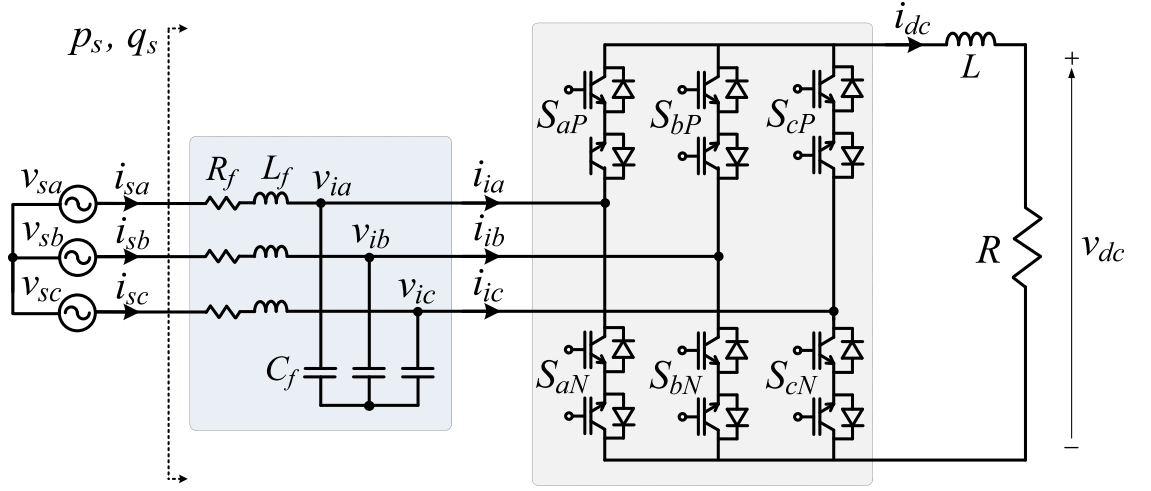
Figure 4.1 Configuration of the AC-DC MC.

where $\boldsymbol{\Phi} = e^{AT_s} = \mathcal{L}^{-1}\left[(s\mathbf{I} - A)^{-1}\right]$, $\boldsymbol{\Gamma} = A^{-1}(\boldsymbol{\Phi} - \mathbf{I}_{2\times 2})\boldsymbol{B}$.

From (4.2), the capacitor voltage and the grid current are predicted for all possible switching states based on the measured values of $\mathbf{v_i}(k)$, $\mathbf{i_s}(k)$, $\mathbf{v_s}(k)$, as well as the calculated value of $\mathbf{i_i}(k)$ by using (2.1) and (2.2):

$$\mathbf{v_i}(k+1) = \boldsymbol{\Phi}_{11}\mathbf{v_i}(k) + \boldsymbol{\Phi}_{12}\mathbf{i_s}(k) + \boldsymbol{\Gamma}_{11}\mathbf{v_s}(k) + \boldsymbol{\Gamma}_{12}\mathbf{i_i}(k), \tag{4.3}$$

$$\mathbf{i_s}(k+1) = \boldsymbol{\Phi}_{21}\mathbf{v_i}(k) + \boldsymbol{\Phi}_{22}\mathbf{i_s}(k) + \boldsymbol{\Gamma}_{21}\mathbf{v_s}(k) + \boldsymbol{\Gamma}_{22}\mathbf{i_i}(k). \tag{4.4}$$

4.2.2 Cost Function Design

The grid current in the AC-DC MC is coupled with the output current. Therefore, the grid current reference cannot be chosen arbitrarily to generate a desired output current. The amplitude and phase of the grid current reference are obtained separately using the active power balance and a phase-locked loop (PLL), respectively [91], [93]. However, because the current amplitude relies on the converter efficiency, it should be adjusted empirically, which leads to inconvenience in practical applications. To avoid this problem, the grid current reference is obtained directly from the grid active and reactive power reference without the PLL by using the instantaneous power theory [71]. The grid active power reference P_s^{ref} is determined from a PI controller that is used to regulate the output current. The grid current

reference is then calculated as follows [71]:

$$\begin{bmatrix} i_{s\alpha}^{ref} \\ i_{s\beta}^{ref} \end{bmatrix} = \frac{2}{3} \frac{P_s^{ref}}{v_{s\alpha}^2 + v_{s\beta}^2} \begin{bmatrix} v_{s\alpha} \\ v_{s\beta} \end{bmatrix} + \frac{2}{3} \frac{Q_s^{ref}}{v_{s\alpha}^2 + v_{s\beta}^2} \begin{bmatrix} v_{s\beta} \\ -v_{s\alpha} \end{bmatrix}, \tag{4.5}$$

where $i_{s\alpha}^{ref}$ and $i_{s\beta}^{ref}$ are the α and β components of the grid current reference, $v_{s\alpha}$ and $v_{s\beta}$ are the

α and β components of the grid voltage, and Q_s^{ref} is the grid reactive power reference.

To regulate the grid current, a cost function was developed from the error between the

current reference and its predicted value:

$$g = \left| i_{s\alpha}^{ref} - i_{s\alpha}(k+1) \right| + \left| i_{s\beta}^{ref} - i_{s\beta}(k+1) \right|, \tag{4.6}$$

where $i_{s\alpha}(k+1)$ and $i_{s\beta}(k+1)$ are the α and β components of the predicted grid current in (4.4).

In each sampling period, the switching state that results in the minimum cost function (4.6)

is applied to control the converter.

4.2.3 Delay Compensation

In the digital implementation of the MPC, there is an inevitable delay between the

measurement and the control output caused by the calculation time, which deteriorates the

performance of the system. To compensate for this delay, a two-step prediction method is

utilized [96]. The cost function for the tracking error at instant $k+2$ is evaluated instead of

instant $k+1$ and minimized to select the optimal switching state. The applied switching state

at instant k is used to estimate the capacitor voltage $\mathbf{v_i}(k+1)$ and grid current $\mathbf{i_s}(k+1)$ at

instant $k+1$ and based on (4.3) and (4.4), respectively. The grid current at instant $k+2$ is then

predicted for all nine possible switching states from (4.4):

$$\mathbf{i_s}(k+2) = \mathbf{\Phi}_{21} \mathbf{v_i}(k+1) + \mathbf{\Phi}_{22} \mathbf{i_s}(k+1) + \mathbf{\Gamma}_{21} \mathbf{v_s}(k+1) + \mathbf{\Gamma}_{22} \mathbf{i_i}(k+1), \tag{4.7}$$

where $\mathbf{v_s}(k+1)$ is considered to be equal to $\mathbf{v_s}(k)$ by ignoring the change in a short sampling

period, and $\mathbf{i_i}(k+1)$ is calculated using (2.1) and (2.2) by considering that i_{dc} is constant

during the prediction process due to the large inductor of the output filter.

To track the current at instant $k+2$, the cost function is modified as follows:

$$g = \left| i_{s\alpha}^{ref} - i_{s\alpha}(k+2) \right| + \left| i_{s\beta}^{ref} - i_{s\beta}(k+2) \right|, \tag{4.8}$$

where $i_{s\alpha}(k+2)$ and $i_{s\beta}(k+2)$ are the α and β components of the predicted grid current in
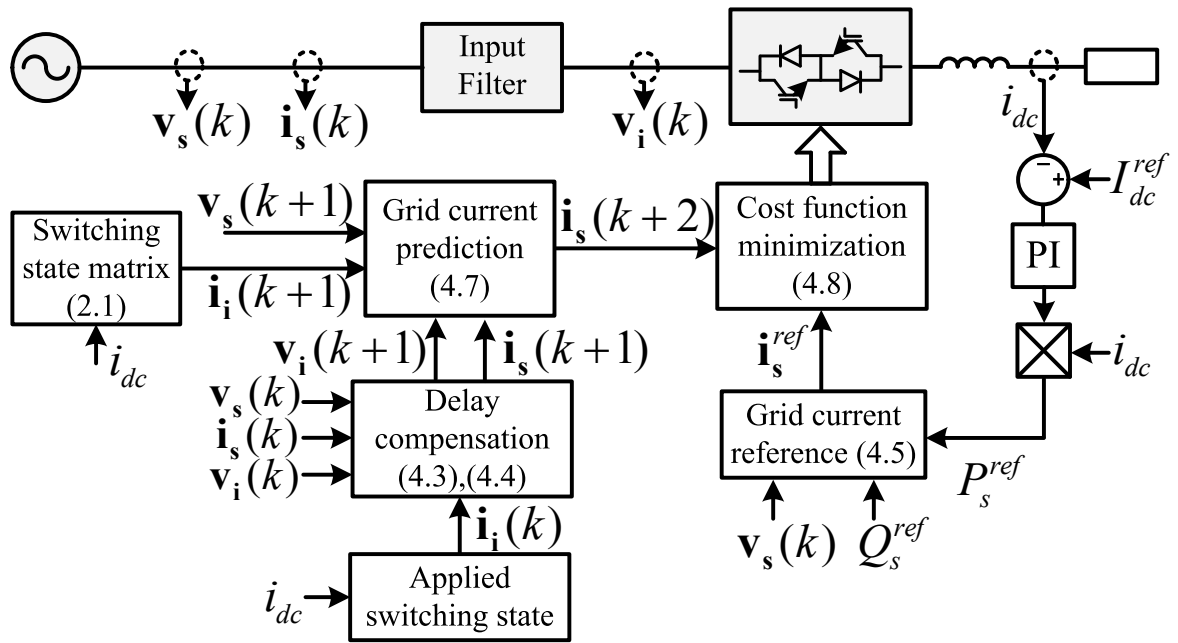
Figure 4.2 Block diagram of the C-MPC for the AC-DC MC.

(4.7). Figure 4.2 shows a control block diagram of the C-MPC for the AC-DC MC with delay compensation. During each sampling period, a large number of calculations are needed for all possible switching states, including nine grid current predictions (4.7) and nine cost function evaluations (4.8). The switching state that results in the minimum cost function (4.8) is applied to control the converter.

4.3 Simplified MPC for AC-DC MC

4.3.1 Grid Current Reference Generation

Under unbalanced grid voltage conditions, the grid current reference in (4.5) includes severe low-order harmonics due to the grid voltage negative sequence component. To solve this problem, the grid instantaneous power model for grid current reference generation is widely expressed based on the positive and negative sequence components of the grid voltage and current, but this normally increase the computational burden. To avoid this

drawback, a method to express the instantaneous power in terms of the grid voltage and current and their 90° lagging signals is applied. Similar to the theoretical analysis in Section 3.3.1, the grid instantaneous power model is obtained as follows:

$$p_s = \frac{3}{2}\mathrm{Re}(\mathbf{v_s}\mathbf{i_s^*}) = P_0 + P_{c2}\cos(2\omega t) + P_{s2}\sin(2\omega t), \tag{4.9}$$

$$q_s = \frac{3}{2}\mathrm{Im}(\mathbf{v_s}\mathbf{i_s^*}) = Q_0 + Q_{c2}\cos(2\omega t) + Q_{s2}\sin(2\omega t), \tag{4.10}$$

where

$$\begin{cases} P_0 = \frac{3}{4}(v_{s\alpha}i_{s\alpha} + v_{s\beta}i_{s\beta} + v'_{s\alpha}i'_{s\alpha} + v'_{s\beta}i'_{s\beta}) \\ P_{c2} = \frac{3}{4}(k_1\cos(2\omega t) + k_2\sin(2\omega t)) \\ P_{s2} = \frac{3}{4}(-k_2\cos(2\omega t) + k_1\sin(2\omega t)) \\ Q_0 = \frac{3}{4}(v_{s\beta}i_{s\alpha} - v_{s\alpha}i_{s\beta} + v'_{s\beta}i'_{s\alpha} - v'_{s\alpha}i'_{s\beta}) \\ Q_{c2} = \frac{3}{4}(k_3\cos(2\omega t) + k_4\sin(2\omega t)) \\ Q_{s2} = \frac{3}{4}(-k_4\cos(2\omega t) + k_3\sin(2\omega t)) \end{cases} \tag{4.11}$$

with

$$\begin{cases} k_1 = (v_{s\alpha}i_{s\alpha} + v_{s\beta}i_{s\beta} - v'_{s\alpha}i'_{s\alpha} - v'_{s\beta}i'_{s\beta}) \\ k_2 = (v'_{s\alpha}i_{s\alpha} + v'_{s\beta}i_{s\beta} + v_{s\alpha}i'_{s\alpha} + v_{s\beta}i'_{s\beta}) \\ k_3 = (v_{s\beta}i_{s\alpha} - v_{s\alpha}i_{s\beta} - v'_{s\beta}i'_{s\alpha} + v'_{s\alpha}i'_{s\beta}) \\ k_4 = (v'_{s\beta}i_{s\alpha} - v'_{s\alpha}i_{s\beta} + v_{s\beta}i'_{s\alpha} - v_{s\alpha}i'_{s\beta}), \end{cases} \tag{4.12}$$

$v_{s\alpha}$, $v_{s\beta}$, $i_{s\alpha}$, $i_{s\beta}$, $v'_{s\alpha}$, $v'_{s\beta}$, $i'_{s\alpha}$, and $i'_{s\beta}$ are the α and β components of the grid voltage, grid current, and their 90° lagging signals, respectively.

The current reference used to control the active and reactive power flows is determined by solving the set of power equations in (4.11). The control objectives are provided to achieve a constant output current, sinusoidal grid current, and input power factor near unity under unbalanced grid voltage conditions. For this purpose, the average active power P_0 should be equal to the grid active power reference P_s^{ref}, and the ripples of the active power P_{c2} and P_{s2} should be zero along with the average reactive power Q_0. The remaining ripples of the reactive power Q_{c2} and Q_{s2} are left to be uncontrolled, so reactive power ripples appear under unbalanced grid voltage conditions. These constraints are satisfied by the

following equations:

$$\begin{cases} P_0 = P_s^{ref} \\ Q_0 = 0 \\ P_{c2} = 0 \\ P_{s2} = 0 \end{cases} .$$ (4.13)

From (4.13), the grid current reference in the αβ frame is obtained as follows:

$$\begin{cases} i_{s\alpha}^{ref} = \dfrac{2P_s^{ref}}{3} \dfrac{v_{s\beta}'}{(v_{s\beta}'v_{s\alpha} - v_{s\beta}v_{s\alpha}')} \\ i_{s\beta}^{ref} = -\dfrac{2P_s^{ref}}{3} \dfrac{v_{s\alpha}'}{(v_{s\beta}'v_{s\alpha} - v_{s\beta}v_{s\alpha}')} \end{cases} .$$ (4.14)

The grid current reference becomes sinusoidal with a given constant value P_s^{ref}. However, it is unbalanced because the grid voltage is unbalanced. The unbalanced grid current leads to another control issue such as the converter trip if one of the phase currents exceeds its rated value, and the system operation reliability becomes worse. To solve this issue, many recently presented methods for a voltage source converter are directly applied to the AC-DC MC based on the current reference in (4.14). For example, in order to keep the maximum current within the limited value, the current reference is modified according to the ratio of the rated current and the maximum current [97], [98]. And also, some advanced methods have been presented to achieve the maximum allowable active and reactive power transfer capability as well as the maximum current limitation [99], [100].

4.3.2 Grid Current Prediction Elimination

The principle of the C-MPC with delay compensation is to select one input current vector $\mathbf{i_i}(k+1)$ from nine possible input current vectors, which makes the predicted grid current $\mathbf{i_s}(k+2)$ closest to the grid current reference $\mathbf{i_s}^{ref}$. To eliminate the nine grid current predictions in the C-MPC, the proposed S-MPC introduces a new variable RICV for prediction. The RICV $\mathbf{i_i}^{ref}(k+1)$ that makes $\mathbf{i_s}(k+2)$ close to its reference $\mathbf{i_s}^{ref}$ is determined from (4.7) by replacing $\mathbf{i_s}(k+2)$ with $\mathbf{i_s}^{ref}$:

$$\mathbf{i_i}^{ref}(k+1) = \frac{\mathbf{i_s}^{ref} - \mathbf{\Phi}_{21}\mathbf{v_i}(k+1) - \mathbf{\Phi}_{22}\mathbf{i_s}(k+1) - \mathbf{\Gamma}_{21}\mathbf{v_s}(k)}{\mathbf{\Gamma}_{22}}.$$ (4.15)
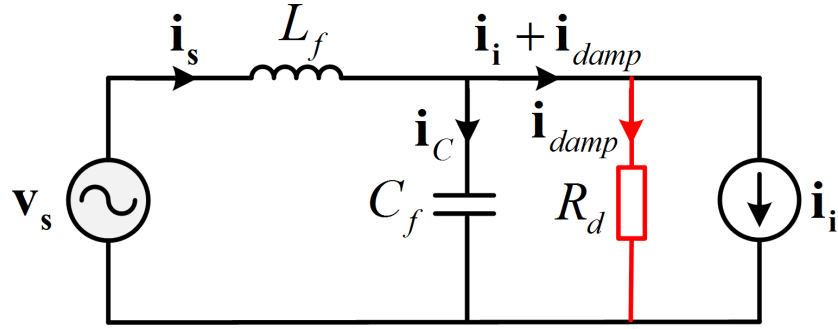
Figure 4.3 Principle of virtual resistor-based active damping method.

To select the input current vector that is closest to the RICV, a new cost function is defined as follows:

$$g = \left| i_{i\alpha}^{ref}(k+1) - i_{i\alpha}(k+1) \right| + \left| i_{i\beta}^{ref}(k+1) - i_{i\beta}(k+1) \right|, \tag{4.16}$$

where $i_{i\alpha}(k+1)$ and $i_{i\beta}(k+1)$ are the α and β components of the input current vector at instant $k+1$. The cost function in (4.16) is evaluated for all nine possible switching states, and only one switching state that leads to the minimum value of (4.16) is applied to control the AC-DC MC. Even though the number of the cost function calculations of both the S-MPC and C-MPC is the same, 9 grid current predictions (4.7) are not required in (4.16); only one calculation of the RICV (4.15) is needed. It means that the total number of calculations of the S-MPC to find the most effective switching state is significantly reduced compared to that of the C-MPC. Thus, the overall computational burden is reduced and the computing time is shortened.

4.4   Simplified MPC with Active Damping Function

4.4.1 Active Damping Principle

As shown in Figure 4.3, the active damping function can mitigate the LC resonance without affecting the converter efficiency by emulating the virtual damping resistor R_d in parallel with the filter capacitor [67]–[71]. Since the active damping is meant to mitigate the system harmonics, only the harmonic capacitor voltage v_i^h is considered to calculate the

damping currents:

$$\mathbf{i}_{damp} = \frac{\mathbf{v}_i^h}{R_d}. \tag{4.17}$$

To avoid using a digital filter to extract $\mathbf{v}_i^h$, the damping current is simply calculated as follows [71]:

$$\mathbf{i}_{damp} = \frac{\mathbf{v}_i + j\omega L_f \mathbf{i}_s^{ref} - \mathbf{v}_s}{R_d}. \tag{4.18}$$

Then, from Figure 4.3, the grid current becomes:

$$\mathbf{i}_s = \mathbf{i}_C + \mathbf{i}_i + \mathbf{i}_{damp}. \tag{4.19}$$

From (4.19), the active damping function can be realized by directly injecting the damping current into the grid current reference. Considering delay compensation, the grid current reference is modified as follows:

$$\mathbf{i}_{s\_new}^{ref} = \mathbf{i}_s^{ref} + \mathbf{i}_{damp}(k+2), \tag{4.20}$$

where $\mathbf{i}_{damp}(k+2)$ is the damping current at instant $k+2$:

$$\mathbf{i}_{damp}(k+2) = \frac{\mathbf{v}_i(k+2) + j\omega L_f \mathbf{i}_s^{ref} - \mathbf{v}_s(k+2)}{R_d}, \tag{4.21}$$

where $\mathbf{v}_s(k+2)$ is considered to be equal to $\mathbf{v}_s(k)$, and $\mathbf{v}_i(k+2)$ is calculated from (4.3):

$$\mathbf{v}_i(k+2) = \mathbf{\Phi}_{11}\mathbf{v}_i(k+1) + \mathbf{\Phi}_{12}\mathbf{i}_s(k+1) + \mathbf{\Gamma}_{11}\mathbf{v}_s(k+1) + \mathbf{\Gamma}_{12}\mathbf{i}_i(k+1). \tag{4.22}$$

By regulating the grid current reference in (4.22), the damping function can be involved in the MPC. There are 9 possible input currents $\mathbf{i}_i(k+1)$ that produce 9 possible input voltages in (4.22), and 9 current damping calculations in (4.21) corresponding to 9 possible input voltages in (4.22) are additionally required to find the most effective switching state by means of the C-MPC with active damping function. Thus, the current damping calculation significantly increases the computational burden of the C-MPC.

4.4.2 Simplified MPC with Active Damping Function

To reduce the computational burden of the S-MPC, a novel realization method is proposed with an active damping function. By replacing $\mathbf{i}_s^{ref}$ in (4.15) with $\mathbf{i}_{s\_new}^{ref}$ in (4.20), the RICV is modified as follows:

Figure 4.4 Block diagram of the S-MPC with active damping function for the AC-DC MC.

$$\mathbf{i}_{\mathbf{i}\_new}^{ref}(k+1) = \frac{(1+jC_5)\mathbf{i}_{\mathbf{s}}^{ref} + C_1\mathbf{v}_{\mathbf{i}}(k+1) + C_2\mathbf{i}_{\mathbf{s}}(k+1) + C_3\mathbf{v}_{\mathbf{s}}(k)}{C_4}, \qquad (4.23)$$

where $C_5 = \omega L_f / R_d$, $C_1 = (\Phi_{11}/R_d - \Phi_{21})$, $C_2 = (\Phi_{12}/R_d - \Phi_{22})$, $C_3 = ((\Gamma_{11}-1)/R_d - \Gamma_{21})$, and $C_4 = (\Gamma_{22} - \Gamma_{12}/R_d)$ are constant values. To regulate the RICV in (4.23), the following cost function is used:

$$g = \left| i_{i\alpha\_new}^{ref}(k+1) - i_{i\alpha}(k+1) \right| + \left| i_{i\beta\_new}^{ref}(k+1) - i_{i\beta}(k+1) \right|. \qquad (4.24)$$

As we can see from (4.24), only one calculation of the RICV (4.23) is required to evaluate the cost function of the proposed S-MPC with active damping function. Therefore, the computational burden of the S-MPC is significantly reduced compared to that of the C-MPC.

Figure 4.4 shows a control block diagram of the S-MPC with active damping function for the AC-DC MC under unbalanced grid voltage condition. A SOGI is used to obtain the lagging signal of the grid voltage because it can track the fundamental component of the grid voltage with zero error, even if the grid voltage is disturbed [82].

In order to select the appropriate virtual damping resistance R_d, the transfer function between the grid current and the converter current is obtained from Figure 4.3:

Table 4.1 Simulation and Experimental Parameters

Parameter	Value
Power supply	$\mathbf{V_p} = 70\text{V}\angle 0^0, f_i = 60 \text{ Hz}$
Input filter	$L_f = 1.2 \text{ mH}, C_f = 20 \ \mu\text{F}, R_d = 19.3 \ \Omega$
Output	$L = 10 \text{ mH}, R = 10 \ \Omega$

$$G_I(s) = \frac{i_s(s)}{i_i(s)} = \frac{\dfrac{1}{L_f C_f}}{s^2 + \dfrac{1}{R_d C_f}s + \dfrac{1}{L_f C_f}}. \tag{4.25}$$

The virtual damping resistance R_d is calculated from (4.25) based on the LC input parameters and the desired damping factor ξ:

$$R_d = \frac{1}{2\xi}\sqrt{\frac{L_f}{C_f}} \tag{4.26}$$

As well known, increasing damping factor ξ results in better damping performance, but it leads to lower value of damping resistor. It is obvious from (4.17) that lower value of damping resistor leads to higher damping current containing high frequency components, which may deteriorate the grid current quality in the MPC. In this study, the damping factor is selected as $\xi = 0.2$, and the virtual damping resistance is determined as $R_d = 19.3 \ \Omega$ from (4.26) with the system parameters given in Table 4.1.

4.5   Simulation Results

A simulation was carried out using PSIM software to compare the performance of the proposed S-MPC with the C-MPC. A degree of unbalance of 10% was applied by injecting a negative sequence voltage $\mathbf{V_n}=7\text{V} \angle 0^o$ and the positive sequence voltage $\mathbf{V_p}=70\text{V} \angle 0^o$, respectively. When the grid voltage is balanced, $\mathbf{V_n}$ is zero. The other parameters are listed in Table 4.1.
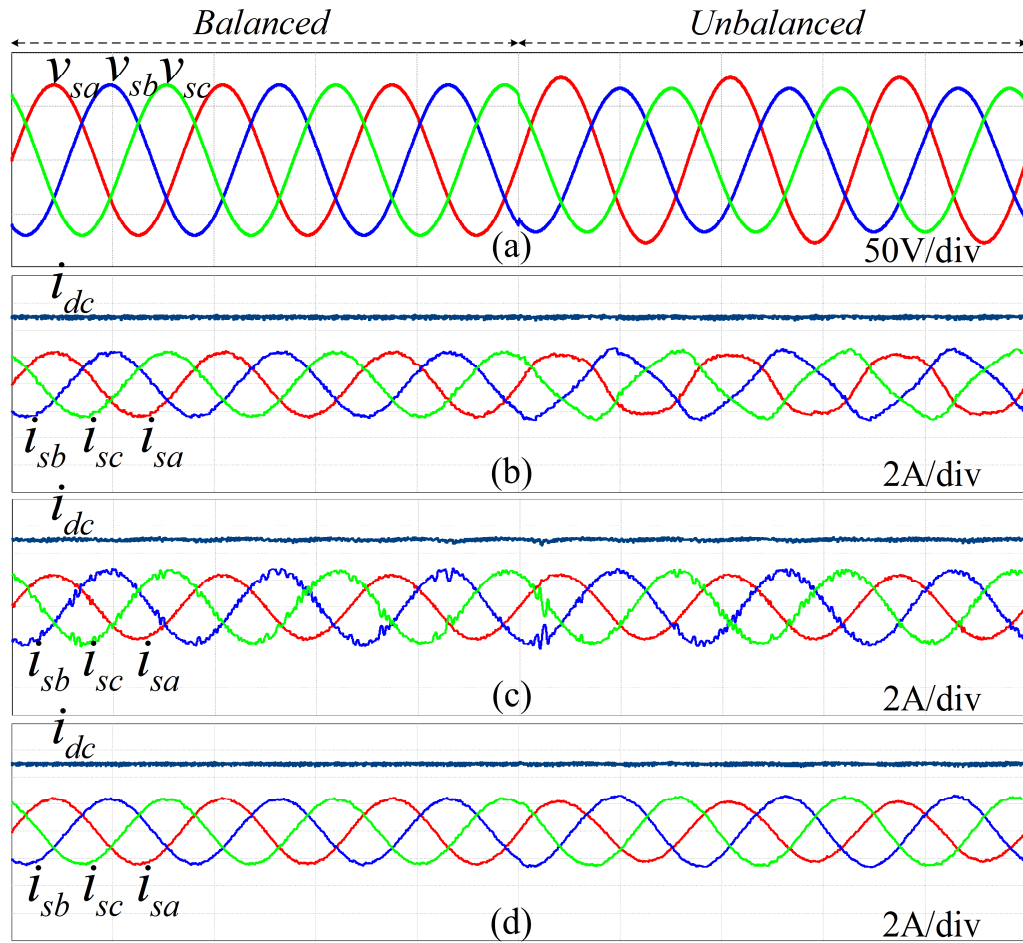
Figure 4.5 Simulation results of converter performance under balanced and unbalanced grid voltage (time: 10 ms/div): (a) Grid voltage, (b) Method I, (c) Method II, and (d) Method III.

4.5.1 Waveform Quality Comparisons

Figure 4.5 shows a performance comparison for the C-MPC with the active damping function (Method I), S-MPC without the active damping function (Method II), and S-MPC with the active damping function (Method III) when the balanced grid voltage becomes unbalanced at t = 0.05 s. The sampling period for the three methods is $T_s = 40 \ \mu s$. The output current reference is fixed at 5 A, and the three-phase grid voltage is illustrated in Figure 4.5(a). As shown in Figures 4.5(b), (c), and (d), all the control methods achieve constant output current irrespective of the grid voltage conditions due to the PI controller regulating the output current.

In the first half part of Figure 4.5, both Method I and Method III show the sinusoidal grid current, which means the performance of the S-MPC is equal to that of the C-MPC
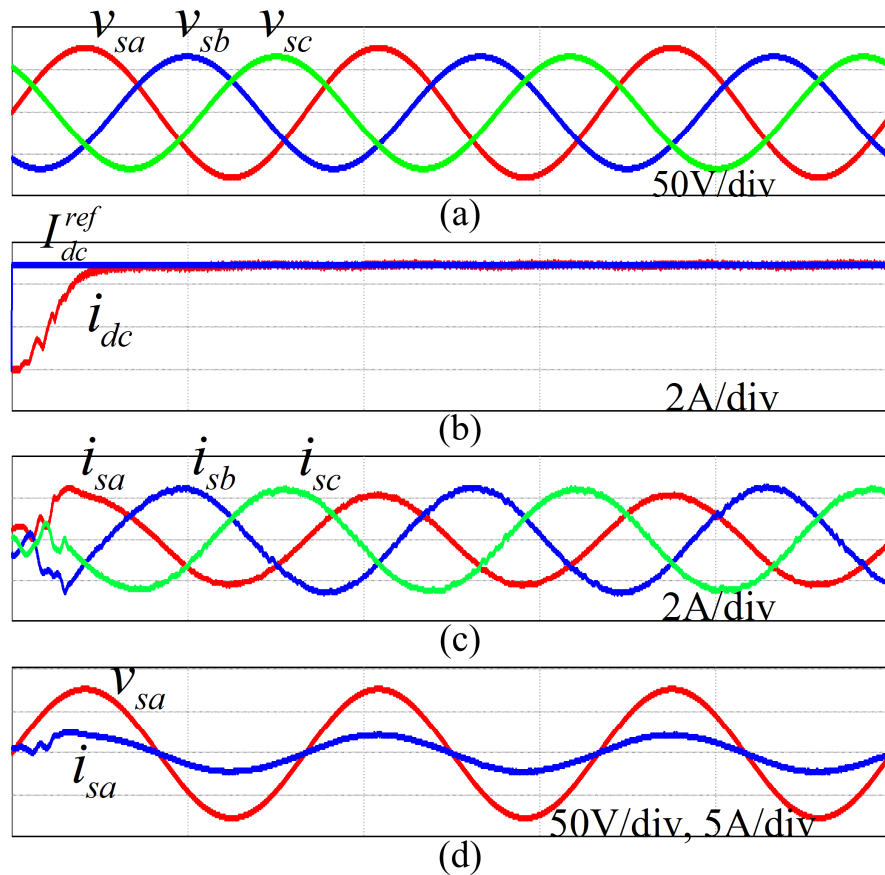
Figure 4.6 Performances of the proposed S-MPC with a suddenly change of output current reference (time: 10ms/div): (a) Grid voltages, (b) output current reference and output current, (c) grid currents, and (d) phase-*a* grid current and grid voltage.

when the balanced grid voltage is provided with same sampling period. However, because the grid current reference in the C-MPC for the AC-DC MC is determined without considering the unbalanced grid voltage conditions, the grid current becomes distorted when the grid voltage becomes unbalanced, as shown in the latter half part of Figure 4.5(b). In Figure 4.5(c), the grid current with Method II includes oscillations due to the limited damping coefficient of the input LC filter. Thanks to the active damping function, the oscillations in the grid current are suppressed with Method III, and sinusoidal grid current is achieved regardless of the grid voltage conditions, as shown in Figure 4.5(d). Thus, the proposed S-MPC with active damping function shows good performance under both balanced and unbalanced grid voltage conditions.

Figure 4.6 shows the performance of the Method III under unbalanced grid voltage with the output current reference changes suddenly from 0 to 5 A. The unbalanced grid voltage is

shown in Figure 4.6(a). Figure 4.6(b) shows that the output current is tracked accurately within a very short time (5 ms), and the grid current is become sinusoidal when the output current reaches its steady-state value as shown in Figure 4.6(c). Figure 4.6(d) shows that the grid current is in phase with the grid voltage, which means that near unity input power factor is achieved quickly during the startup process.

4.5.2 Influence of Shortening Sampling Period

In order to show the influence of the shortening sampling period on the average switching frequency, switching losses, overall efficiency and the grid current waveform quality, we have investigated the S-MPC and compared to the C-MPC for various output current. The average switching frequency of the MPC means the average value of the switching frequencies of all the power switches in the power circuit [101]:

$$f_{avg} = \sum_{x=\{a,b,c\}, \, y=\{P,N\}} \frac{\overline{f}_{xy}}{6}, \tag{4.27}$$

where $\overline{f}_{xy}$ is the average switching frequency of the power switch S_{xy}, which is obtained from the total number of the commutations n_{xy} of the switch S_{xy} during a time period t_f, i.e., $\overline{f}_{xy} = n_{xy} / t_f$. It is worth noting that the switching losses do not only depend on the average switching frequency, but also on the losses of the power switch during one commutation, which is proportional to the variation of the current and voltage involved in the commutation process [39]:

$$P_{sw} = k\Delta i_c \Delta v_{ce}, \tag{4.28}$$

where k is the proportional constant, i_c is the collector current and v_{ce} is the collector-emitter voltage of the power switch. The switching losses are calculated by using a thermal module in PSIM 9.0 software with IGBT-type IRG4PF50WD. The overall efficiency of the system η is calculated as follows:

$$\eta = \frac{P_{out}}{P_s} \times 100\%, \tag{4.29}$$

where P_{out} is the output power and P_s is the grid active power. The THD is used to reflect the grid current waveform quality:
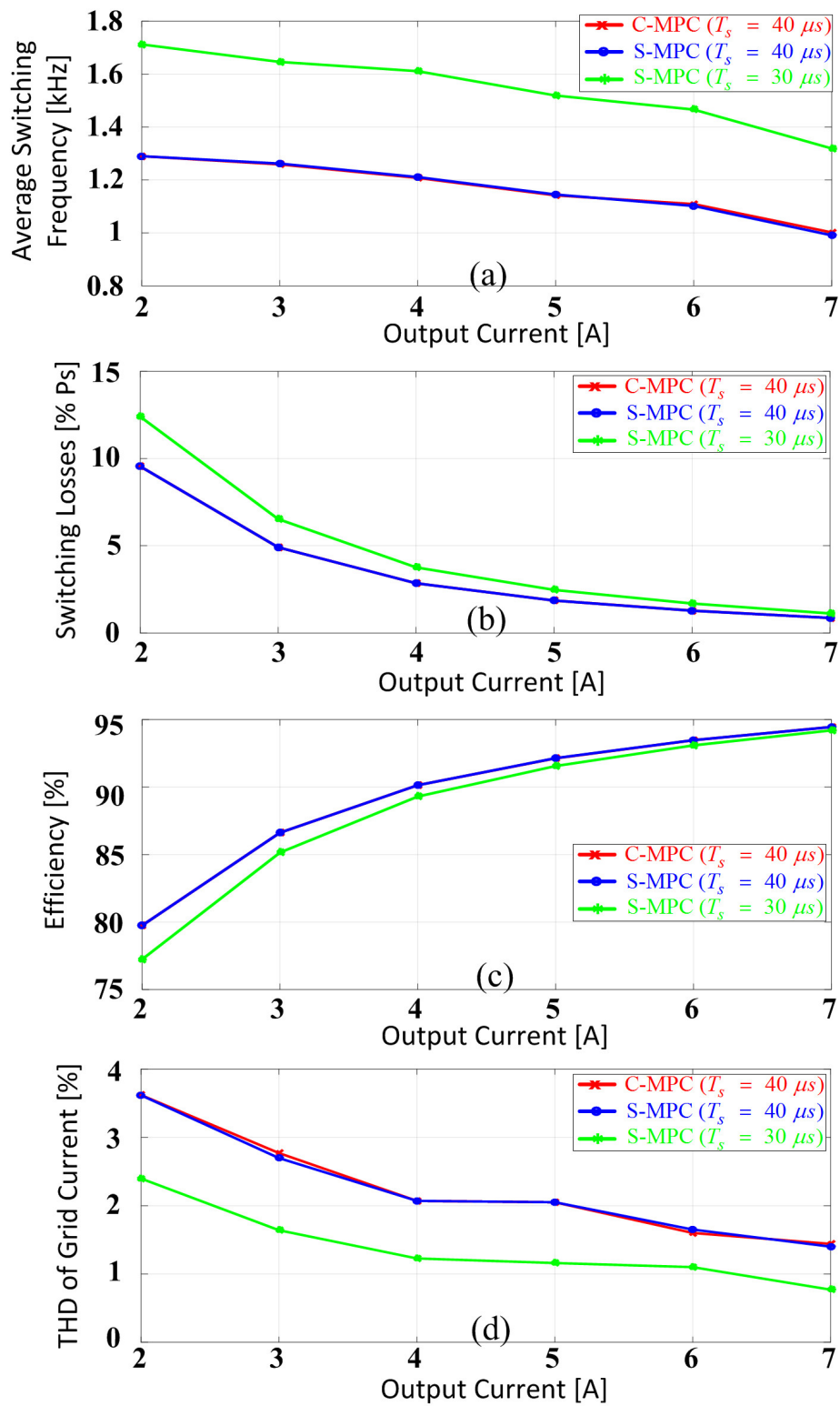
Figure 4.7 Simulation comparison of the Method I and Method III in terms of (a) the average switching frequency, (b) switching losses, (c) overall efficiency, and (d) THD of grid current versus various output currents under balanced grid voltage condition.
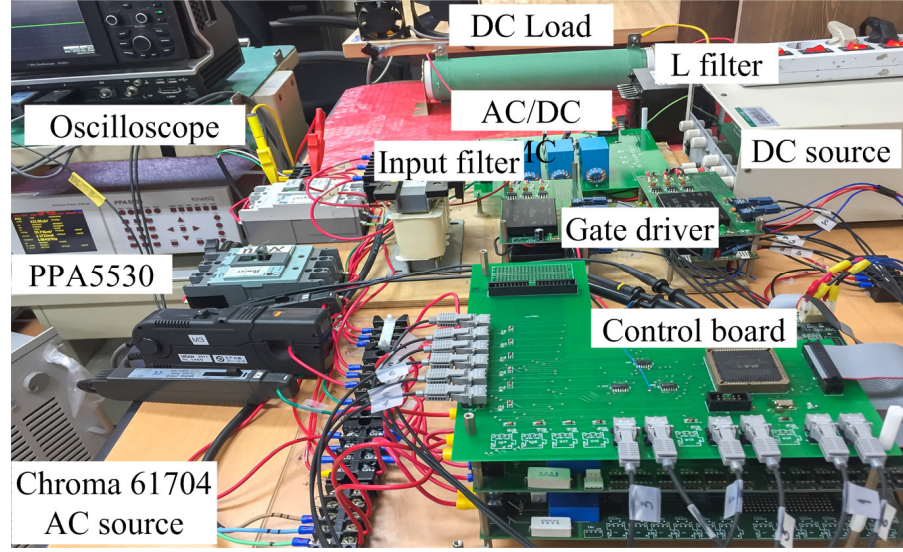
Figure 4.8 Experimental set-up for AC-DC MC.

$$THD = \frac{\sqrt{I_{rms}^2 - I_1^2}}{I_1} \times 100\%, \tag{4.30}$$

where I_1 is the RMS value of the fundamental current component and I_{rms} is the overall RMS value of the current.

Figure 4.7 shows the comparisons of the Method I with sampling period $T_s = 40\ \mu s$, Method III with sampling period $T_s = 40\ \mu s$, and Method III with sampling period $T_s = 30\ \mu s$ for (a) the average switching frequency, (b) switching losses, (c) overall efficiency, and (d) THD of grid current versus various output current under balanced grid voltage condition, respectively. Comparing with the same sampling period $T_s = 40\ \mu s$, the performance of the Method III is similar as that of the Method I as we can see from Figure 4.8(a) to (d). In case of the Method III with sampling period $T_s = 30\ \mu s$, the method with shorter sampling period has higher average switching frequency as shown in Figure 4.8(a). In Figures 4.8(b) and (c), even though the method with shorter sampling period has higher switching losses and lower overall efficiency, those switching losses and overall efficiency become approximately the same at higher load conditions. Moreover, Figure 4.8(d) shows the THD of grid current is reduced significantly by means of the shorter sampling period method for all load conditions. Therefore, the proposed S-MPC is definitely effective when the high waveform quality is expected.
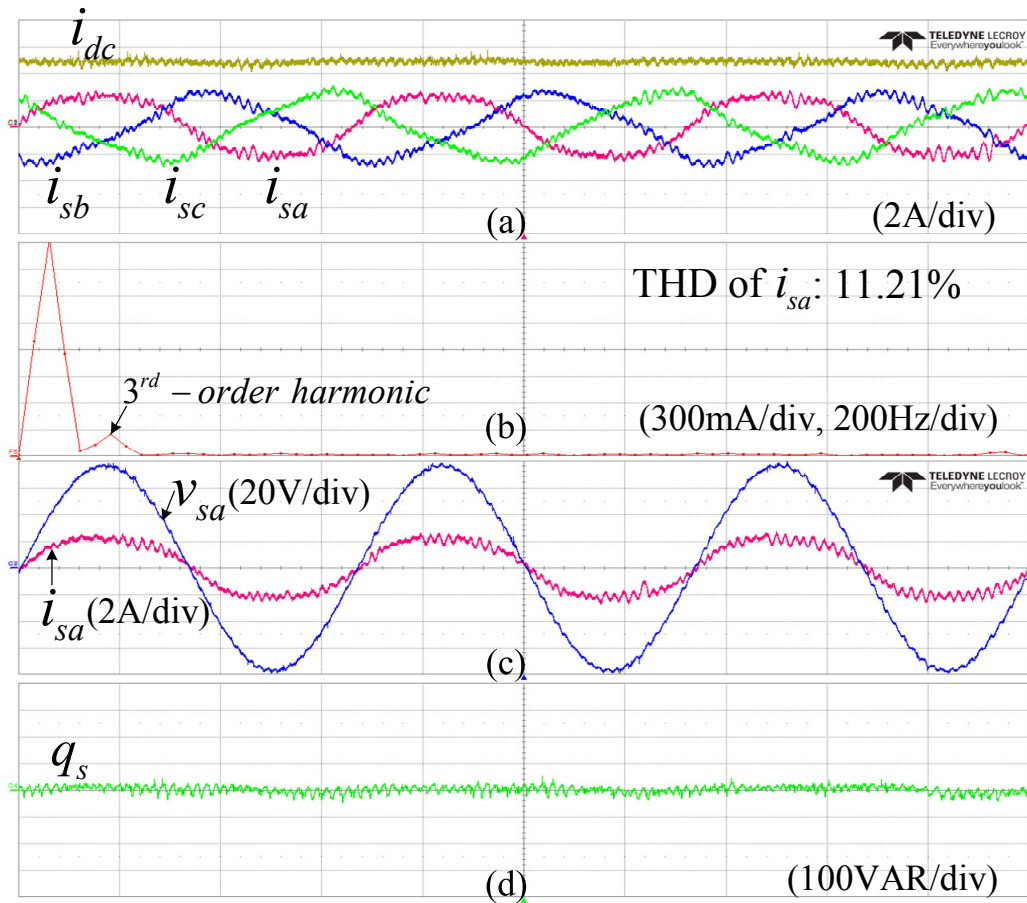
Figure 4.9 Experiment results of Method I under unbalanced grid voltage (time: 5 ms/div): (a) grid and output currents, (b) FFT spectrum of phase-*a* grid current, (c) phase-*a* grid current and grid voltage, (d) grid reactive power.

4.6 Experimental Results

The prototype AC-DC MC in Figure 4.8 was implemented to verify the effectiveness of the proposed method. The control system was designed with a DSP TMS320F28335 and a CPLD EPM7128SLC84-15. The AC-DC MC was realized by 12 IRG4PF50WD IGBTs, and the unbalanced grid voltage was provided by a Chroma 61704 programmable AC power source with positive and negative voltage sequences of $V_p=70V \angle 0^o$ and $V_n=7V \angle 0^o$, which result in a degree of unbalance of 10%. The parameters in the experiment were the same as those used in the simulation in Table 4.1, and all experimental results were tested under unbalanced grid voltage conditions.
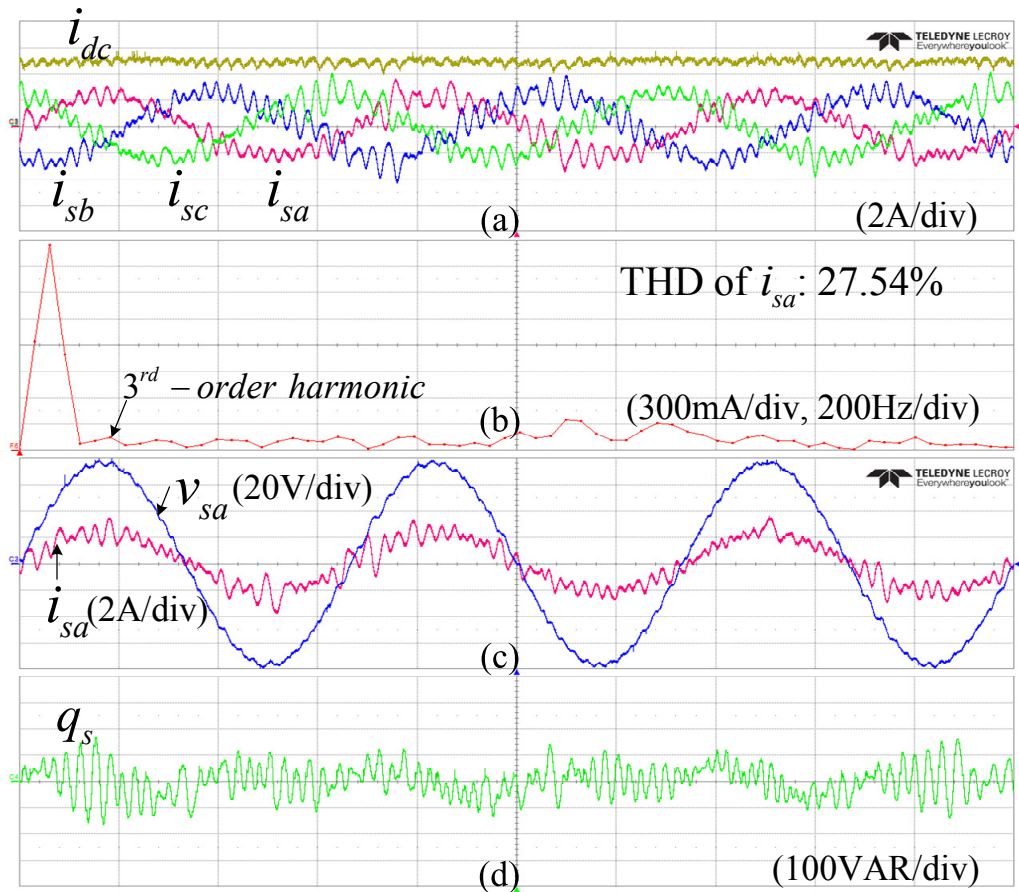
Figure 4.10 Experiment results of Method II under unbalanced grid voltage (time: 5 ms/div): (a) grid and output currents, (b) FFT spectrum of phase-*a* grid current, (c) phase-*a* grid current and grid voltage, (d) grid reactive power.

In Figures 4.9, 4.10, and 4.11, the system performance is compared for Method I, Method II, and Method III. The sampling period was set to $T_s = 40 \ \mu s$ for the three methods. The output current reference was 5 A, and THDs of the grid current were measured using a PPA5530 Precision Power Analyzer. As shown in Figures 4.9(a) and (b), Method I keeps the output current constant, but it causes a highly distorted grid current with a remarkable third-order harmonic and THD of 11.21% because the grid current reference in the Method I is determined without considering the unbalanced grid voltage conditions. The instantaneous grid reactive power is controlled to be zero in Method I, so the grid current is in phase with the grid voltage, and the grid reactive power is almost zero, as shown in Figure 4.9(c) and 4.9(d).
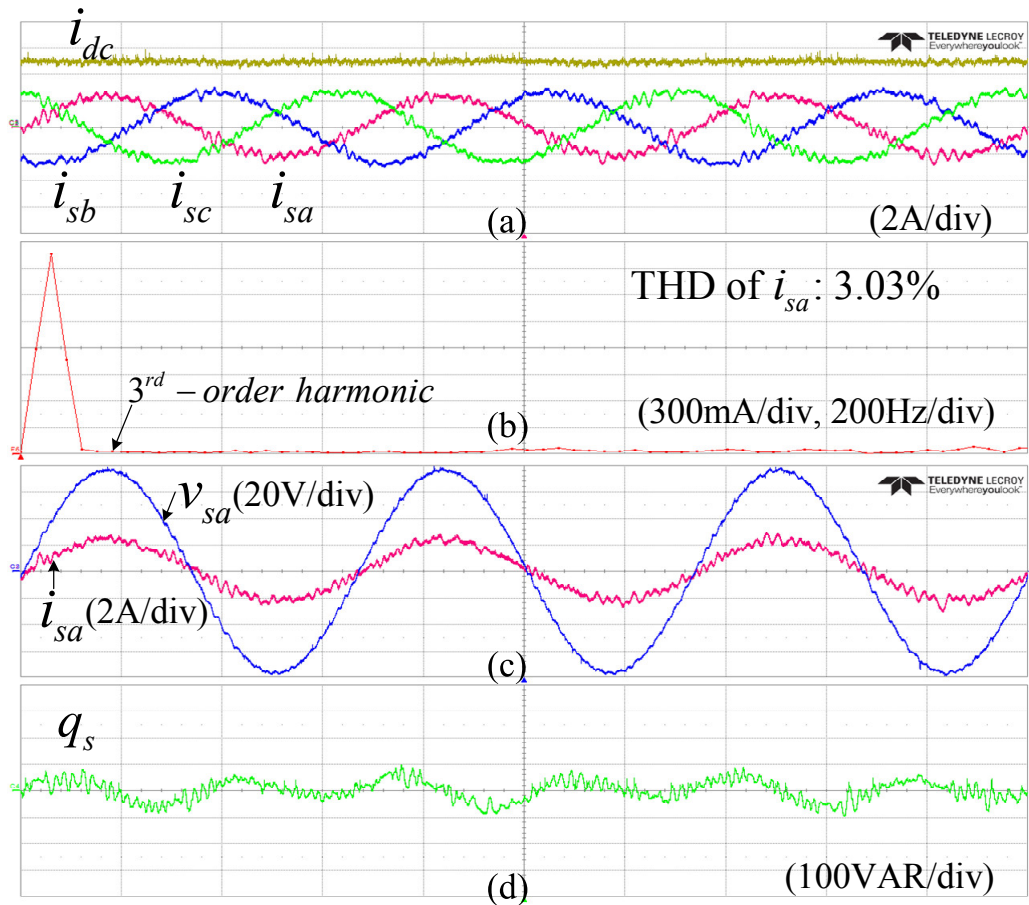
Figure 4.11 Experiment results of Method III under unbalanced grid voltage (time: 5 ms/div): (a) grid and output currents, (b) FFT spectrum of phase-*a* grid current, (c) phase-*a* grid current and grid voltage, (d) grid reactive power.

Figure 4.10 shows the performance of Method II. There are severe oscillations in the grid current in Figure 4.10(a), which leads to large output current ripple. As shown in Figure 4.10(b), the third-order harmonic of the grid current is reduced compared to Method I due to the quantitative analysis of the power flow. However, the THD of the grid current with Method II is increased to 27.54% due to the limited damping coefficient of the input LC filter. As shown in Figure 4.10(c), the grid current is not in phase with the grid voltage because the large grid reactive power ripple in Figure 4.10(d) makes it hard for the input power factor to be unity.

Method III shows reduced output current ripple and damped grid current oscillation due to the active damping function, as shown in Figure 4.11(a). In Figure 4.11(b), the third-order

Table 4.2 Comparison of Execution Times

Tasks	Execution times (μs)		
	Method I	Method II	Method III
Current reference calculation	9.29	10.06	10.10
Prediction and cost function evaluation	16.25	7.13	7.04
Other algorithms (ADC, SPI,…)	10.61	10.46	10.59
Total	36.15	27.65	27.73

Table 4.3 Comparison of the Number of Calculation

Tasks			Number of calculation		
			Method I	Method II	Method III
Current reference calculation	Grid current reference generation	$\mathbf{i}_\mathbf{s}^{ref}$	1	1	1
	RICV generation	$\mathbf{i}_\mathbf{i}^{ref}(k+1)$ or $\mathbf{i}_{\mathbf{i}\_new}^{ref}(k+1)$	-	1	1
	Damping current calculation	$\mathbf{v}_\mathbf{i}(k+2)$	9	-	-
		$\mathbf{i}_{damp}(k+2)$	9	-	-
Prediction and cost function evaluation	Delay compensation	$\mathbf{v}_\mathbf{i}(k+1)$	1	1	1
		$\mathbf{i}_\mathbf{s}(k+1)$	1	1	1
	Grid current prediction	$\mathbf{i}_\mathbf{s}(k+2)$	9	-	-
	Cost function	g	9	9	9
	Total		39	13	13

harmonic of the grid current is eliminated, and the THD of the grid current is significantly reduced to 3.03%. Furthermore, the grid current is in phase with the grid voltage, and the average grid reactive power is kept at zero, even though it is oscillating, as shown in Figure 4.11(c) and (d). This means that the near-unity input power factor is achieved with Method III. Thus, Method III shows superior performance in controlling the grid current compared to Method I and Method II under unbalanced grid voltage conditions.

Table 4.2 shows a comparison of the execution time for Method I, Method II, and Method III. Since the lagging signal of the grid voltage needs to be extracted, the time to calculate the current reference with the S-MPC (Method II and III) is slightly longer than
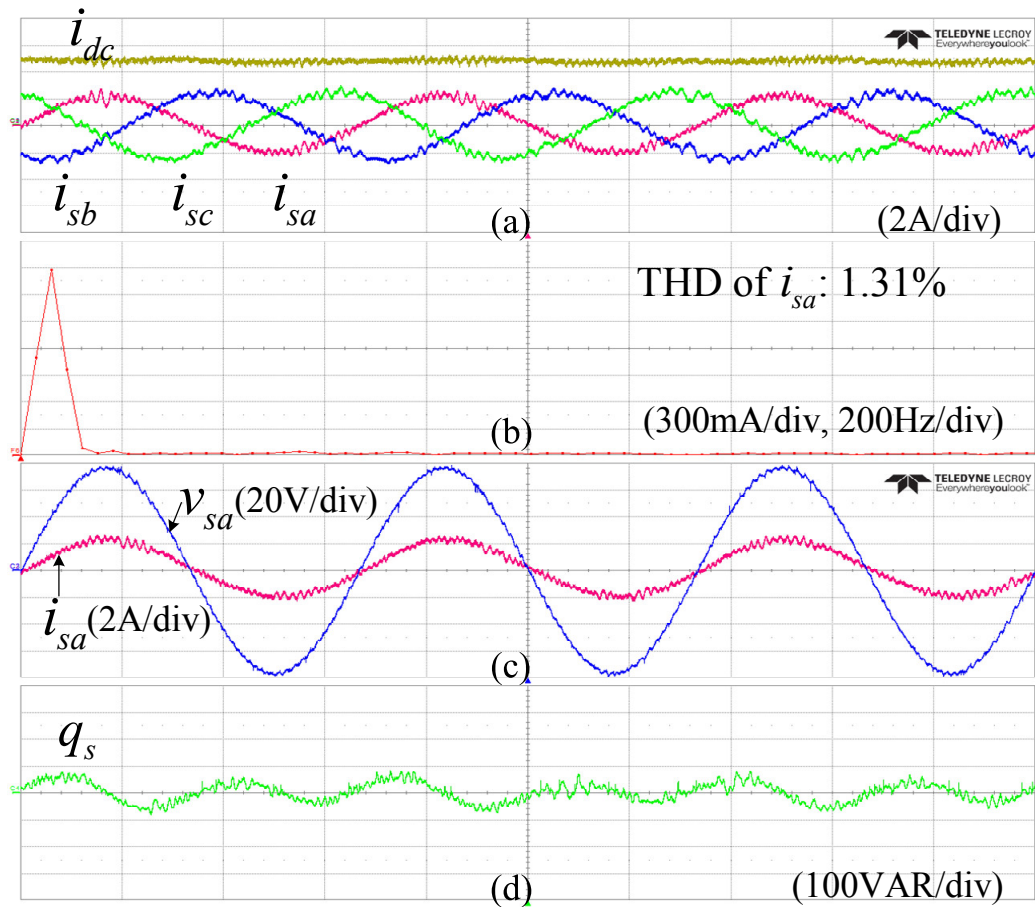
Figure 4.12 Experiment results of Method III with $T_s = 30 \ \mu s$ under unbalanced grid voltage (time: 5 ms/div): (a) grid and output currents, (b) FFT spectrum of phase-a grid current, (c) phase-a grid current and grid voltage, (d) grid reactive power.

that with the C-MPC (Method I). However, thanks to the simplification of the prediction procedure, the time for the prediction and cost function evaluation in the S-MPC is reduced more than 50% compared to that of the C-MPC. Thus, the total execution time is significantly reduced by the S-MPC, which enables enhanced system performance by shortening the sampling period. Furthermore, due to the novel method to calculate the RICV, the total execution time of Method III is almost the same as that of Method II, even though the active damping function is involved. For more intuition, Table 4.3 summarizes the number of the required calculation for each task in these methods.

From Table 4.2, we can apply a shorter sampling period for the S-MPC. Figure 4.12 shows the performance of the Method III with sampling period $T_s = 30 \ \mu s$. Compared with

(a)

(b)
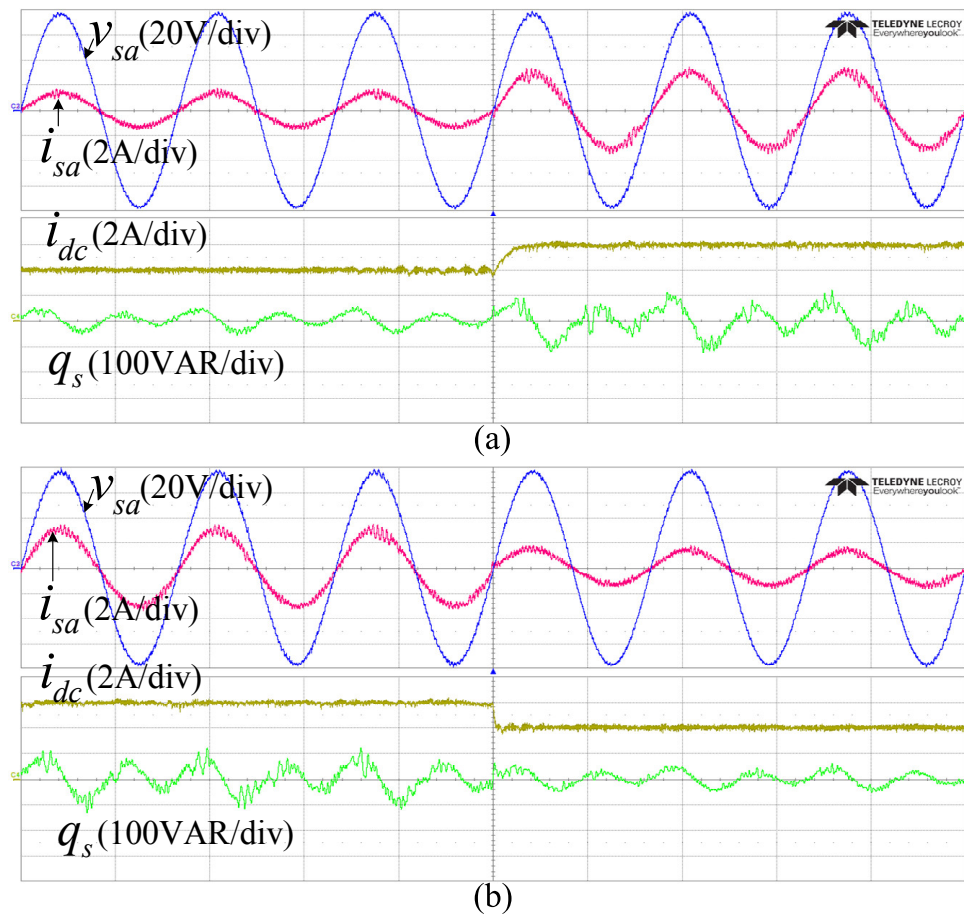
Figure 4.13 Experiment results of the phase-*a* grid voltage and current, output current, and grid reactive power for Method III with T_s = 30 μs under unbalanced grid voltage with step change of output current reference (time: 10 ms/div): (a) from 4 A to 6 A, (b) from 6 A to 4 A.

Figure 4.11, the performance of the system is improved much more. The THD of the grid current is reduced to 1.31%, and there is lower ripple in the grid reactive power.

Figures 4.13(a) and (b) show the dynamic performance of Method III with sampling period T_s = 30 μs when the output current reference suddenly changes from 4 to 6 A and from 6 to 4 A. The output current quickly tracks its reference, and the average grid reactive power is always kept at zero during the transient period. Thus, the grid current is almost in phase with the grid voltage, and an input power factor near unity is achieved in spite of the change in the output current reference.

4.7   Summary

This chapter has proposed an S-MPC with an active damping function for AC-DC MC under unbalanced grid voltage to achieve constant output current, sinusoidal grid current, and an input power factor near unity. The proposed method calculated only one RICV instead of nine grid current predictions, which significantly reduced the computing time. Furthermore, the novel realization method was proposed to involve the active damping function in the S-MPC without increasing the computational burden. Therefore, the execution time of the S-MPC was significantly reduced compared to that of the C-MPC, and the system performance was improved much better thanks to the reduced sampling period.

Chapter 5

Grid Voltage Sensorless Model Predictive Control Scheme with Virtual Current Vector

This chapter proposes a virtual-flux-based MPC (VF-MPC) scheme to remove the grid voltage sensor and enhance the grid current performance for AC-DC MC under unbalanced grid voltage conditions. By modeling the power flow in terms of the virtual flux (VF) and its 90° lagging signal, the grid current reference and grid voltage are obtained simply without the extraction of the VF positive and negative sequence components. Furthermore, the number of current vectors is increased from 9 to 39 vectors by generating 30 virtual current vectors to minimize the grid current tracking error. Especially, to reduce the computational burden due to the increased number of current vectors, a preselection method is introduced based on the location of the input current reference, which can effectively reduce the number of candidate current vectors from 39 to 8. The proposed VF-MPC scheme was compared with previous MPC schemes, and its effectiveness was verified by a simulation and experiment.

5.1   Introduction

The MPC has been applied to MCs to control various kinds of variables, such as the output current and reactive power [102], active and reactive powers [69], and grid current directly [103]. Among them, MPC with direct grid current control usually provides better performance [103]. In [104], a simplified direct current control scheme was presented to drive an AC-DC MC effectively even when the grid voltage is unbalanced. However, these MPC schemes provide relatively poor steady-state performance because only one switching state is applied during a sampling period.

To improve the steady-state performance, a modulated model predictive control (M2PC) scheme was introduced for MCs by synthesizing the current and voltage references [105], [106]. However, the computational burden of M2PC is increased significantly due to the combination cost function calculation, which is used to select an optimal combination current and voltage vectors. In case of AC-DC MC, the combination cost function of the M2PC is eliminated by considering the location of the input current reference [50]. However, the online duty cycle calculation in [50] is still an obstacle to implementing AC-DC MCs with low computational burden. To overcome this problem, MPC was combined with 12 virtual current vectors for an AC-DC MC, where the duty cycle was predefined for each switching states used to generate the virtual current vector [49]. Even though a preselection algorithm is applied to reduce the number of candidate current vectors, the computational burden is still high because the grid current prediction is needed for all candidate current vectors. Moreover, the MPC of the AC-DC MC requires voltage information on both sides of the input filter to predict the grid current.

As well known, the voltage sensor increases hardware volume and cost and may reduce control reliability due to the risk of sensor malfunction. To eliminate the grid voltage sensor, virtual flux (VF)-based voltage estimation is known as the most common and simplest method [107]. However, VF estimation based on a pure integrator results in saturation and DC-drift problems. Several advanced methods have been proposed to achieve fast and accurate VF estimation [108]–[111]. Even though the methods in [108]–[111] are well

established for balanced grid voltage, the accuracy of the grid voltage estimation and the control performance deteriorate under unbalanced grid voltage conditions.

To improve the control performance under unbalanced grid voltage conditions, the positive and negative sequence components of the VF are generally considered [112]–[114]. A balanced sinusoidal grid current is achieved by extracting the positive sequence component of the VF to estimate the instantaneous power [112]. Furthermore, both the positive and negative sequence components of the VF are detected to generate a current reference corresponding to different control objectives, such as balanced sinusoidal grid current or unbalanced sinusoidal grid current and ripple-free grid active or reactive powers [113], [114]. In spite of the flexible control capability, the computational burden is usually increased due to the extraction of positive and negative sequence components [80], [81].

To enhance the grid current performance for an AC-DC MC under unbalanced grid voltage conditions, a VF-based grid voltage sensorless MPC (VF-MPC) scheme is proposed in this chapter. The grid voltage is firstly estimated by deducing its relation with the lagging VF irrespective of the unbalanced conditions. Then, a new instantaneous power model is developed in terms of the VF and its 90° lagging signal, so the grid current reference can be generated easily without the extraction of the VF positive and negative sequence components. Furthermore, a novel set of 30 virtual current vectors are also proposed to reduce the grid current tracking error by increasing the number of current vectors from 9 to 39. And also, in order to reduce the computational burden caused by the increased virtual vector, a simple sector detection algorithm is proposed to preselect 8 from 39 current vectors as candidate optimal current vectors for the prediction process. Thus, the proposed VF-MPC can enhance the grid current performance without increasing the computational burden compared to a previous MPC scheme with virtual current vector in [49]. Simulation and experimental comparisons with different schemes in [49] and [104] are given to evaluate the effectiveness of the proposed scheme.

5.2 Conventional VF-MPC of AC-DC MC

5.2.1 Grid Voltage Estimation Based on VF
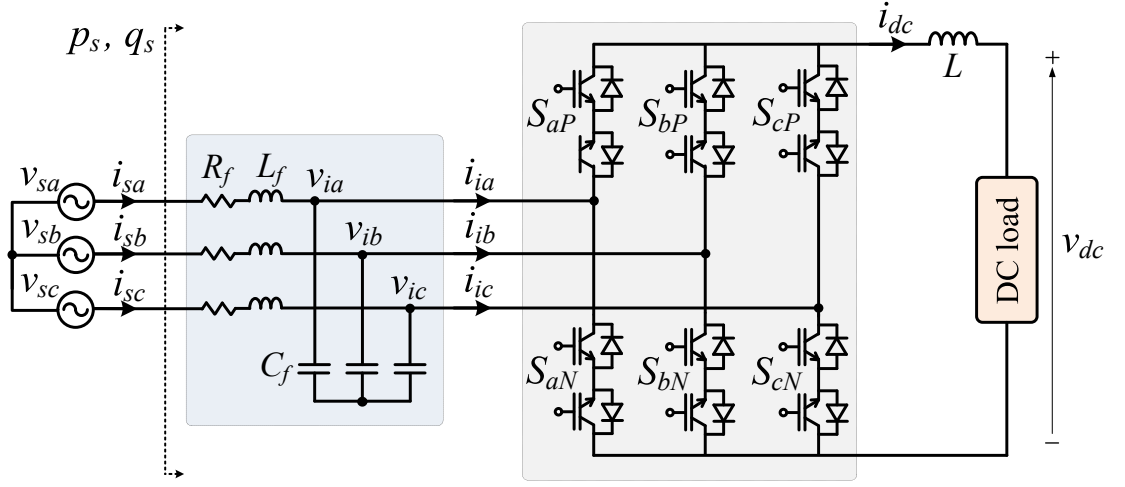
Figure 5.1 Topology of an AC-DC MC.

The considering topology of an AC-DC MC in this chapter is shown in Figure 5.1. Based on Figure 5.1, the input side of the AC-DC MC is described by the following continuous-time equations:

$$\mathbf{v_s} = R_f \mathbf{i_s} + L_f \frac{d\mathbf{i_s}}{dt} + \mathbf{v_i}, \tag{5.1}$$

$$\mathbf{i_s} = \mathbf{i_i} + C_f \frac{d\mathbf{v_i}}{dt}, \tag{5.2}$$

where $\mathbf{v_s}$, $\mathbf{i_s}$, $\mathbf{v_i}$, and $\mathbf{i_i}$ are the grid voltage, grid current, input voltage, and input current vectors, respectively, and L_f, C_f, and R_f are the input filter parameters.

To reduce the volume and cost and improve the reliability, the grid voltage measurement is replaced with VF-based grid voltage estimation. This method was originally applied for the voltage-sensorless control of voltage source converters (VSCs) [107]–[111]. Similarly to VSCs, the inductance L_f and resistance R_f of the input filter of an AC-DC MC are equivalent to the stator leakage inductance and resistance of a virtual AC motor. The VF vector is defined as follows:

$$\boldsymbol{\psi_s} = \int \mathbf{v_s} dt \tag{5.3}$$

Substituting (5.1) into (5.3), the VF is obtained as follows:

$$\boldsymbol{\psi_s} = \int (R_f \mathbf{i_s} + \mathbf{v_i}) dt + L_f \mathbf{i_s} \tag{5.4}$$

Figure 5.2 Block diagram of the conventional VF-MPC for the AC-DC MC.

From (5.4), the VF is estimated based on the measured values of $\mathbf{i_s}$ and $\mathbf{v_i}$. To avoid saturation and DC-drift problems caused by the pure integrator, a low-pass filter (LPF) was used to replace the pure integrator. However, the LPF reduces the system performance since it causes phase and magnitude errors in the estimated VF [108]. To eliminate these errors, a second-order LPF is adopted to estimate the VF [111]. The transfer function of the second-order LPF is

$$G_{LPF2}(s) = \frac{2\omega_c}{(s+\omega_c)^2} \tag{5.5}$$

where the cut-off frequency ω_c equals to the grid angular frequency. The grid voltage vector can be obtained from the estimated VF as follows:

$$\mathbf{v_s} = \frac{d\mathbf{\psi_s}}{dt} = \frac{d(\mathbf{\psi}e^{j\omega t})}{dt} = \frac{d\mathbf{\psi}}{dt}e^{j\omega t} + j\omega\mathbf{\psi_s}, \tag{5.6}$$

where $\mathbf{\psi}$ is the time phasor of the VF, and ω is the grid angular frequency. Under balanced sinusoidal grid voltage conditions, the derivative in (5.6) equals zero, and the steady-state estimation of the grid voltage vector is obtained as follows:

$$\mathbf{v_s} = j\omega\mathbf{\psi_s}. \tag{5.7}$$

5.2.2 Conventional VF-MPC

Figure 5.2 shows a block diagram of the conventional VF-MPC scheme for AC-DC MCs. The grid active power reference P_s^{ref} is determined from a PI controller that is used to regulate the output current. The grid current reference in the stationary frame (αβ frame) is generated to achieve sinusoidal grid current, constant output current, and near-unity grid power factor [104]:

$$\begin{cases} i_{s\alpha}^{ref} = \dfrac{2P_s^{ref}}{3} \dfrac{v_{s\beta}'}{(v_{s\beta}'v_{s\alpha} - v_{s\beta}v_{s\alpha}')} \\[4mm] i_{s\beta}^{ref} = -\dfrac{2P_s^{ref}}{3} \dfrac{v_{s\alpha}'}{(v_{s\beta}'v_{s\alpha} - v_{s\beta}v_{s\alpha}')} \end{cases} \tag{5.8}$$

where $v_{s\alpha}$, $v_{s\beta}$, $v'_{s\alpha}$, and $v'_{s\beta}$ are the α and β components of the grid voltage and their 90° lagging signals, respectively. Substituting (5.7) into (5.8), the grid current reference is expressed in terms of the VF:

$$\begin{cases} i_{s\alpha}^{ref} = -\dfrac{2P_s^{ref}}{3} \dfrac{\psi_{s\beta}}{\omega(\psi_{s\alpha}^2 + \psi_{s\beta}^2)} \\[4mm] i_{s\beta}^{ref} = \dfrac{2P_s^{ref}}{3} \dfrac{\psi_{s\alpha}}{\omega(\psi_{s\alpha}^2 + \psi_{s\beta}^2)} \end{cases} \tag{5.9}$$

To regulate the grid current, a cost function is developed from the error between the current reference and its predicted value:

$$g = \left| i_{s\alpha}^{ref} - i_{s\alpha}(k+1) \right| + \left| i_{s\beta}^{ref} - i_{s\beta}(k+1) \right|, \tag{5.10}$$

where $i_{s\alpha}(k+1)$ and $i_{s\beta}(k+1)$ are the α and β components of the predicted grid current. To avoid the performance deterioration caused by the delay effect in digital implementation, a two-step prediction method is used. The cost function for the tracking error at instant $(k+2)$ is evaluated instead of instant $(k+1)$:

$$g = \left| i_{s\alpha}^{ref} - i_{s\alpha}(k+2) \right| + \left| i_{s\beta}^{ref} - i_{s\beta}(k+2) \right| \tag{5.11}$$

In each sampling period, the switching state that minimizes the cost function in (5.11) is applied to drive the converter.

5.3   Proposed VF-MPC

5.3.1 VF-Based Instantaneous Power under Unbalanced Grid Voltages

Under unbalanced grid voltage conditions, the amplitude of the VF is time-varying due to the grid voltage negative sequence component. This causes inaccurate grid voltage estimation in (5.7) and severe low-order harmonics in the grid current reference in (5.9). To overcome these problems, we developed a new instantaneous power model of the AC-DC MC in terms of the VF to generate the grid current reference.

In an unbalanced grid voltage system without a zero sequence, the VF vector $\boldsymbol{\psi}_s$ and its 90° lagging signal $\boldsymbol{\psi}'_s$ are expressed as the sum of the positive and negative sequence components:

$$\boldsymbol{\psi}_s = \boldsymbol{\psi}_p e^{j\omega t} + \boldsymbol{\psi}_n e^{-j\omega t}, \tag{5.12}$$

$$\boldsymbol{\psi}'_s = \boldsymbol{\psi}_p e^{j(\omega t - \frac{\pi}{2})} + \boldsymbol{\psi}_n e^{-j(\omega t - \frac{\pi}{2})} = -j\boldsymbol{\psi}_p e^{j\omega t} + j\boldsymbol{\psi}_n e^{-j\omega t}. \tag{5.13}$$

where $\boldsymbol{\psi}_p$ and $\boldsymbol{\psi}_n$ are the time phasors of positive and negative sequence components of VF, respectively. From (5.12) and (5.13), the grid voltage vector is obtained based on the VF:

$$\begin{aligned}
\mathbf{v}_s &= \frac{d\boldsymbol{\psi}_s}{dt} = \frac{d\boldsymbol{\psi}_p}{dt} e^{j\omega t} + j\omega\boldsymbol{\psi}_p e^{j\omega t} + \frac{d\boldsymbol{\psi}_n}{dt} e^{-j\omega t} - j\omega\boldsymbol{\psi}_n e^{-j\omega t} \\
&= j\omega\boldsymbol{\psi}_p e^{j\omega t} - j\omega\boldsymbol{\psi}_n e^{-j\omega t} = -\omega\boldsymbol{\psi}'_s
\end{aligned} \tag{5.14}$$

From (5.14), we can see that the grid voltage is estimated easily based on the lagging VF irrespective of the unbalanced conditions.

The grid's instantaneous active and reactive powers are generally expressed as following under unbalanced grid voltage conditions:

$$p_s = \frac{3}{2}\text{Re}(\mathbf{v}_s \mathbf{i}_s^*) = P_0 + P_{c2}\cos(2\omega t) + P_{s2}\sin(2\omega t), \tag{5.15}$$

$$q_s = \frac{3}{2}\text{Im}(\mathbf{v}_s \mathbf{i}_s^*) = Q_0 + Q_{c2}\cos(2\omega t) + Q_{s2}\sin(2\omega t), \tag{5.16}$$

where P_o and Q_o are the average values of the active and reactive power, and P_{c2}, P_{s2}, Q_{c2}, Q_{s2} are the ripples of the active and reactive powers, respectively.

In the previous VF-based grid voltage sensorless methods [112]–[114], the computational burden generally increased because the positive and negative sequence components of the VF are used to model the active and reactive powers in (5.15) and (5.16). To avoid this drawback, the grid voltage sensorless method is implemented by deriving the active and reactive grid power components in terms of the grid current and VF in the αβ frame based on the relationship in (5.14):

$$
\begin{cases}
P_0 = \dfrac{3}{4}\omega(-\psi'_{s\alpha}i_{s\alpha} - \psi'_{s\beta}i_{s\beta} + \psi_{s\alpha}i'_{s\alpha} + \psi_{s\beta}i'_{s\beta}) \\
P_{c2} = \dfrac{3}{4}\omega(k_1\cos(2\omega t) + k_2\sin(2\omega t)) \\
P_{s2} = \dfrac{3}{4}\omega(-k_2\cos(2\omega t) + k_1\sin(2\omega t)) \\
Q_0 = \dfrac{3}{4}\omega(-\psi'_{s\beta}i_{s\alpha} + \psi'_{s\alpha}i_{s\beta} + \psi_{s\beta}i'_{s\alpha} - \psi_{s\alpha}i'_{s\beta}) \\
Q_{c2} = \dfrac{3}{4}\omega(k_3\cos(2\omega t) + k_4\sin(2\omega t)) \\
Q_{s2} = \dfrac{3}{4}\omega(-k_4\cos(2\omega t) + k_3\sin(2\omega t))
\end{cases}
\tag{5.17}
$$

where

$$
\begin{cases}
k_1 = (-\psi'_{s\alpha}i_{s\alpha} - \psi'_{s\beta}i_{s\beta} - \psi_{s\alpha}i'_{s\alpha} - \psi_{s\beta}i'_{s\beta}) \\
k_2 = (\psi_{s\alpha}i_{s\alpha} + \psi_{s\beta}i_{s\beta} - \psi'_{s\alpha}i'_{s\alpha} - \psi'_{s\beta}i'_{s\beta}) \\
k_3 = (-\psi'_{s\beta}i_{s\alpha} + \psi'_{s\alpha}i_{s\beta} - \psi_{s\beta}i'_{s\alpha} + \psi_{s\alpha}i'_{s\beta}) \\
k_4 = (\psi_{s\beta}i_{s\alpha} - \psi_{s\alpha}i_{s\beta} - \psi'_{s\beta}i'_{s\alpha} + \psi'_{s\alpha}i'_{s\beta}),
\end{cases}
\tag{5.18}
$$

where $i_{s\alpha}, i_{s\beta}, \psi_{s\alpha}, \psi_{s\beta}, i'_{s\alpha}, i'_{s\beta}, \psi'_{s\alpha}$, and $\psi'_{s\beta}$ are the α and β components of the grid current and VF and their 90° lagging signals, respectively.

5.3.2 Current Reference Generation

The grid current reference is generated according to the control objective such as active or reactive power ripple elimination by considering the power model in (5.17). In this study, the average grid reactive power is set to zero to achieve a grid power factor near unity. For this purpose, the average grid active power P_0 is set equal to the grid active power reference

$P_s{}^{ref}$, while the active power ripples P_{c2} and P_{s2} should be zero to remove the ripple on DC side. Thus, we can obtain the following equations:

$$\begin{cases} P_0 = P_s^{ref} \\ Q_0 = 0 \\ P_{c2} = 0 \\ P_{s2} = 0 \end{cases}. \tag{5.19}$$

From (5.19), the grid current reference in the αβ frame is obtained as follows:

$$\begin{cases} i_{s\alpha}^{ref} = \dfrac{2P_s^{ref}}{3} \dfrac{\psi_{s\beta}}{\omega(\psi_{s\beta}'\psi_{s\alpha} - \psi_{s\beta}\psi_{s\alpha}')} \\ i_{s\beta}^{ref} = -\dfrac{2P_s^{ref}}{3} \dfrac{\psi_{s\alpha}}{\omega(\psi_{s\beta}'\psi_{s\alpha} - \psi_{s\beta}\psi_{s\alpha}')} \end{cases}. \tag{5.20}$$

5.4   Proposed Virtual Current Vectors

5.4.1 Proposed Virtual Current Vectors

The number of real current vectors is limited to 9 for an AC-DC MC, which results in poor steady-state performance of the MPC scheme. To solve this problem, the number of the current vectors is increased by generating virtual current vectors for the MPC scheme. The virtual vector technique was originally presented to improve the performance of VSCs [115]–[118]. A set of 12 virtual vectors was firstly applied for the MPC of an AC-DC MC in [49]. Generally, the tracking error can be reduced by enlarging the control set of the MPC scheme. However, a large number of virtual vectors may lead to heavy computational burden and commutation failure due to the narrow pulse [49]. In the proposed method, the computational burden is reduced by using a simple preselection algorithm compared to the MPC scheme in [49] even though 30 virtual current vectors are used to improve the grid current performance of an AC-DC MC.

Each virtual current vector $I^{virtual}$ is synthesized by two or three real current vectors in one sampling period for a prefixed time interval t_j:

Table 5.1 Virtual current vectors (VCVs) formations

VCV	Formation	VCV	Formation	VCV	Formation
I_7	$\frac{1}{3}I_1 + \frac{2}{3}I_{0a}$	I_{17}	$\frac{2}{3}I_3 + \frac{1}{3}I_{0b}$	I_{27}	$\frac{2}{3}I_2 + \frac{1}{3}I_3$
I_8	$\frac{1}{3}I_2 + \frac{2}{3}I_{0a}$	I_{18}	$\frac{1}{3}I_3 + \frac{1}{3}I_4 + \frac{1}{3}I_{0b}$	I_{28}	$\frac{1}{3}I_2 + \frac{2}{3}I_3$
I_9	$\frac{1}{3}I_3 + \frac{2}{3}I_{0b}$	I_{19}	$\frac{2}{3}I_4 + \frac{1}{3}I_{0b}$	I_{29}	$\frac{2}{3}I_3 + \frac{1}{3}I_4$
I_{10}	$\frac{1}{3}I_4 + \frac{2}{3}I_{0b}$	I_{20}	$\frac{1}{3}I_4 + \frac{1}{3}I_5 + \frac{1}{3}I_{0c}$	I_{30}	$\frac{1}{3}I_3 + \frac{2}{3}I_4$
I_{11}	$\frac{1}{3}I_5 + \frac{2}{3}I_{0c}$	I_{21}	$\frac{2}{3}I_5 + \frac{1}{3}I_{0c}$	I_{31}	$\frac{2}{3}I_4 + \frac{1}{3}I_5$
I_{12}	$\frac{1}{3}I_6 + \frac{2}{3}I_{0c}$	I_{22}	$\frac{1}{3}I_5 + \frac{1}{3}I_6 + \frac{1}{3}I_{0c}$	I_{32}	$\frac{1}{3}I_4 + \frac{2}{3}I_5$
I_{13}	$\frac{2}{3}I_1 + \frac{1}{3}I_{0a}$	I_{23}	$\frac{2}{3}I_6 + \frac{1}{3}I_{0c}$	I_{33}	$\frac{2}{3}I_5 + \frac{1}{3}I_6$
I_{14}	$\frac{1}{3}I_1 + \frac{1}{3}I_2 + \frac{1}{3}I_{0a}$	I_{24}	$\frac{1}{3}I_6 + \frac{1}{3}I_1 + \frac{1}{3}I_{0a}$	I_{34}	$\frac{1}{3}I_5 + \frac{2}{3}I_6$
I_{15}	$\frac{2}{3}I_2 + \frac{1}{3}I_{0a}$	I_{25}	$\frac{2}{3}I_1 + \frac{1}{3}I_2$	I_{35}	$\frac{2}{3}I_6 + \frac{1}{3}I_1$
I_{16}	$\frac{1}{3}I_2 + \frac{1}{3}I_3 + \frac{1}{3}I_{0b}$	I_{26}	$\frac{1}{3}I_1 + \frac{2}{3}I_2$	I_{36}	$\frac{1}{3}I_6 + \frac{2}{3}I_1$

$$I^{virtual} = \sum_{j=1}^{n} \frac{t_j}{T_s} I_j^{real}, \ (n=2 \text{ or } n=3) \tag{5.21}$$

$$\sum_{j=1}^{n} t_j = T_s \tag{5.22}$$

$$I_j^{real} \in \{I_0, I_1, ..., I_6\} \tag{5.23}$$

Table 5.1 shows the formation of the 30 virtual current vectors, and Figure 5.3 shows the space vector diagram of the real and virtual current vectors used in the proposed VF-MPC. Taking the virtual vector I_7 as an example, two real vectors I_1 and I_{0a} are used to synthesize it with the corresponding time intervals $t_1 = T_s/3$ and $t_2 = 2T_s/3$, respectively.

5.4.2 Preselection of Candidate Current Vector

In spite of the enhanced performance, the large number of virtual current vectors significantly increases the computational burden due to the large number of calculations for grid current prediction and cost function evaluation. To reduce the computational burden without affecting the control performance, the grid current prediction for all candidate current vectors is replaced with the computation of only one input current reference vector
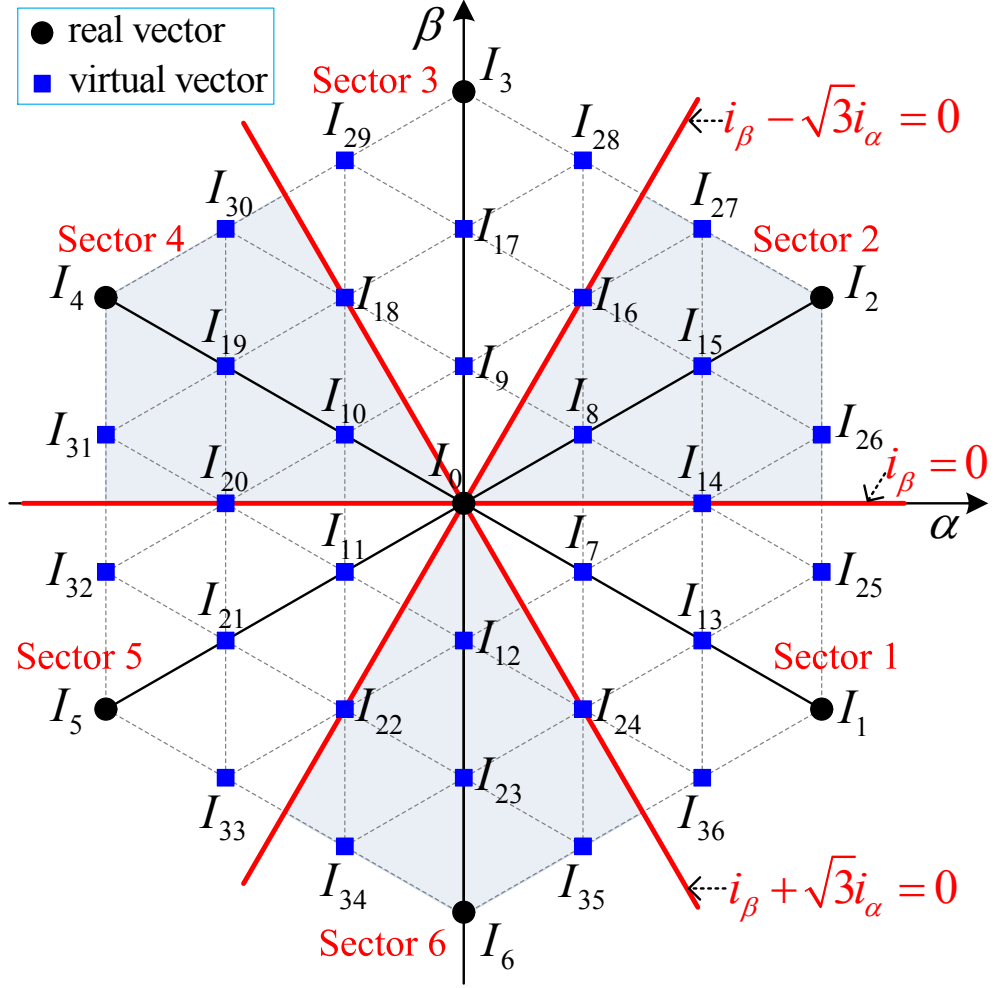
Figure 5.3 The proposed space current vector diagram for the AC-DC MC.

$\mathbf{i_i}^{ref}$. In (5.11), the cost function is used to select one input current vector $\mathbf{i_i}(k+1)$ from the candidate current vectors, which makes the predicted grid current $\mathbf{i_s}(k+2)$ closest to its reference $\mathbf{i_s}^{ref}$. Therefore, the input current reference vector $\mathbf{i_i}^{ref}$ that makes $\mathbf{i_s}(k+2)$ close to its reference $\mathbf{i_s}^{ref}$ is determined as follows:

$$\mathbf{i_i}^{ref} = \frac{\mathbf{i_s}^{ref} - \mathbf{\Phi}_{21}\mathbf{v_i}(k+1) - \mathbf{\Phi}_{22}\mathbf{i_s}(k+1) - \mathbf{\Gamma}_{21}\mathbf{v_s}(k)}{\mathbf{\Gamma}_{22}}, \tag{5.24}$$

where the grid current reference $\mathbf{i_s}^{ref}$ is calculated from (5.20), and the grid voltage $\mathbf{v_s}(k)$ is estimated in (5.14).

However, the system performance with the RICV in (5.24) may deteriorate because of the limited damping coefficient of the input LC filter. To solve this problem, active damping is widely applied to mitigate the LC resonance by emulating the virtual damping resistor R_d

Table 5.2 Current sectors determination

Constraints		Sector
$i_{i\beta}^{ref} \geq 0$	$i_{i\beta}^{ref} - \sqrt{3}i_{i\alpha}^{ref} < 0$	2
	$\begin{cases} i_{i\beta}^{ref} - \sqrt{3}i_{i\alpha}^{ref} \geq 0 \\ i_{i\beta}^{ref} + \sqrt{3}i_{i\alpha}^{ref} \geq 0 \end{cases}$	3
	$i_{i\beta}^{ref} + \sqrt{3}i_{i\alpha}^{ref} < 0$	4
$i_{i\beta}^{ref} < 0$	$i_{i\beta}^{ref} - \sqrt{3}i_{i\alpha}^{ref} \geq 0$	5
	$\begin{cases} i_{i\beta}^{ref} - \sqrt{3}i_{i\alpha}^{ref} < 0 \\ i_{i\beta}^{ref} + \sqrt{3}i_{i\alpha}^{ref} < 0 \end{cases}$	6
	$i_{i\beta}^{ref} + \sqrt{3}i_{i\alpha}^{ref} \geq 0$	1

in parallel with a filter capacitor. The RICV is modified to involve the active damping function in the MPC scheme, as explained in section 4.4.2:

$$\mathbf{i_i}^{ref} = \frac{(1 + jC_5)\mathbf{i_s}^{ref} + C_1\mathbf{v_i}(k+1) + C_2\mathbf{i_s}(k+1) + C_3\mathbf{v_s}(k)}{C_4}, \tag{5.25}$$

where $C_5 = \omega L_f / R_d$, $C_1 = (\Phi_{11}/R_d - \Phi_{21})$, $C_2 = (\Phi_{12}/R_d - \Phi_{22})$, $C_3 = ((\Gamma_{11} - 1)/R_d - \Gamma_{21})$, and $C_4 = (\Gamma_{22} - \Gamma_{12}/R_d)$ are constant values. To select the current vector that is closest to the RICV, the cost function is modified as follows:

$$g = \left| i_{i\alpha}^{ref} - i_{i\alpha}(k+1) \right| + \left| i_{i\beta}^{ref} - i_{i\beta}(k+1) \right|, \tag{5.26}$$

where $i_{i\alpha}^{ref}$ and $i_{i\beta}^{ref}$ are the α and β components of the RICV in (5.25), and $i_{i\alpha}(k+1)$ and $i_{i\beta}(k+1)$ are the α and β components of the candidate current vector.

If all 39 input current vectors are considered as candidates, the 39 times cost function calculation still results in high computing time for the evaluation process. To reduce the number of cost function calculations, the possible candidate current vectors are preselected based on the located sector of the $\mathbf{i_i}^{ref}$. As shown in Figure 5.3, the space vector current diagram of the AC/DC MC is divided into 6 sectors, and the $\mathbf{i_i}^{ref}$ sector is generally determined based on its phase angle. Conventionally, the phase angle is calculated by an arctangent function [116]–[118]:
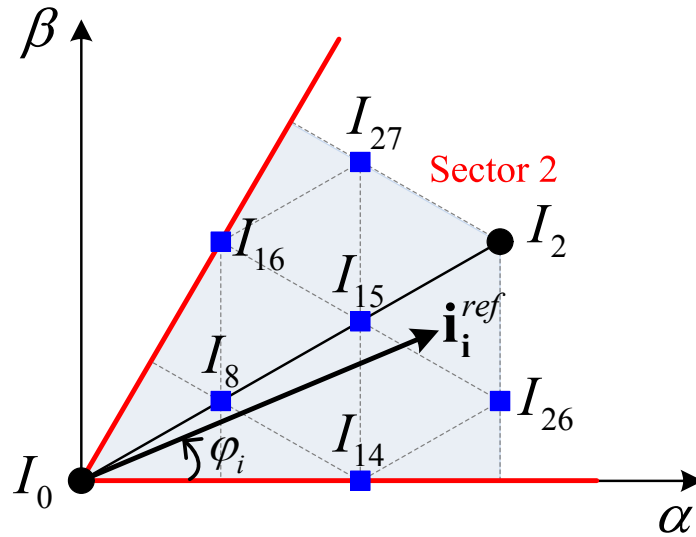
Figure 5.4 Candidate current vectors when the current reference $\mathbf{i_i}^{ref}$ is located in sector 2.

Table 5.3 Preselection of Candidate Current Vectors

Sectors	Candidate current vectors
1	I_{0a}, I_1, I_7, I_{24}, I_{13}, I_{14}, I_{36}, I_{25}
2	I_{0a}, I_2, I_8, I_{14}, I_{15}, I_{16}, I_{26}, I_{27}
3	I_{0b}, I_3, I_9, I_{16}, I_{17}, I_{18}, I_{28}, I_{29}
4	I_{0b}, I_4, I_{10}, I_{18}, I_{19}, I_{20}, I_{30}, I_{31}
5	I_{0c}, I_5, I_{11}, I_{20}, I_{21}, I_{22}, I_{32}, I_{33}
6	I_{0c}, I_6, I_{12}, I_{22}, I_{23}, I_{24}, I_{34}, I_{35}

$$\varphi_i = \tan^{-1} \frac{i_{i\beta}^{ref}}{i_{i\alpha}^{ref}} \tag{5.27}$$

However, the trigonometric calculation in (5.27) is complex and time-consuming in the practical implementation. To overcome this problem, the space vector current diagram is divided into 6 sectors as shown in Figure 5.3 by three straight lines with their corresponding equations of the lines. As shown in Table 5.2, the sector of the current reference $\mathbf{i_i}^{ref}$ is easily determined from Figure 5.3 without trigonometric calculation.
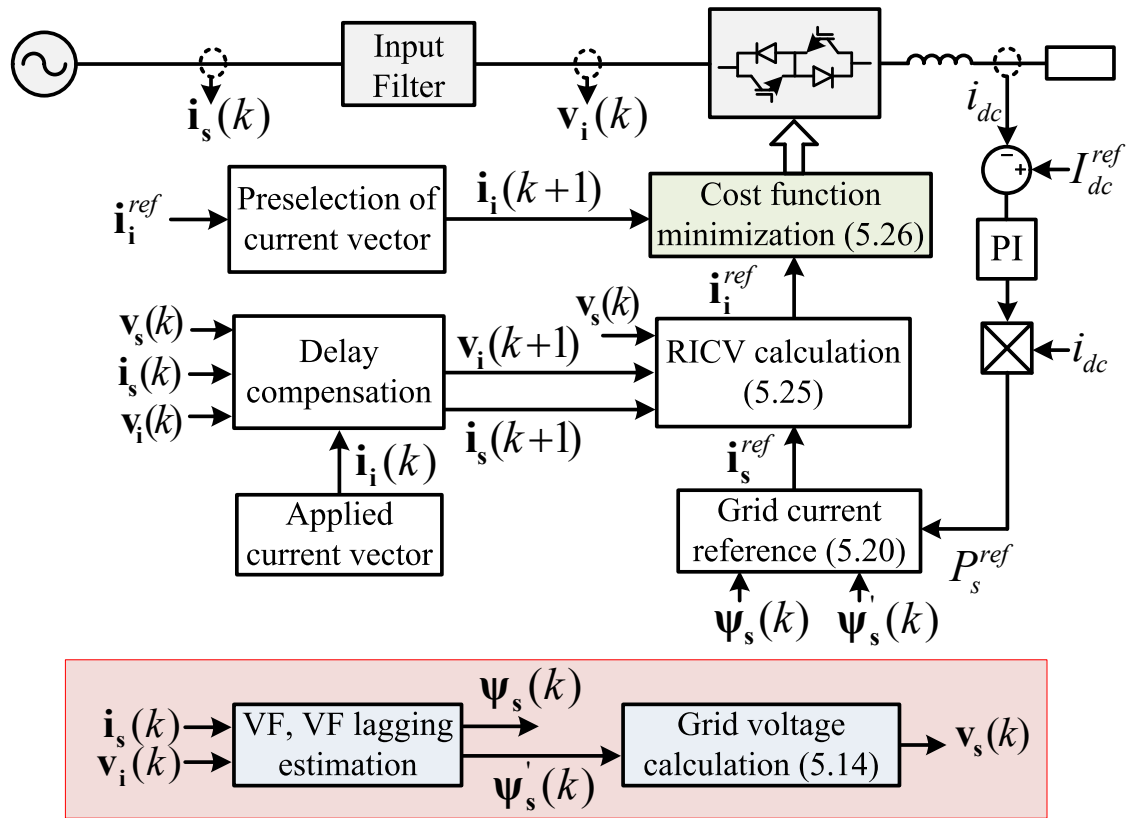
Figure 5.5 Block diagram of the proposed VF-MPC with virtual current vectors for the AC-DC MC.

The candidate current vectors for the prediction process are selected according to the located sector of the current reference $\mathbf{i_i}^{ref}$. For example, if the $\mathbf{i_i}^{ref}$ is located in sector 2, 8 of the 39 current vectors (I_{0a}, I_2, I_8, I_{14}, I_{15}, I_{16}, I_{26}, and I_{27}) are selected as possible candidate current vectors to be evaluated by the cost function in (5.26), as shown in Figure 5.4. Similarly, all possible candidate current vectors are shown in Table 5.3 when the current reference $\mathbf{i_i}^{ref}$ is located in different sectors. When the candidate current vectors are preselected, the number of cost function calculations is reduced from 39 to 8, which reduces the computing time significantly.

Figure 5.5 shows a block diagram of the proposed VF-MPC with virtual current vectors for the AC-DC MC. During each sampling period, the current vector that minimizes the cost function in (5.26) is applied to drive the converter.

Table 5.4 Simulation and Experimental Parameters

System Parameters	Values	
	Simulation	Experiment
Power supply	$\mathbf{V_p} = 220 \text{ V}\angle 0^0$, $f_i = 60$ Hz	$\mathbf{V_p} = 70 \text{ V}\angle 0^0$, $f_i = 60$ Hz
Rated power	1.5 kW	500 W
Input filter	$L_f = 1.2$ mH, $C_f = 20$ μF, $R_f = 0 \ \Omega$, $R_d = 20 \ \Omega$	$L_f = 1.2$ mH, $C_f = 20$ μF, $R_f \approx 0 \ \Omega$, $R_d = 20 \ \Omega$
Output	$L = 10$ mH, $R = 15 \ \Omega$, $V_{DC} = 150$ V	$L = 10$ mH, $R = 10 \ \Omega$
Sampling period	$T_s = 50$ μs	$T_s = 50$ μs

5.5   Simulation Results

Simulations were carried out using PSIM 9.0 software to evaluate the performance of the proposed VF-MPC scheme. A 10% degree of unbalance was applied by injecting a positive sequence voltage $\mathbf{V_p}$=220V$\angle 0^o$ and a negative sequence voltage $\mathbf{V_n}$=22V$\angle 0^o$. $\mathbf{V_n}$ is zero when the grid voltage is balanced. The other parameters are listed in Table 5.4.

Figure 5.6 shows a performance comparison in the rectifier mode for the conventional VF-MPC (VF-MPC1) and the proposed VF-MPC (VF-MPC2) when the balanced grid voltage becomes unbalanced at t = 0.05 s. The output current reference is 8 A. When the grid voltage is balanced, the grid voltage is well estimated by both VF-MPC schemes. As shown in the first halves of Figures 5.6(a) and (b), both VF-MPC schemes achieve a constant output current and a balanced sinusoidal grid current with THD of 3.69% and 3.87%, respectively. The grid current is kept in phase with the grid voltage, which means a unity grid power factor is achieved.

However, when the grid voltage becomes unbalanced, the estimated grid voltage becomes inaccurate because the negative component of the VF is not considered by the VF-MPC1. Therefore, VF-MPC1 shows large output current ripple and severe grid current distortion with THD of 10.62%. Both grid active and reactive powers include power ripples.
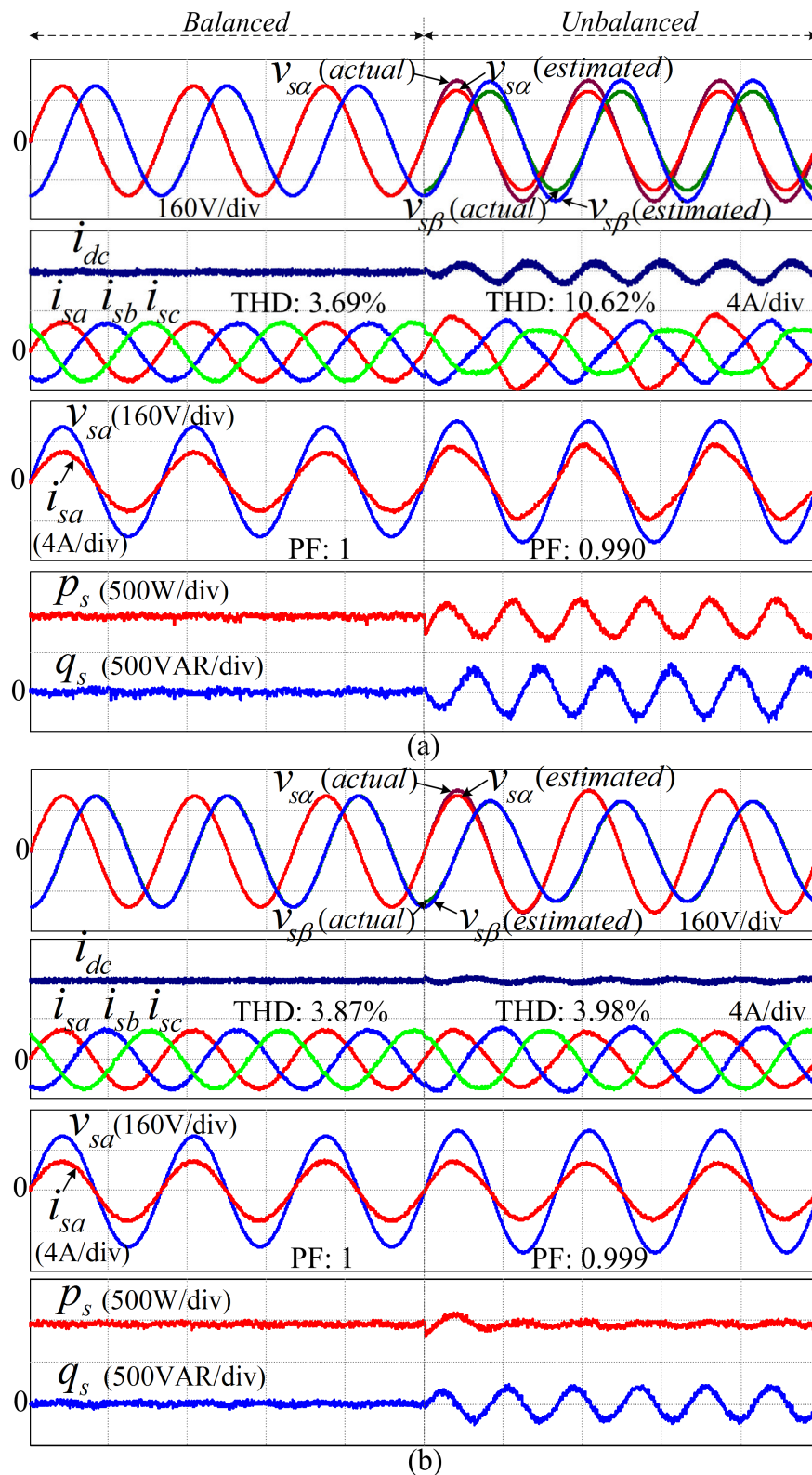
Figure 5.6 Simulation results of actual and estimated grid voltage in αβ frame, grid and output currents, phase-a grid voltage and current, and grid active and reactive powers for rectifier mode (time: 10 ms/div): (a) Conventional VF-MPC (VF-MPC1), (b) Proposed VF-MPC (VF-MPC2).
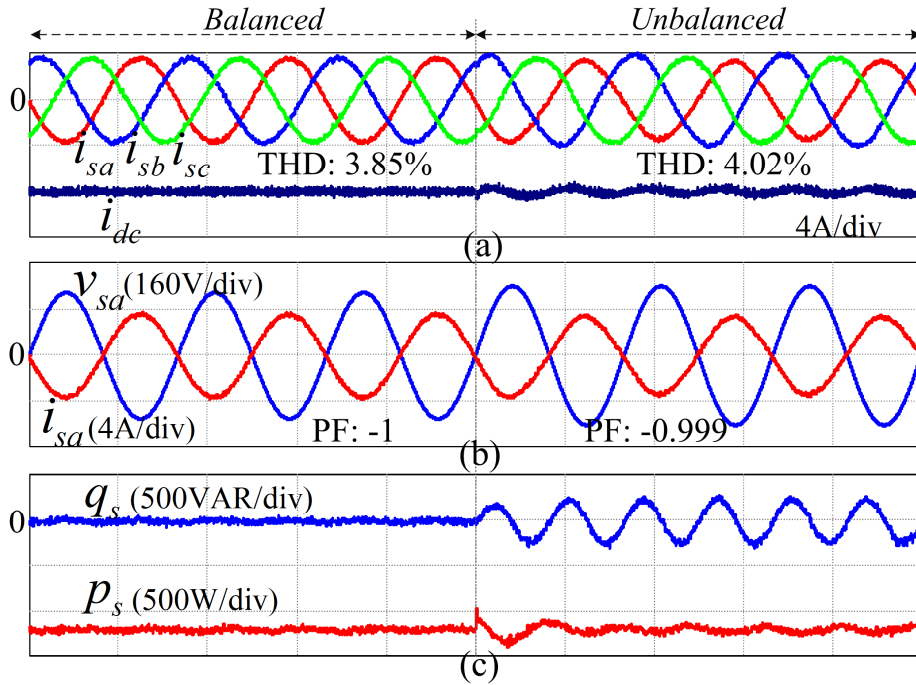
Figure 5.7 Simulation results of the performance of the VF-MPC2 for inverter mode (time: 10 ms/div): (a) Grid and output currents, (b) Phase-a grid voltage and current, (c) Grid active and reactive powers.

Even though the average reactive power is controlled to zero, the grid power factor is reduced to 0.990 due to the distorted grid current, as shown in the second half of Figure 5.6(a). In contrast, the grid voltage is estimated accurately by the VF-MPC2 regardless of unbalanced conditions. As shown in the second half of Figure 5.6(b), VF-MPC2 provides a constant output current and a sinusoidal grid current with THD of 3.98%. The grid active power ripple is eliminated, and the average reactive power is kept at zero, which results in a near unity grid power factor. From Figure 5.6, the VF-MPC2 shows good performance under both balanced and unbalanced grid voltage conditions.

To verify performance of the VF-MPC2 in the inverter mode of the AC-DC MC, a battery with voltage rating $V_{DC} = 150$ V is used as an active load in the DC side. Figure 5.7 shows the performance of the VF-MPC2 for the inverter mode when the balanced grid voltage becomes unbalanced at t = 0.05 s. The output current reference is -8 A. As shown in Figure 5.7(a), the proposed MPC method shows sinusoidal grid current with the THDs of 3.85% and 4.02% under the balanced and unbalanced grid voltage conditions, respectively. We can see that the output current is well controlled at reference values even under
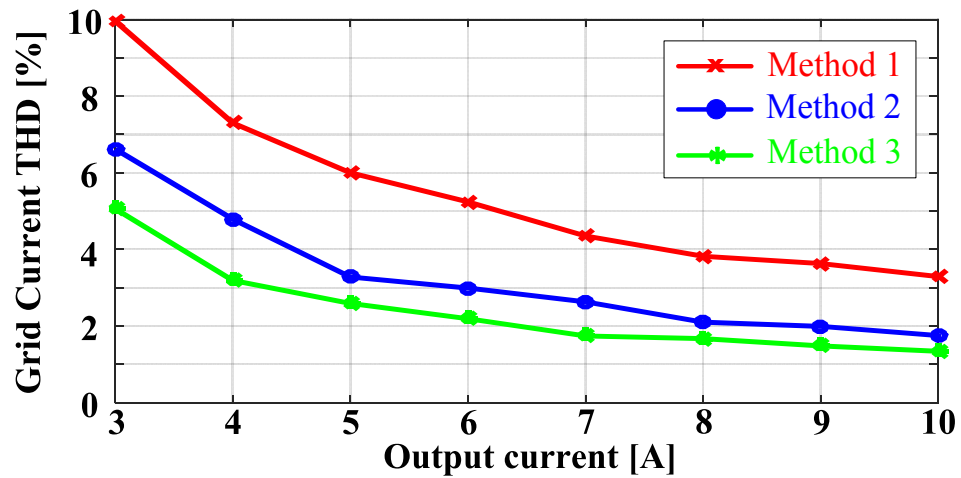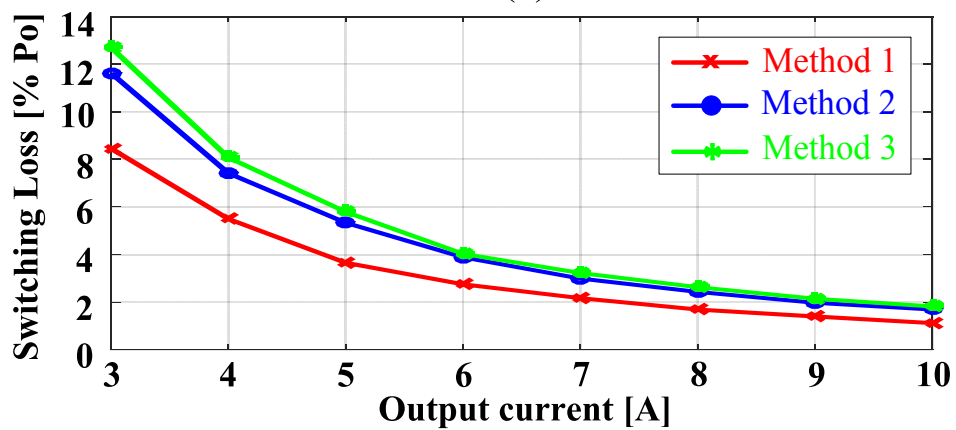
Figure 5.8 Comparisons with different methods: (a) Grid current THDs, (b) Switching losses.

unbalanced grid voltage condition. In Figure 5.7(b), the phase angle difference between the grid voltage and current becomes 180°, and a near unity power factor is achieved by keeping zero average grid reactive power as shown in Figure 5.7(c). In Figure 5.7(c), the negative grid active power means the grid active power is supplied from the battery. From Figure 5.7, it is clear that the proposed MPC method works well in inverter mode regardless of the grid voltage conditions.

To verify the effectiveness of the proposed virtual current vector method along with VF-MPC2, grid current THDs and switching losses were investigated with three different methods in rectifier mode: (a) VF-MPC2 with only real current vector [12] (Method 1), (b) VF-MPC2 with additional 12 virtual current vectors [16] (Method 2), and VF-MPC2 with the proposed 30 virtual current vectors (Method 3), as shown in Figure 5.8. The grid current
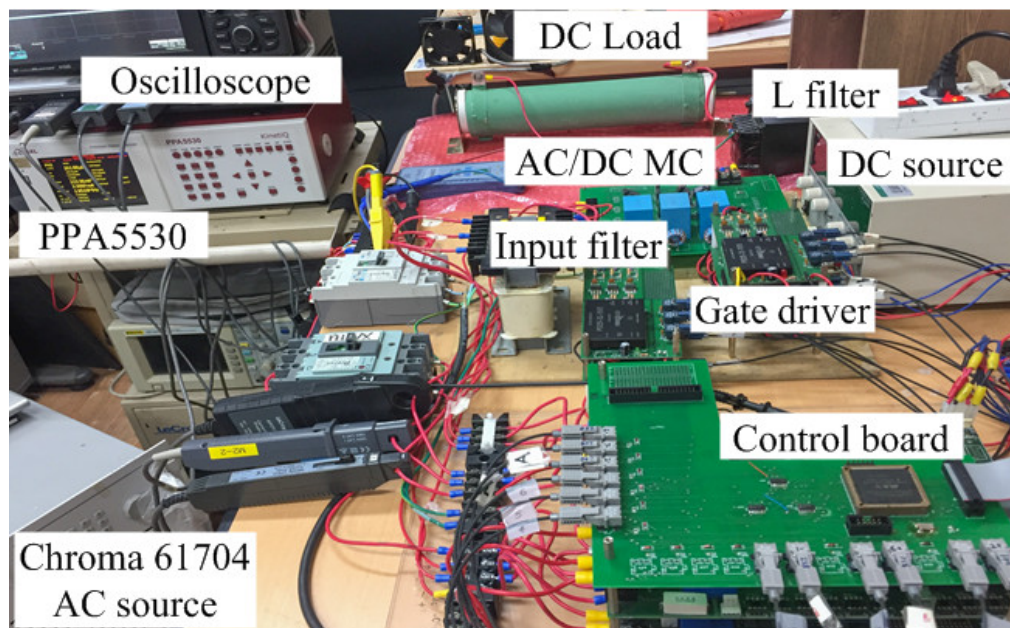
Figure 5.9 Experimental set-up for AC/DC MC.

THDs are highest with Method 1 since the number of current vectors is limited to 9. Compared to Method 1, the grid current THDs are reduced with Method 2 by applying 12 virtual current vectors. Furthermore, thanks to the increased number of current vectors to 39, the grid current THDs with Method 3 are reduced significantly compared to Method 1 and Method 2, as shown in Figure 5.8(a). Figure 5.8(b) shows that the switching losses with Method 3 increase slightly, even though the number of current vectors is much higher than in Method 2. Therefore, the proposed virtual current vector method is definitely effective when high grid current quality is expected.

5.6   Experimental Results

The prototype AC/DC MC in Figure 5.9 was implemented to verify the effectiveness of the proposed VF-MPC scheme. The control system was designed with a DSP TMS320F28335, and a CPLD Altera EPM7128SLC84-15. The bidirectional power switches were realized by two discrete IGBTs IRG4PF50WD, and the unbalanced grid voltage is provided by Chroma 61704 programmable AC power source with positive and negative
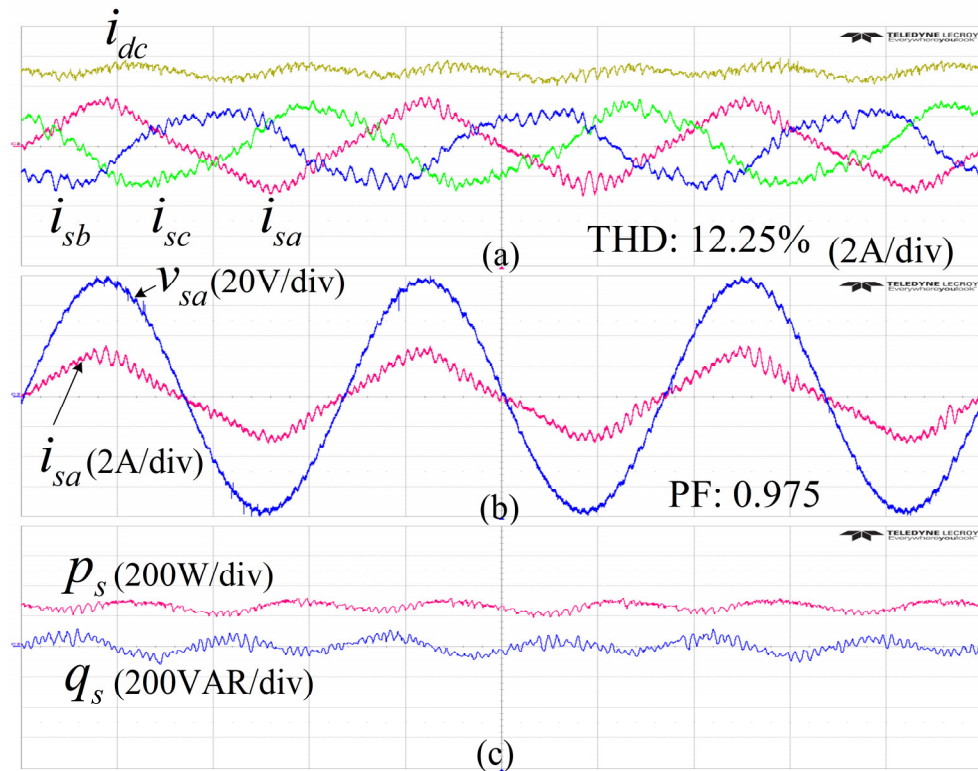
Figure 5.10 Experiment results for VF-MPC1 (time: 5 ms/div): (a) grid and output currents, (b) phase-*a* grid current and grid voltage, (c) grid active and reactive powers.

voltage sequences of $\mathbf{V_p}$=70V $\angle\,0^0$ and $\mathbf{V_n}$=7V $\angle\,0^0$, respectively, which result in a 10% degree of imbalance. A PPA5530 Precision Power Analyzer was used to measure the THDs of the grid current and the grid power factor. The parameters in the experiment are listed in Table 5.4, and all experimental results are obtained for rectifier mode under unbalanced grid voltage conditions.

Figure 5.10 shows the experimental performance of the VF-MPC1 scheme with an output current reference of 5 A. Due to the inaccuracy of grid voltage estimation under unbalanced conditions, the output current shows large ripple, and the grid current becomes severely distorted with THD of 12.25%, as shown in Figure 5.10(a). In Figure 5.10(b), even though the average grid reactive power is controlled to zero by the VF-MPC1 scheme, the power factor is reduced to 0.975 because of the distorted grid current. Both grid active and reactive powers include ripples as shown in Figure 5.10(c).

The experimental performance of the VF-MPC2 scheme is shown in Figure 5.11. By deducing the grid current reference and grid voltage from the VF and its 90° lagging signal,
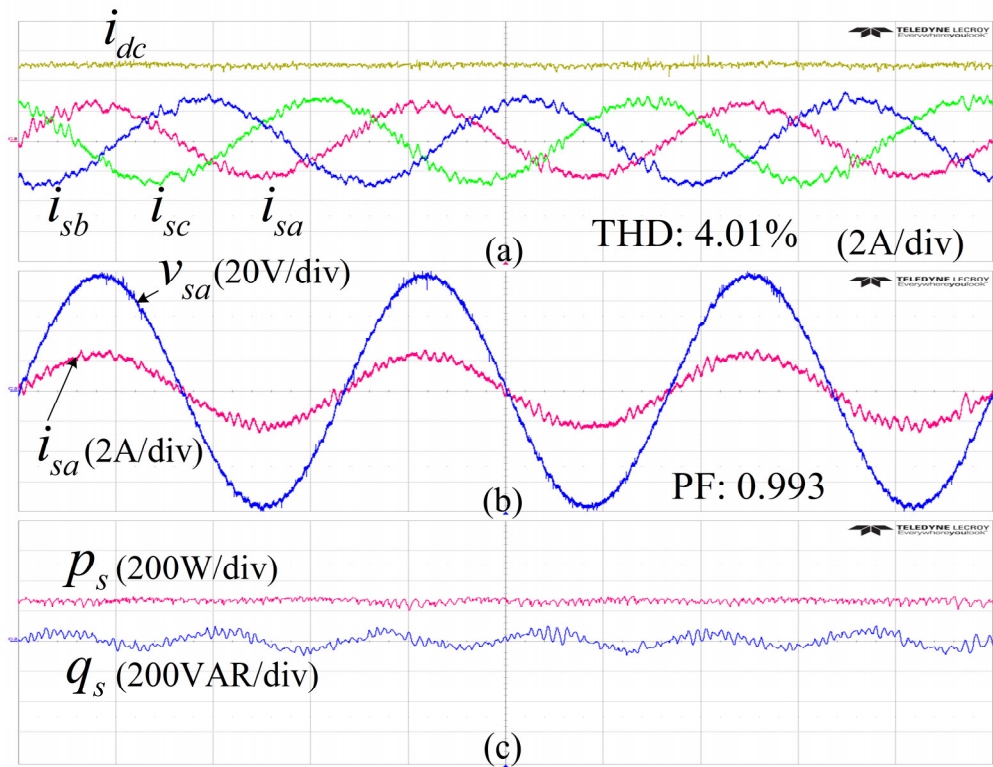
Figure 5.11 Experiment results for VF-MPC2 with only 9 real current vectors (Method 1) (time: 5 ms/div): (a) grid and output currents, (b) phase-*a* grid current and grid voltage, (c) grid active and reactive powers.

the VF-MPC2 scheme provides a constant output current and a sinusoidal grid current with THD of 4.01%, as shown in Figure 5.11(a). In Figure 5.11(c), the active power ripple is eliminated, and the average reactive power is kept at zero, which results in a high power factor of 0.993 as shown in Figure 5.11(b). From Figure 5.11, it is clear that VF-MPC2 works well under unbalanced grid voltage conditions.

In spite of sinusoidal grid current waveform, the grid THD is still high because only 9 real current vectors are used in the VF-MPC2 scheme (Method 1) in Figure 5.11(a). To demonstrate the effectiveness of the virtual current vector in terms of grid current improvement, Figures 5.12 and 5.13 show the experimental performance of the VF-MPC2 scheme with 12 virtual current vectors (Method 2) and the proposed 30 virtual current vectors (Method 3). As shown in Figures 5.12(c) and 5.13(c), the active power ripple is significantly eliminated, and the average reactive power is kept at zero by both methods.

i_{dc}

i_{sb} i_{sc} i_{sa} (a) THD: 2.67% (2A/div)

v_{sa}(20V/div)

i_{sa}(2A/div) (b) PF: 0.996

p_s(200W/div)

q_s(200VAR/div)

(c)
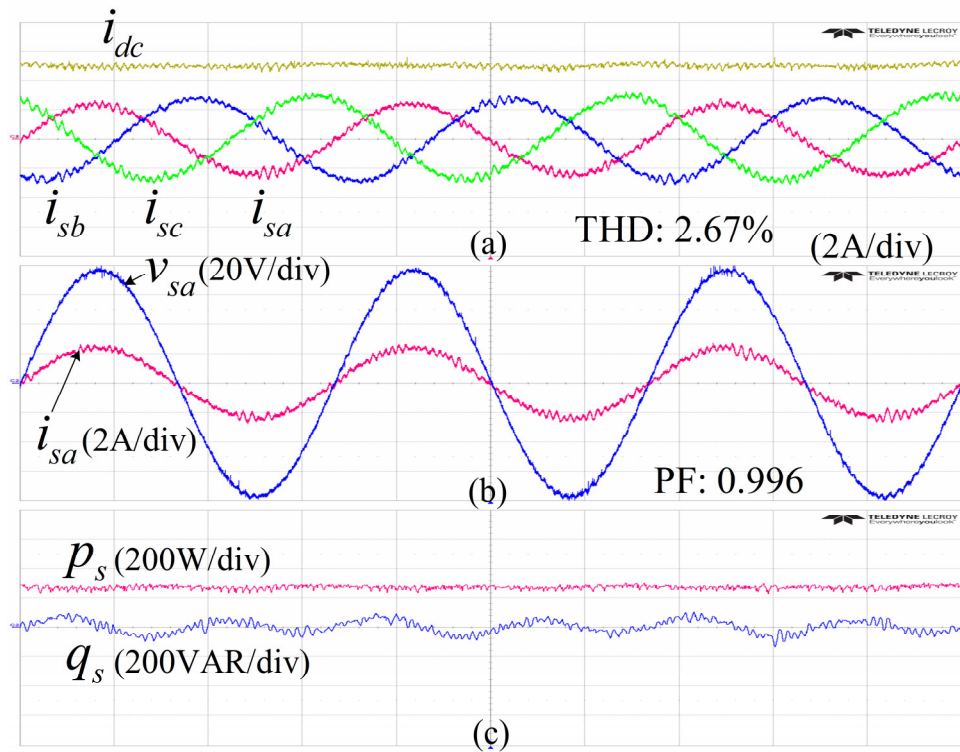
Figure 5.12 Experiment results for Method 2 (time: 5 ms/div): (a) grid and output currents, (b) phase-*a* grid current and grid voltage, (c) grid active and reactive powers

i_{dc}

i_{sb} i_{sc} i_{sa} (a) THD: 1.98% (2A/div)

v_{sa}(20V/div)

i_{sa}(2A/div) (b) PF: 0.998

p_s(200W/div)

q_s(200VAR/div)

(c)
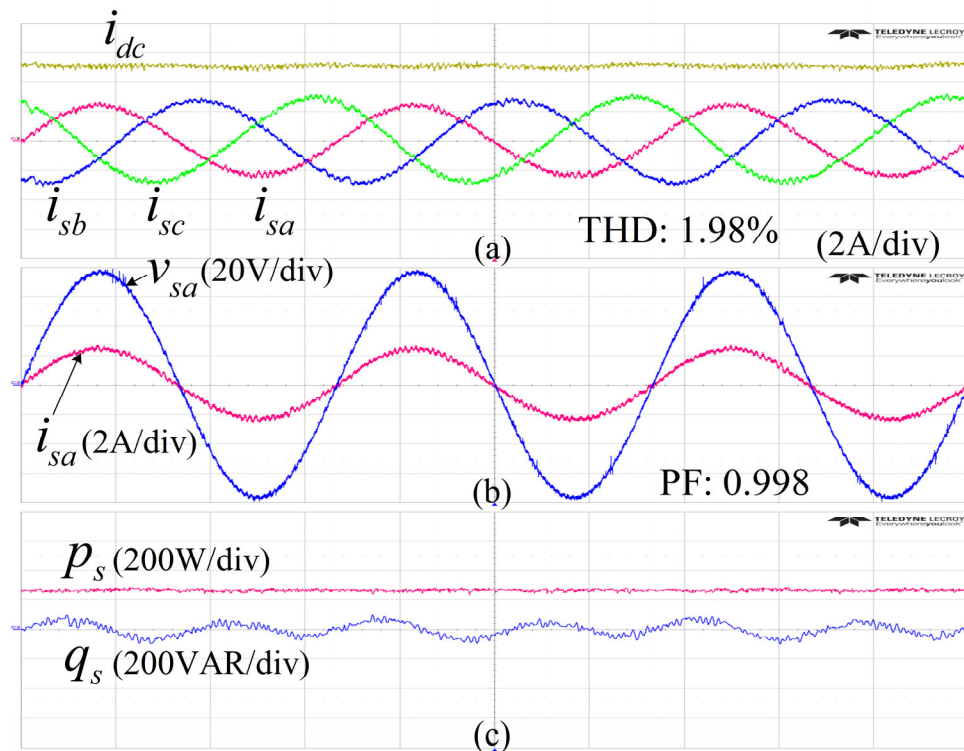
Figure 5.13 Experiment results for Method 3 (time: 5 ms/div): (a) grid and output currents, (b) phase-*a* grid current sand grid voltage, (c) grid active and reactive powers.
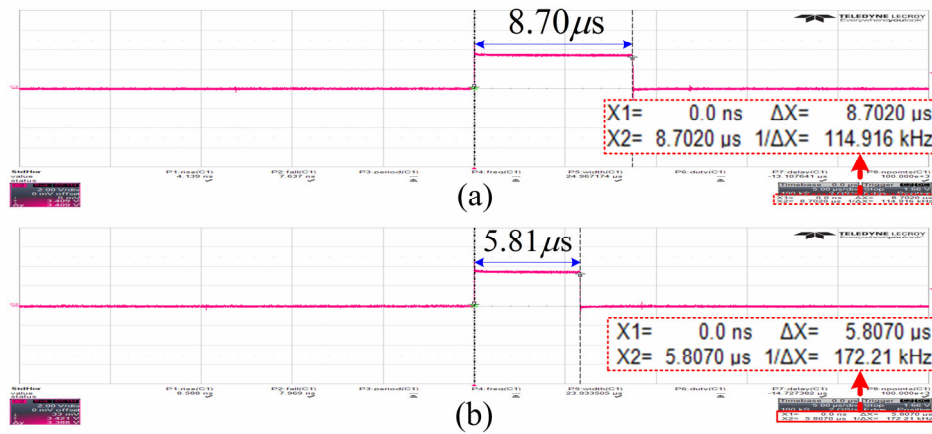
Figure 5.14 Prediction time comparison (time: 5 μs/div): (a) Method 2, (b) Method 3.
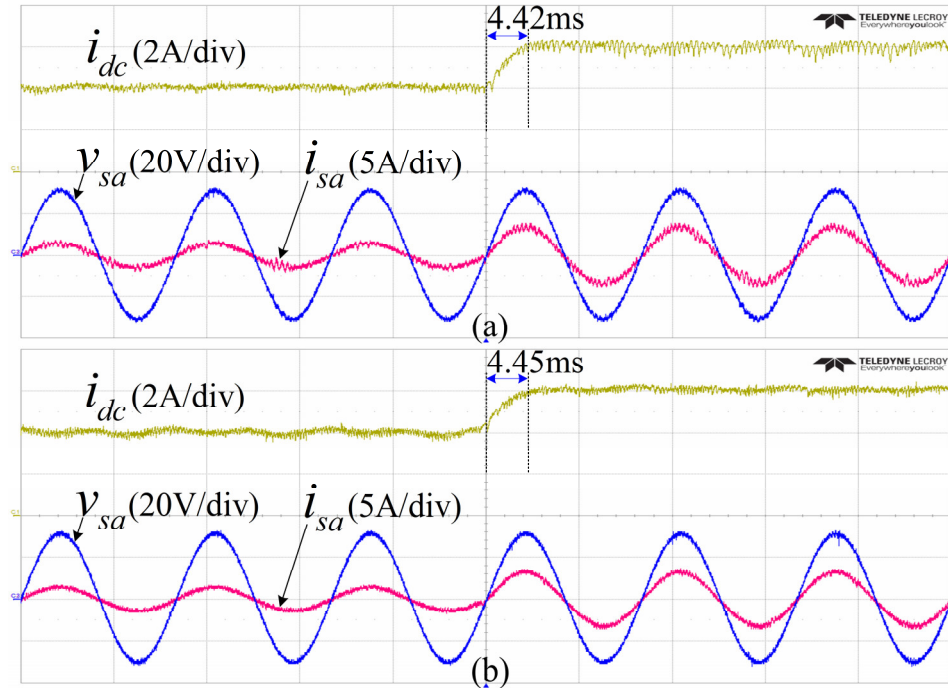
Figure 5.15 Experimental results of output current, phase-a grid voltage and current with a step change of output current reference from 4 A to 6 A (time: 10 ms/div): (a) Method 1, (b) Method 3.

Figure 5.12(a) shows that the grid current is improved by Method 2 with a THD of 2.67% compared to the THD of 4.01% with Method 1. As a result, the grid power factor in Method 2 is increased to 0.996, as shown in Figure 5.12(b).

Furthermore, compared with Figure 5.12, the performance of the system is improved much more by Method 3. The THD of the grid current is reduced to 1.98%, and the power

Table 5.5 Experimental comparison for different MPC schemes

	VF-MPC1	VF-MPC2		
		Method 1	Method 2	Method 3
Grid current THD (%)	12.25	4.01	2.67	1.98
Power factor	0.975	0.993	0.996	0.998
Prediction time (µs)	-	5.87	8.70	5.81
Dynamic response (ms)	-	4.42	4.45	4.45

factor is kept at almost unity (0.998), as shown in Figure 5.13. Even though the number of virtual current vectors is much higher with Method 3, the prediction time is reduced compared to Method 2 thanks to the proposed preselection method to select the candidate current vectors, as shown in Figure 5.14.

The dynamic performance is compared for Method 1 and Method 3 in Figure 5.15 when the output current reference suddenly changes from 4 A to 6 A. The output and grid current responses with Method 3 are fast, almost similar to those of Method 1. This means the generation of virtual current vector does not affect the dynamic performance of the MPC scheme. Furthermore, the grid current is kept almost in phase with the grid voltage with both methods, so a near-unity grid power factor is achieved even in the transient process.

Table 5.5 summaries the experimental comparison for different MPC schemes. From the experimental results, it is clear that the proposed VF-MPC scheme improves the grid current quality without grid voltage sensor in spite of unbalanced grid voltage condition.

5.7   Summary

This chapter has proposed a grid voltage sensorless MPC scheme by means of the VF concept for an AC-DC MC under unbalanced grid voltage conditions. The grid current reference and grid voltage are obtained by the VF and its 90° lagging signal, so the computation burden is reduced by avoiding extraction of the VF positive and negative sequence components. Moreover, the grid current performance is improved by generating

several virtual current vectors to reduce the grid current tracking errors. The number of current vector candidates was reduced significantly from 39 to 8 by considering the location of the input current reference. Therefore, the computation time is not increased even though the number of virtual current vectors is increased compared to previous method [49]. The simulation and experimental results verified the superior performance of the proposed VF-MPC scheme with virtual current vectors, and the number of voltage sensors is reduced by haft compared to the conventional voltage based MPC methods in [49] and [104].

Chapter 6

Model Predictive Control Scheme with Input Filter Power Ripple Consideration

The power ripple in the input filter is normally ignored in the conventional MPC scheme of an AC-DC MC under unbalanced grid voltage conditions. Unfortunately, this power ripple causes output power and current ripples. Some methods compensate this power ripple to obtain ripple-free output current. However, these methods are generally complicated due to the increased computational and control burden or the use of a digital filter to estimate the power ripple. Moreover, the compensation of power ripple results in current distortion on the grid side, which has yet to be fully addressed. This chapter presents an improved MPC scheme to simultaneously compensate input filter power ripple and reduce grid current distortion under unbalanced grid voltage conditions. The power ripple is calculated based on the grid voltage and its 90° lagging signal, which makes the implementation simple without grid voltage components extraction or digital filter design. Furthermore, a closed-loop current controller is proposed to reduce the harmonic distortion of the grid current. The feasibility of the proposed MPC scheme is confirmed by both simulation and experimental results.

6.1 Introduction

A number of modified MPC schemes have been presented to drive MCs normally through unbalanced grid voltage conditions [93]–[95], [104]. In [93] and [94], a balanced sinusoidal grid currents is provided. However, this causes output current ripple for AC-DC MCs due to the power balance principle. Furthermore, depending on the control targets, the converter can provide balanced or unbalanced grid current as well as grid active or reactive power ripple elimination [95]. However, grid voltage positive and negative sequence components (P-NSCs) are usually detected to generate the grid current reference, which increases the control complexity. To overcome this problem, a simplified MPC scheme without grid voltage P-NSCs extraction is presented in [104]. Unfortunately, it is hard to guarantee ripple-free output current with these methods [93]–[95], [104] since the power ripple in the input filter is not considered.

To improve output current performance, the power ripple in an input filter was recently considered together with grid power [119]–[123]. The ripple on the DC side was eliminated by adding the power ripple from an input filter to the grid power reference for a PWM rectifier [119]–[121]. However, power ripple compensating methods [119]–[121] are not applicable to MCs since MCs generally use a second-order LC input filter. In [122], the P-NSCs of the grid voltage and current are detected to model the power ripple in an LC input filter. In addition, a proportional resonant (PR) controller is applied to control the grid current. Although a ripple-free output current was achieved in [122], it requires large computational and control efforts. To reduce these drawbacks, a model predictive current control (MPCC) scheme was adopted for the input filter of an MC [123]. In [123], the power ripple was estimated using a digital notch filter. Then, it was added to the grid power reference. However, the power ripple resulted in grid current distortion. To date, this shortcoming has not been remedied.

In this chapter, an improved MPC scheme is proposed to reduce both the grid current distortion and the output current ripple of an AC-DC MC. The power compensation is simply calculated by using the grid voltage and its 90° lagging signal. Thus, the proposed
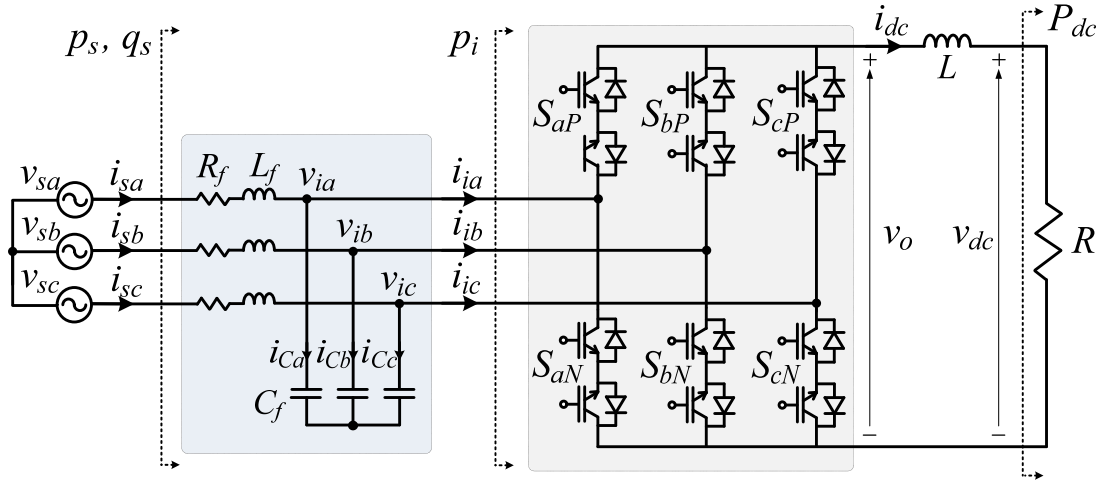
Figure 6.1 Power circuit of AC-DC MC system.

MPC scheme is implemented easily without grid voltage P-NSCs detection or digital filter design. Furthermore, a closed-loop current controller is proposed to suppress the grid current harmonic caused by power ripple under unbalanced grid voltage conditions. The controller generates a grid current reference for the MPC scheme that can effectively suppress grid current harmonics. Simulation and experimental tests are done to confirm the feasibility of the proposed MPC scheme.

6.2   Existing MPC Scheme with Ripple-Free Active Power

A power circuit of an AC-DC MC is shown in Figure 6.1, where the AC-DC MC is connected to a three-phase power supply through an input LC filter, and a resistive load R is connected in the DC side through an L filter. With the relevant symbols shown in Figure 6.1, the relationships among the input currents i_{ia}, i_{ib}, and i_{ic}; the input voltages v_{ia}, v_{ib}, and v_{ic}; the output current i_{dc}; and the output voltage v_o are:

$$\begin{bmatrix} i_{ia} \\ i_{ib} \\ i_{ic} \end{bmatrix} = \begin{bmatrix} S_{aP} - S_{aN} \\ S_{bP} - S_{bN} \\ S_{cP} - S_{cN} \end{bmatrix} i_{dc}, \tag{6.1}$$

$$v_o = \begin{bmatrix} S_{aP} - S_{aN} \\ S_{bP} - S_{bN} \\ S_{cP} - S_{cN} \end{bmatrix}^T \begin{bmatrix} v_{ia} \\ v_{ib} \\ v_{ic} \end{bmatrix}, \tag{6.2}$$

where S_{xy} ($x \in \{a,b,c\}$ and $y \in \{P,N\}$) are the switching functions for each of the bidirectional switches. The switching function $S_{xy} = 1$ when the switch is on, and $S_{xy} = 0$ when the switch is off.

The predictive model in Section 4.2.1 is utilized to obtain the predictive value of the grid current at the *(k+1)* instant:

$$\mathbf{i}_s(k+1) = \Phi_{21}\mathbf{u_i}(k) + \Phi_{22}\mathbf{i_s}(k) + \Gamma_{21}\mathbf{u_s}(k) + \Gamma_{22}\mathbf{i_i}(k). \tag{6.3}$$

The dynamic model of the output side is:

$$v_o = L\frac{di_{dc}}{dt} + Ri_{dc} \tag{6.4}$$

Using the forward Euler approximation of (6.4) with the sampling period T_s, the output current is predicted as follows:

$$i_{dc}(k+1) = \left(1 - \frac{T_s R}{L}\right)i_{dc}(k) + \frac{T_s}{L}v_o(k) \tag{6.5}$$

where $v_o(k)$ is calculated from (6.2).

A grid current reference can be generated to satisfy various control targets under unbalanced grid conditions such as balancing the grid current [93], [94], active or reactive powers ripple elimination [95], [119]–[121], or flexible control of active and reactive power ripple [97], [124]. However, the normal control target for an AC-DC MC is removing the current ripple on the DC side while maintaining a sinusoidal grid current and a near-unity grid power factor [52], [104].

In the existing MPC scheme of AC-DC MC in [104], the input active power p_i is considered to be the same as the grid active power p_s. Thus, to remove the ripple on the DC side, ripple-free active power P_i^{ref} should be provided by the grid. The grid current reference is generated to obtain a sinusoidal grid current, ripple-free active power, and near-unity grid power factor as follows:

$$\begin{cases} i_{s\alpha}^{ref} = \dfrac{2P_i^{ref}}{3} \dfrac{v_{s\beta}^{'}}{(v_{s\beta}^{'}v_{s\alpha} - v_{s\beta}v_{s\alpha}^{'})} \\[4mm] i_{s\beta}^{ref} = -\dfrac{2P_i^{ref}}{3} \dfrac{v_{s\alpha}^{'}}{(v_{s\beta}^{'}v_{s\alpha} - v_{s\beta}v_{s\alpha}^{'})} \end{cases} \tag{6.6}$$

where $v_{s\alpha}$, $v_{s\beta}$, $v_{s\alpha}^{'}$, and $v_{s\beta}^{'}$ are the grid voltage and their 90° lagging signals in the αβ frame.

The unbalanced grid voltage vector can be expressed as the sum of P-NSCs:

$$\mathbf{v_s} = \mathbf{V_p} e^{j\omega_i t} + \mathbf{V_n} e^{-j\omega_i t}, \tag{6.7}$$

where ω_i is the grid angular frequency, and $\mathbf{V_p}$ and $\mathbf{V_n}$ are the time phasors of the P-NSCs of grid voltage. Then, the 90° lagging signal of the grid voltage vector is calculated as:

$$\mathbf{v_s^{'}} = \mathbf{V_p} e^{j(\omega_i t - \frac{\pi}{2})} + \mathbf{V_n} e^{-j(\omega_i t - \frac{\pi}{2})} = -j\mathbf{V_p} e^{j\omega_i t} + j\mathbf{V_n} e^{-j\omega_i t} \tag{6.8}$$

From (6.7) and (6.8), the grid voltage and its 90 electrical degrees delay signal are expressed in the αβ frame as:

$$\begin{cases} v_{s\alpha} = \mathbf{V_p} \cos \omega_i t + \mathbf{V_n} \cos \omega_i t \\ v_{s\beta} = \mathbf{V_p} \sin \omega_i t - \mathbf{V_n} \sin \omega_i t \\ v_{s\alpha}^{'} = \mathbf{V_p} \sin \omega_i t + \mathbf{V_n} \sin \omega_i t \\ v_{s\beta}^{'} = -\mathbf{V_p} \cos \omega_i t + \mathbf{V_n} \cos \omega_i t \end{cases} \tag{6.9}$$

By using (6.9), the denominator of (6.6) is calculated as:

$$(v_{s\beta}^{'}v_{s\alpha} - v_{s\beta}v_{s\alpha}^{'}) = |\mathbf{V_n}|^2 - |\mathbf{V_p}|^2 \tag{6.10}$$

It is observed from (6.10) that the denominator of (6.6) is time-invariant. Thus, the current reference (6.6) is sinusoidal with a ripple-free active power reference P_i^{ref}. The input active power reference P_i^{ref} is determined by the output power reference P_{dc}^{ref} and the efficiency of the converter η:

$$P_i^{ref} = P_{dc}^{ref}/\eta \tag{6.11}$$

where P_{dc}^{ref} is calculated using the output current reference i_{dc}^{ref}:

$$P_{dc}^{ref} = i_{dc}^{ref\,2} R \tag{6.12}$$

The output power reference in (6.12) is calculated for a resistive load R and should be modified if an active load such as a DC source or battery is connected on the output side [21], [49]. In practical applications, the efficiency η has little effect on the system performance, even though it is unknown and time-variant [49].
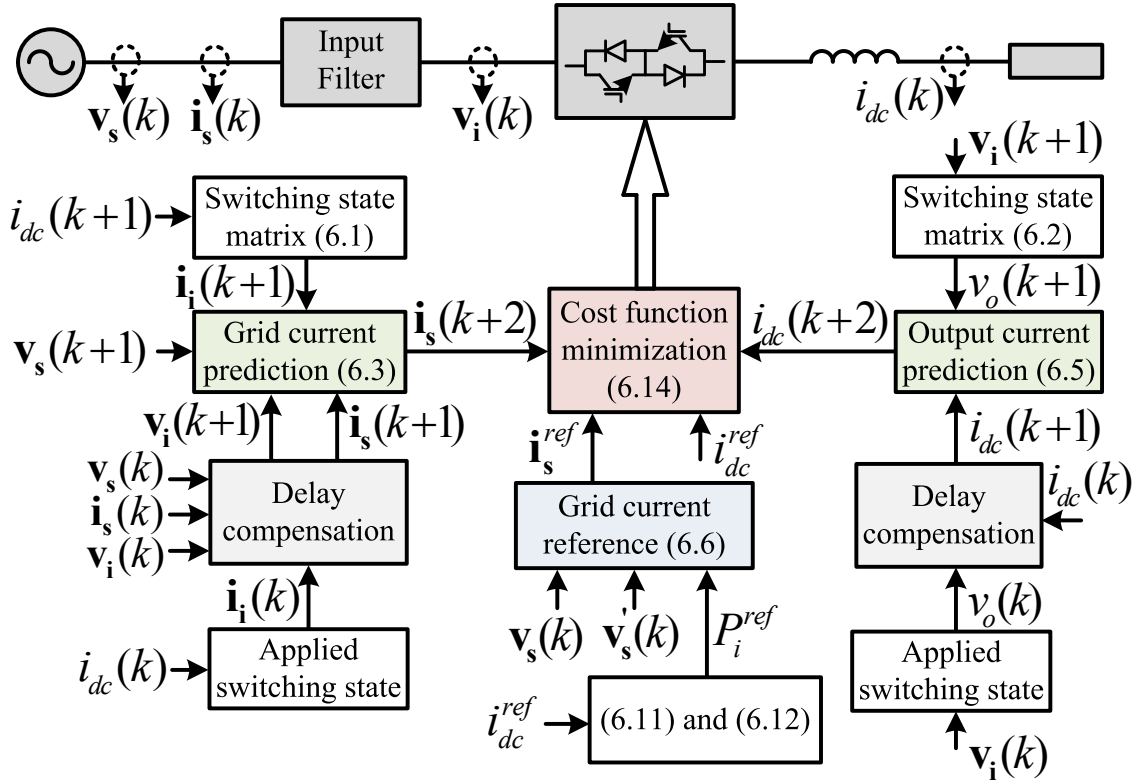
Figure 6.2 Control diagram of an MPC scheme with ripple-free active power.

To simultaneously regulate the grid and output currents, a cost function is defined to find the best switching state for the converter:

$$g = \left(\left| i_{s\alpha}^{ref} - i_{s\alpha}(k+1) \right| + \left| i_{s\beta}^{ref} - i_{s\beta}(k+1) \right| \right) + \lambda \left(i_{dc}^{ref} - i_{dc}(k+1) \right), \qquad (6.13)$$

where λ is a weighting factor that is adjusted to handle the priority of these current variables. Considering the delay effect in digital implementation, the cost function is calculated at the $(k+2)$ instant to avoid performance deterioration [96]:

$$g = \left(\left| i_{s\alpha}^{ref} - i_{s\alpha}(k+2) \right| + \left| i_{s\beta}^{ref} - i_{s\beta}(k+2) \right| \right) + \lambda \left(i_{dc}^{ref} - i_{dc}(k+2) \right). \qquad (6.14)$$

Figure 6.2 illustrates a control diagram of the existing MPC with ripple-free active power in [104] under unbalanced grid conditions. At each sample period, all of the valid switching states are used to calculated g in (6.14), and the best switching state that minimizes g is selected to drive the AC-DC MC.

6.3   Improved MPC Scheme

6.3.1 Input Filter Power Ripple Compensation

In the existing MPC scheme, the active power relationship is expressed as follows:

$$p_s = p_i = P_{dc}/\eta \tag{6.15}$$

However, due to the instantaneous power in the input filter, the active power relationship should be corrected as follows:

$$p_s - p_L - p_C = p_i = P_{dc}/\eta \tag{6.16}$$

where p_L and p_C are the active powers in the inductor and capacitor of the input filter, respectively. The active powers in the input filter inductor and capacitor are expressed in terms current and voltage variables in the αβ stationary frame as:

$$p_L = \frac{3}{2}\left(v_{L\alpha}i_{s\alpha} + v_{L\beta}i_{s\beta}\right) \tag{6.17}$$

$$p_C = \frac{3}{2}\left(v_{i\alpha}i_{C\alpha} + v_{i\beta}i_{C\beta}\right) \tag{6.18}$$

where $v_{L\alpha}$ and $v_{L\beta}$ are the voltage drops on the input filter inductor, while $i_{C\alpha}$ and $i_{C\beta}$ are the current flows into the input filter capacitor.

In practical applications, the voltage drop on the input filter inductor is usually small enough to be ignored. Thus, the input voltage $\mathbf{v_i}$ can be considered to be equal to the grid voltage $\mathbf{v_s}$, and the filter inductor power p_L can be ignored in comparison with the filter capacitor power p_C. Then, the filter capacitor current is determined as follows:

$$\mathbf{i_C} = C_f \frac{d\mathbf{v_i}}{dt} \approx C_f \frac{d\mathbf{v_s}}{dt} \tag{6.19}$$

From (6.7) and (6.8), the derivative of the grid voltage is calculated using its 90° lagging signal as follows:

$$\frac{d\mathbf{v_s}}{dt} = -\omega\mathbf{v_s'} \tag{6.20}$$

Substituting (6.19) and (6.20) into (6.18), the active power in the input filter capacitor is simply obtained as follows:

$$p_C = -\frac{3}{2}\omega C_f \left(v_{s\alpha} v_{s\alpha}^{'} + v_{s\beta} v_{s\beta}^{'} \right) \tag{6.21}$$

From (6.21), the power compensation is calculated using the grid voltage and its 90° lagging signal, which are inherently detected for grid current reference generation. Therefore, when compared to the methods in [122] and [123], the proposed calculation method (6.21) is simply implemented without extraction grid voltage sequence components or digital notch filter design.

By substituting (6.9) into (6.21), the power p_C is expressed as follows:

$$p_C = -3\omega C_f \mathbf{V_p} \mathbf{V_n} \sin 2\omega t \tag{6.22}$$

It is observed from (6.22) that the active power in the capacitor of the input filter oscillates at double the grid frequency when the grid voltage is unbalanced ($\mathbf{V_n} \neq \mathbf{0}$). This power ripple causes a double-frequency ripple on the output current, even though ripple-free grid active power is provided. From (6.16), the grid active power reference should be modified to achieve ripple-free output power and ripple-free output current:

$$P_0 = P_i^{ref} + p_L + p_C \approx P_i^{ref} + p_C \tag{6.23}$$

The grid current reference is recalculated using (6.6) for the MPC scheme with power compensation (MPC-PC) to achieve ripple-free output current:

$$\begin{cases} i_{s\alpha}^{ref} = \dfrac{2(P_i^{ref} + p_C)}{3} \dfrac{v_{s\beta}^{'}}{(v_{s\beta}^{'} v_{s\alpha} - v_{s\beta} v_{s\alpha}^{'})} \\[4mm] i_{s\beta}^{ref} = -\dfrac{2(P_i^{ref} + p_C)}{3} \dfrac{v_{s\alpha}^{'}}{(v_{s\beta}^{'} v_{s\alpha} - v_{s\beta} v_{s\alpha}^{'})} \end{cases}. \tag{6.24}$$

6.3.2 Grid Current Harmonics Suppression

The grid active power reference oscillates as in (6.23). Thus, current harmonics are inevitably included in the grid current reference in (6.24). However, this effect has not been considered. To demonstrate a quantitative analysis of grid current harmonics, the grid current reference is rewritten by substituting (6.9) and (6.22) into (6.24):
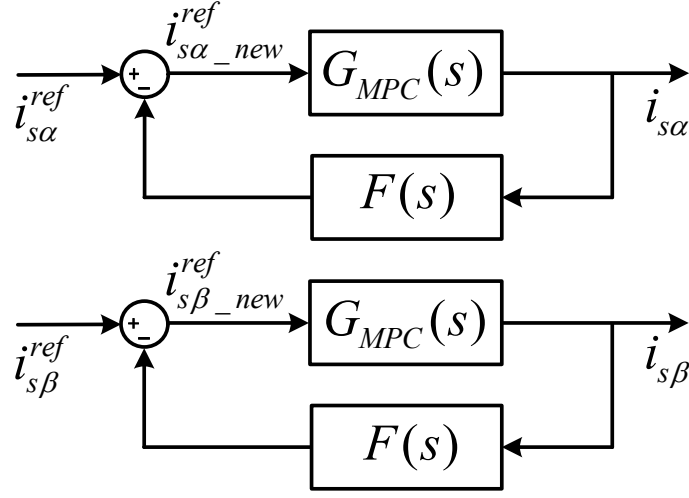
Figure 6.3 Proposed feedback controller to suppress the grid current harmonic.

$$\begin{cases} i_{s\alpha}^{ref} = \dfrac{2\left(-\mathbf{V_p}+\mathbf{V_n}\right)}{3\left(\left|\mathbf{V_n}\right|^2-\left|\mathbf{V_p}\right|^2\right)}\left((P_i^{ref}\cos\omega t - \dfrac{3}{2}\omega C_f \mathbf{V_p}\mathbf{V_n}(\sin 3\omega t + \sin\omega t)\right) \\[4mm] i_{s\beta}^{ref} = -\dfrac{2\left(\mathbf{V_p}+\mathbf{V_n}\right)}{3\left(\left|\mathbf{V_n}\right|^2-\left|\mathbf{V_p}\right|^2\right)}\left((P_i^{ref}\sin\omega t + \dfrac{3}{2}\omega C_f \mathbf{V_p}\mathbf{V_n}(\cos 3\omega t - \cos\omega t)\right) \end{cases}. \tag{6.25}$$

It is observed from (6.25) that the third-order current harmonic appears on the grid current reference. If the grid current harmonic is left uncontrolled, the grid current THD increases and may not comply with IEEE Std 519 – 2014, which states that grid current THD should be lower than 5% for grid code compliance [83]. To suppress grid current harmonics, a resonant controller is introduced into the feedback path of the grid current, as shown in Figure 6.3.

The closed-loop feedback controller generates a new grid current reference ($i_{s\alpha\_new}^{ref}$ and $i_{s\beta\_new}^{ref}$), which is used for the improved MPC (I-MPC) scheme of the AC-DC MC. The resonant controller $F(s)$ is designed to suppress the third-order current harmonic as follows:

$$F(s) = \frac{Ks}{s^2 + (3\omega_i)^2} \tag{6.26}$$

where K is the resonant gain that adjusts the gain of the controller at the selected resonant frequency $3\omega_i$.
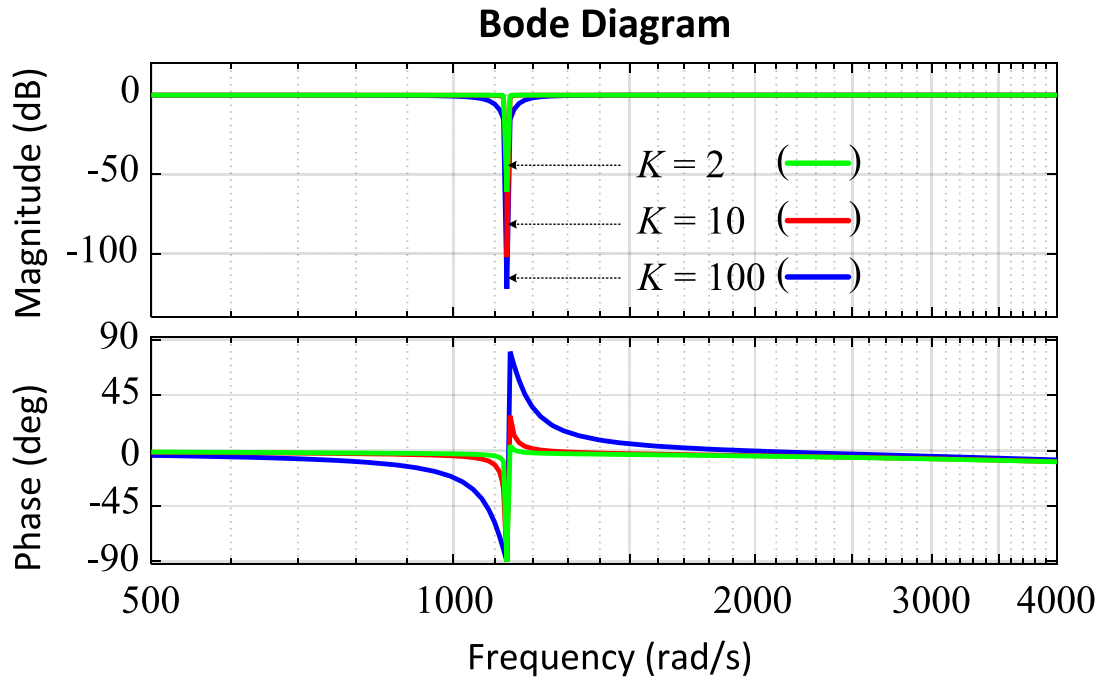
Bode Diagram

Figure 6.4 Bode diagram of the closed-loop transfer function *G(s)*.

The closed-loop transfer function of the grid current feedback controller is obtained as follows:

$$G(s) = \frac{G_{MPC}(s)}{1 + G_{MPC}(s)F(s)} \tag{6.27}$$

where $G_{MPC}(s)$ is the transfer function from the reference current to the actual grid current. The actual grid current is controlled to track its reference by a cost function. Thus, the transfer function $G_{MPC}(s)$ only represents the time delay effect generated by the MPC scheme:

$$G_{MPC}(s) = e^{-sT_s} \tag{6.28}$$

Figure 6.4 shows a Bode diagram of the closed-loop transfer function *G(s)* in (6.27) with different values of *K*. The resonant peak at the selected frequency $3\omega_i$ is reduced with an increase in *K*, which means a grid current reference with a lower third-order harmonic current is generated. However, the third-order harmonic current also contributes to compensating the power ripple in the input filter, as discussed in section 6.3.1. Thus, *K* is adjusted to achieve a good tradeoff between the suppression of grid current harmonic and the elimination of output current ripple.

Table 6.1 System Parameters

Parameter	Value
Power supply	$\mathbf{V_p} = 100\text{V}\angle 0^0, \mathbf{V_n} = 15\text{V}\angle 0^0, f_i = 60$ Hz
Input filter	$L_f = 1.2$ mH, $C_f = 20\ \mu$F, $R_f \approx 0\ \Omega$
Output	$L = 10$ mH, $R = 10\ \Omega$
MPC parameters	$T_s = 50\ \mu s,\ \lambda = 0.5$

6.4   Simulation Results

The effectiveness of the proposed I-MPC scheme is verified using simulation tests with PSIM. The P-NSCs of the grid voltage are set to $\mathbf{V_p}$=100V $\angle 0^o$ and $\mathbf{V_n}$=15V $\angle 0^o$ to generate an unbalanced degree of 15%. In the case of a balanced grid voltage, $\mathbf{V_n}$ = 0. The efficiency η is set to 1 in the simulations. Table 6.1 lists the parameters of the system.

Figure 6.5 shows the performance of the output and grid currents in the I-MPC scheme with resonant gain (K) values of 100, 10, and 2. The output current reference is 5A. With the biggest K value, the grid current THD is lowest, while the output current ripple is largest as shown in Figure 6.5(a). On the other hand, the output current ripple is significantly reduced with the smallest K, but this causes a high grid current distortion with a THD of over 5% as shown in Figure 6.5(c). Figure 6.5(b) shows that the proposed I-MPC scheme with a K value of 10 achieves a small output current ripple, while the grid current is kept sinusoidal with a THD below 5%. This result coincides with the theoretical analysis in section 3.2, which indicates that a higher K provides a lower grid current THD but a larger output current ripple. However, the system stability is less affected by the change of K even though the waveform quality is sensitive to the value of K. To achieve a good tradeoff between the output and grid current quality, the value of K is tuned finely by a trial and error method. With the same system parameters, a K value of 10 is selected and used for the next simulation.

Figure 6.6 shows steady-state waveforms of the existing MPC (Method 1) in [104],
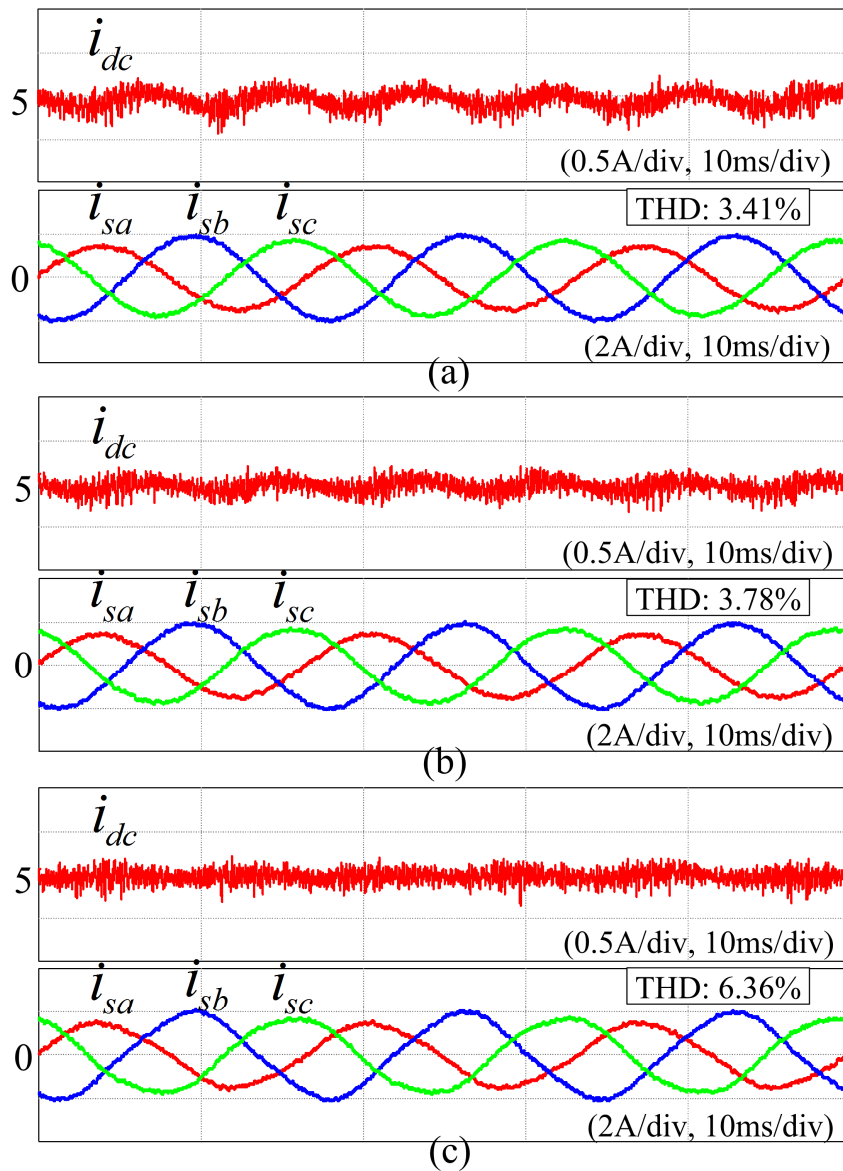
Figure 6.5 Influence of K on the output and grid currents: (a) $K = 100$; (b) $K = 10$; (c) $K = 2$.

MPC-PC (Method 2), and I-MPC schemes under unbalanced grid voltage conditions with an output current reference of 5A. Figure 6.6(a) illustrates that the Method 1 achieves a sinusoidal grid current with a THD of 3.32% since the grid current reference is sinusoidally generated in (6.6) by providing a ripple-free grid active power reference. However, the grid active power reference of the Method 1 is obtained by ignoring the power ripple in the input filter. Thus, the output current shows large ripple. The power ripple in the input filter is compensated in the Method 2 to provide ripple-free output current. In Figure 6.6(b), even though a ripple-free output current is achieved, the grid current becomes distorted with a THD of 7.13% since an oscillated grid active power reference is used to generate the grid
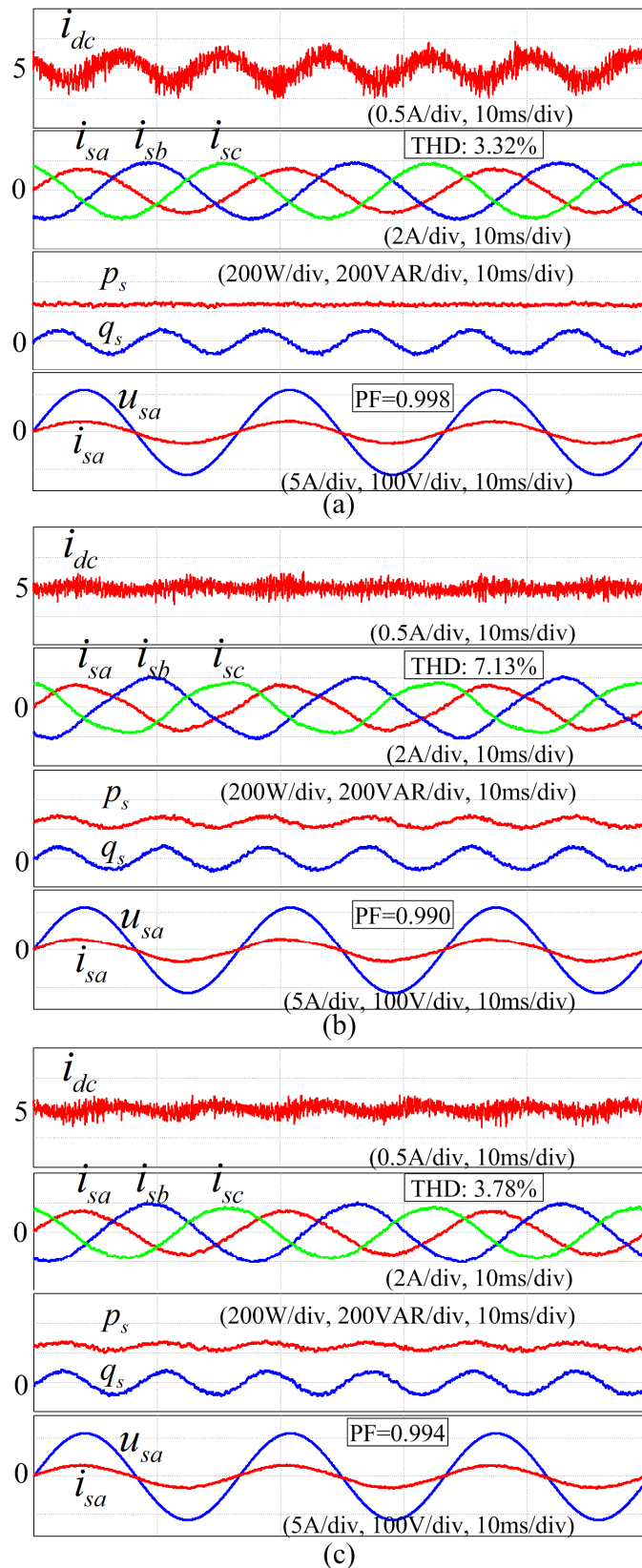
Figure 6.6 Simulated comparison of the output current, grid current, grid active and reactive power, phase-*a* grid current and voltage for different MPC schemes under unbalanced conditions: (a) Method 1, (b) Method 2, (c) I-MPC.
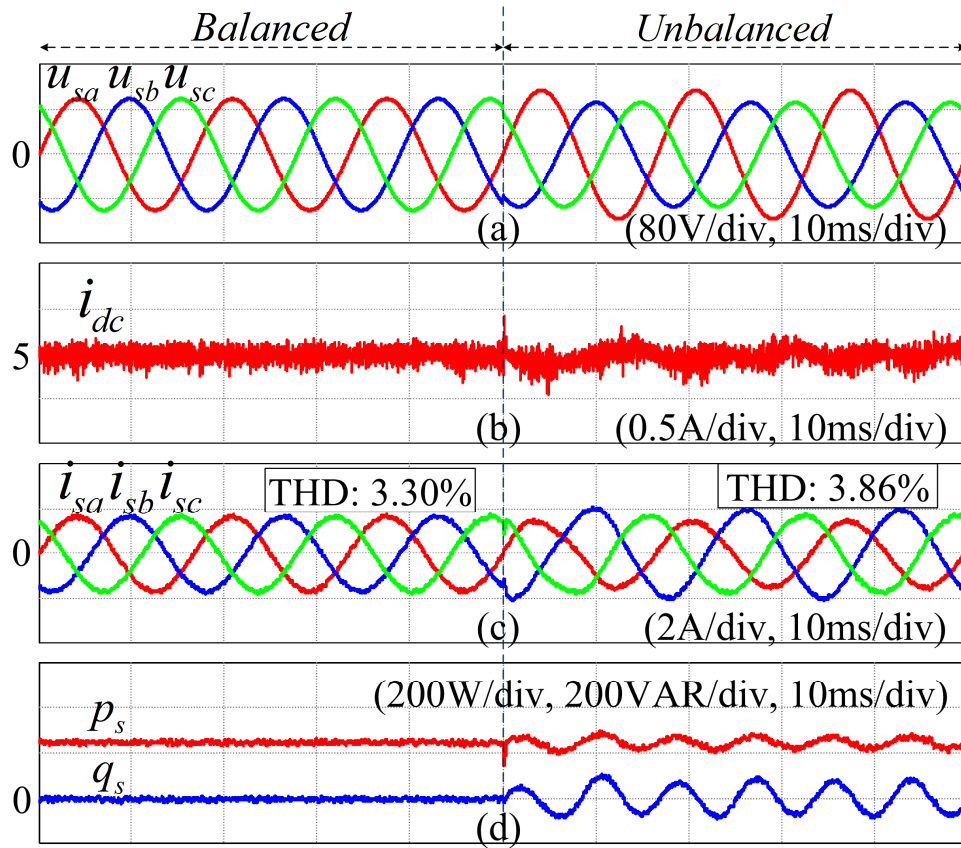
Figure 6.7 Simulated performance for the proposed I-MPC scheme: (a) grid voltage; (b) output current; (c) grid current; (d) grid active and reactive powers.

current reference in (6.24). Thanks to the closed-loop feedback controller, the harmonic distortion in the grid current reference is reduced, even though the power ripple in the input filter is compensated by the I-MPC scheme. As shown in Figure 6.6(c), the I-MPC scheme achieves a nearly sinusoidal grid current with a THD of 3.78%, which complies with IEEE Std 519 – 2014. In addition, the output current ripple is highly decreased when compared with that in the Method 1.

Figure 6.7 illustrates the dynamic response of the I-MPC scheme when the grid voltage changes from the balanced condition to the unbalanced condition at 0.05s. When the grid voltage is balanced, the I-MPC scheme achieves a ripple-free output current and a balanced sinusoidal grid current with a THD of 3.30%. Ripple-free grid active power is provided, and a unity grid power factor is achieved with zero grid reactive power. When the grid voltage is unbalanced, the proposed I-MPC can quickly achieve an almost sinusoidal grid current with a slightly increased THD of 3.86%, and the output current has small ripple. Moreover, a

near-unity input power is obtained with zero average grid reactive power. Thus, the proposed I-MPC scheme shows superior performance even when the grid voltage is unbalanced.

6.5   Experimental Results

Performance was also tested experimentally to verify the feasibility of the improved MPC scheme. The bidirectional switches are implemented by 2 discrete IGBTs (IRG4PF50WD) with a common-emitter connection, and the control system is based on a DSP (TMS320F28335) and a CPLD (EPM7128SLC84-15). A Chroma 61704 programmable AC source is utilized to provide an imbalanced grid voltage with P-NSCs of $\mathbf{V_p}$=100V$\angle 0^o$ and $\mathbf{V_n}$=15V$\angle 0^o$, which leads to an imbalanced degree of 15%. A PPA5530 Precision Power Analyzer was used to measure the THDs of the grid current and the grid power factor. The parameters of the experimental setup are listed in Table 1, and the efficiency η was empirically adjusted to 0.92 in the experimental tests.

Figure 6.8 shows experimental waveform of the proposed I-MPC scheme under balanced grid voltage conditions with an output current reference of 5A. In Figure 6.8(a), the output current is controlled to accurately track the given reference, and the grid current is sinusoidal with a low THD of 3.38%. In Figure 6.8(b), the grid current is kept almost in phase with the grid voltage, which results in a grid power factor of almost unity (0.994). The I-MPC scheme also provides ripple-free grid active power since the active power in the filter capacitor is zero under balanced grid voltage conditions, as demonstrated in (25). Therefore, it is confirmed that the proposed I-MPC scheme works effectively under balanced conditions.

Figure 6.9, Figure 6.10, and Figure 6.11 show comparisons of the Method 1, Method 2, and I-MPC schemes under unbalanced grid voltage conditions with an output current reference of 5A. Figure 6.9(a) shows that the Method 1 can achieve a sinusoidal grid current with a low THD of 3.43%. However, the output current ripple is large since the active power ripple in the input filter capacitor in Figure 6.9(c) is not considered to generate the grid
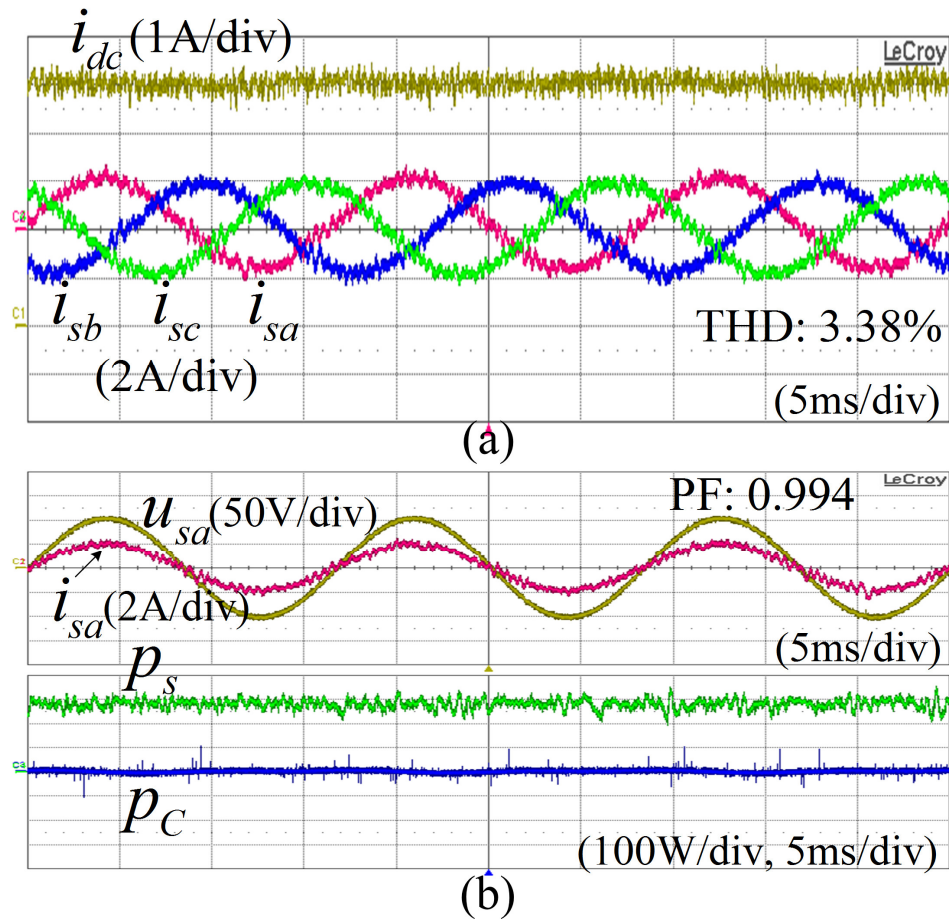
Figure 6.8 Experimental performance of the I-MPC scheme under balanced conditions: (a) output and grid currents; (b) phase-a grid current and voltage, grid active power and filter capacitor active power.

active power reference. The FFT analysis of the grid and output currents in Figure 6.9(b) clearly shows that the double-frequency component becomes significant in the output current spectrum. Figure 6.9(c) shows that an almost unity grid power factor (0.992) is obtained with zero average grid reactive power.

Figure 6.10 shows the performance of the Method 2. Thanks to the compensation of the power ripple in the input filter, the double-frequency current ripple is well suppressed in the output current as shown in Figure 6.10(a) and Figure 6.10(b). However, the power ripple compensation term results in the grid active power oscillating as shown in Figure 6.10(c), which results in a distorted grid current. In Figure 6.10(a) and Figure 6.10(b), the grid current THD increases to 7.41% since the third-order harmonic appears in the grid current spectrum, which does not comply with IEEE Std 519 − 2014.
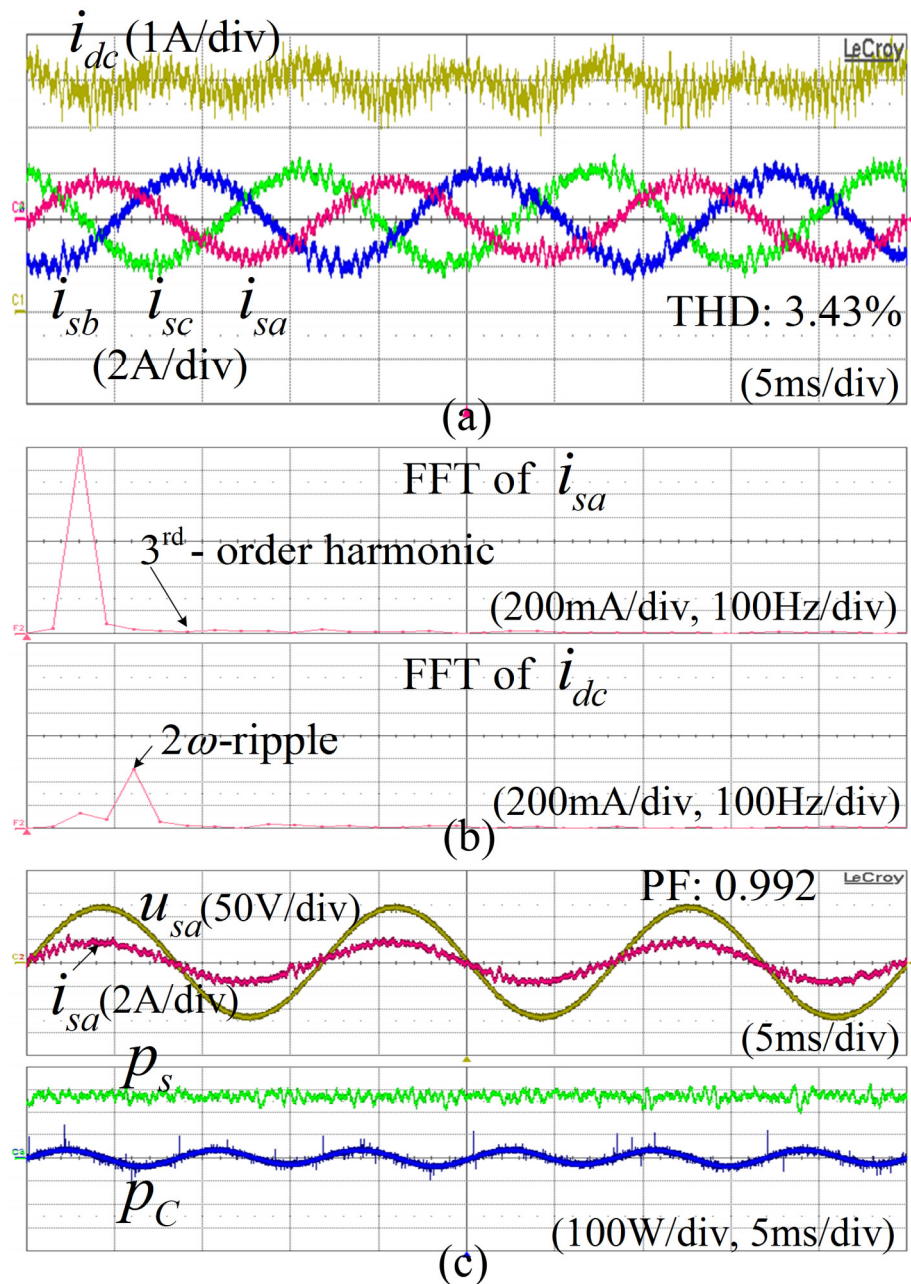
Figure 6.9 Experimental performance of the Method 1 under unbalanced conditions: (a) output and grid currents; (b) FFT of the grid phase-a and output currents; (c) phase-a grid current and voltage, grid active power and filter capacitor active power.

In Figure 6.10(c), the Method 2 provides zero average grid reactive power. However, the power factor is reduced to 0.980 due to the distorted grid current. The experimental performance of the proposed I-MPC scheme with $K=10$ is shown in Figure 6.11. Figure 6.11(a) and Figure 6.11(b) show that the I-MPC scheme keeps the grid current almost
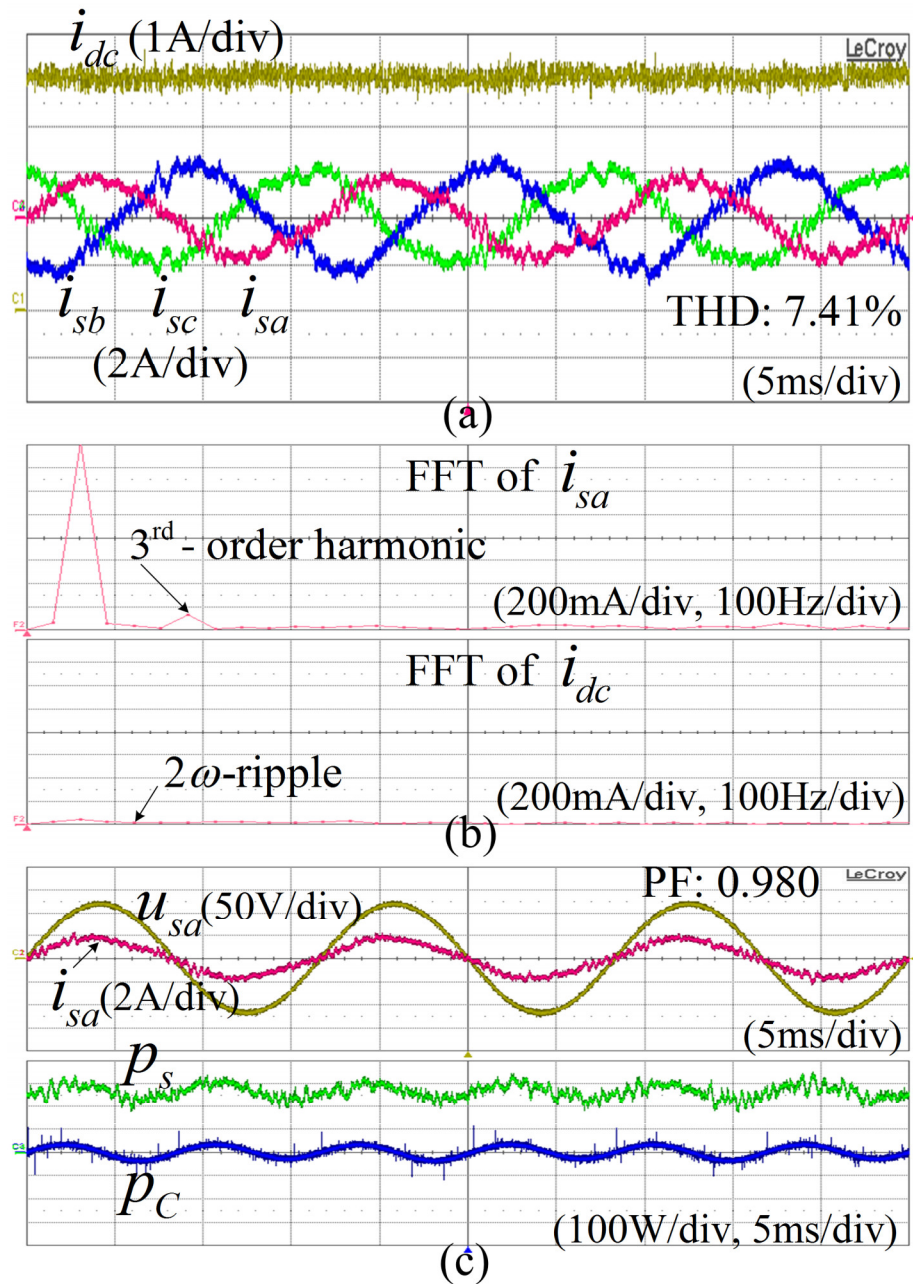
Figure 6.10 Experimental performance of the Method 2 under unbalanced conditions: (a) output and grid currents; (b) FFT of the grid phase-a and output currents; (c) phase-a grid current and voltage, grid active power and filter capacitor active power.

sinusoidal thanks to the feedback controller for grid current reference generation. In Figure 6.11(c), the grid active power of the I-MPC scheme has a lower ripple than that of the Method 2 in Figure 6.10(c), which contributes to reducing the grid current distortion and keeping the output current ripple small. Thus, the I-MPC scheme reduces the grid current
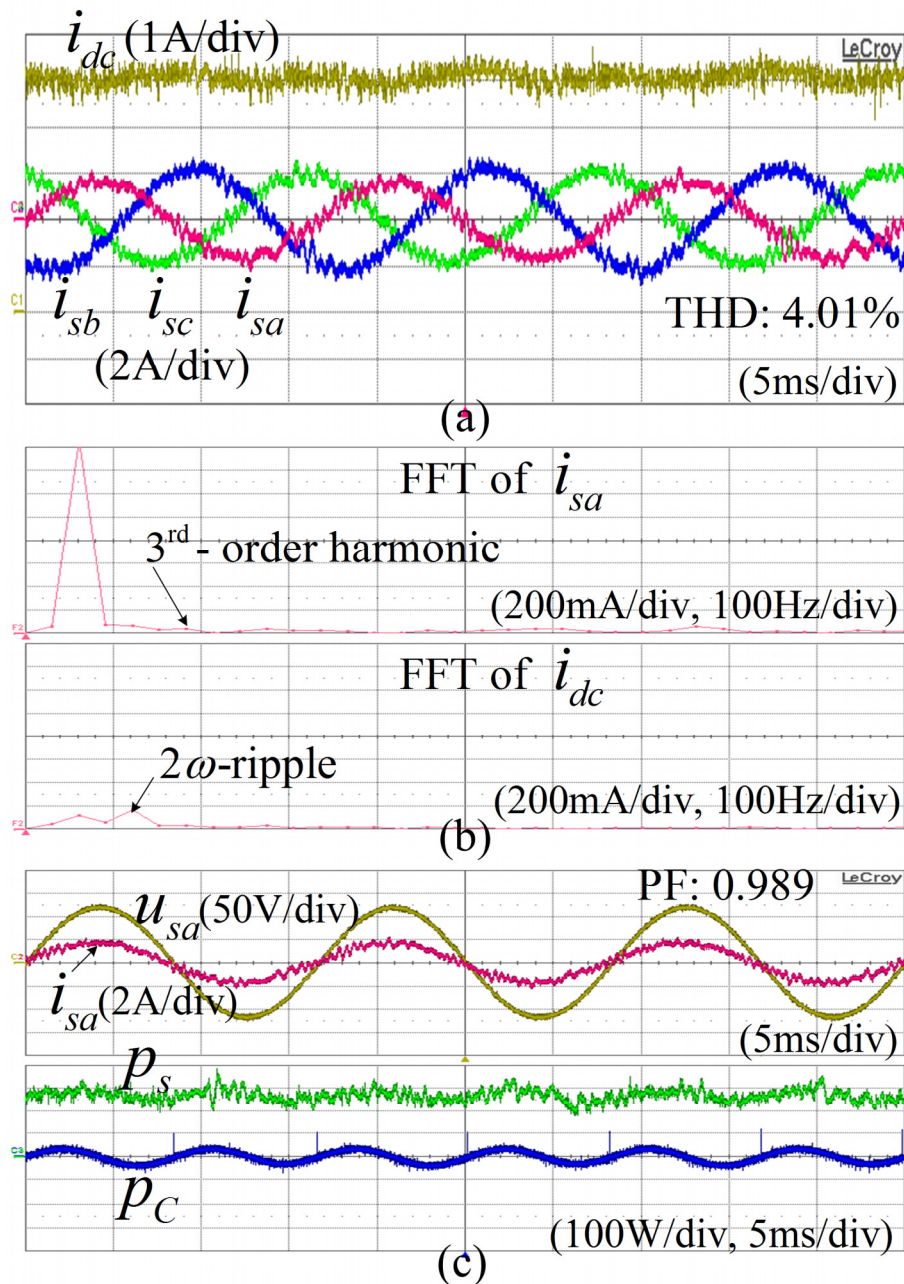
Figure 6.11 Experimental performance of the I-MPC scheme under unbalanced conditions: (a) output and grid currents; (b) FFT of the grid phase-a and output currents; (c) phase-a grid current and voltage, grid active power and filter capacitor active power.

THD to 4.01%, when compared to the Method 2, and this complies with IEEE Std 519 – 2014. The output current ripple is kept small in Figure 6.11(a) and it is reduced significantly when compared with that of the existing MPC scheme in Figure 6.10(a). In Figure 6.11(c), the grid current and voltage are almost in phase, which results in a high grid power factor of 0.989.
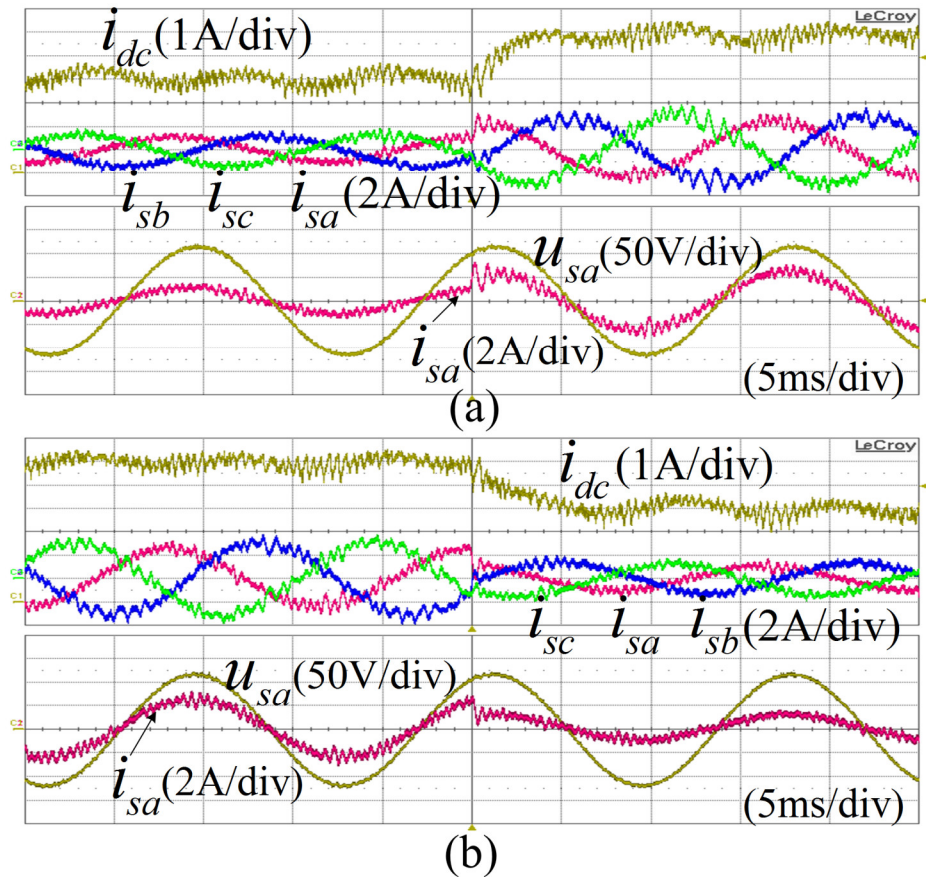
Figure 6.12 Dynamic responses of the Method 1 for output and grid currents, phase-*a* grid voltage and current with output current reference changing: (a) from 4 A to 6 A; (b) from 6 A to 4 A.

Figure 6.12 and Figure 6.13 show the dynamic responses for the Method 1 and the proposed I-MPC under imbalanced conditions. The output current reference increases from 4 A to 6 A and decreases from 6 A to 4 A. Despite the additional feedback controller for generating the grid current reference, the output and grid current responses of the I-MPC scheme are very fast when compared to those of the Method 1. Moreover, the I-MPC scheme achieves much smaller output current ripples in Figure 6.13 than the Method 1 in Figure 6.12. As shown in Figure 6.12 and Figure 6.13, the grid current is sinusoidal with both schemes, and a near-unity grid power factor is obtained. The experimental results verify the proposed scheme's effectiveness in reducing grid current distortion and output current ripple under grid voltage imbalance conditions.
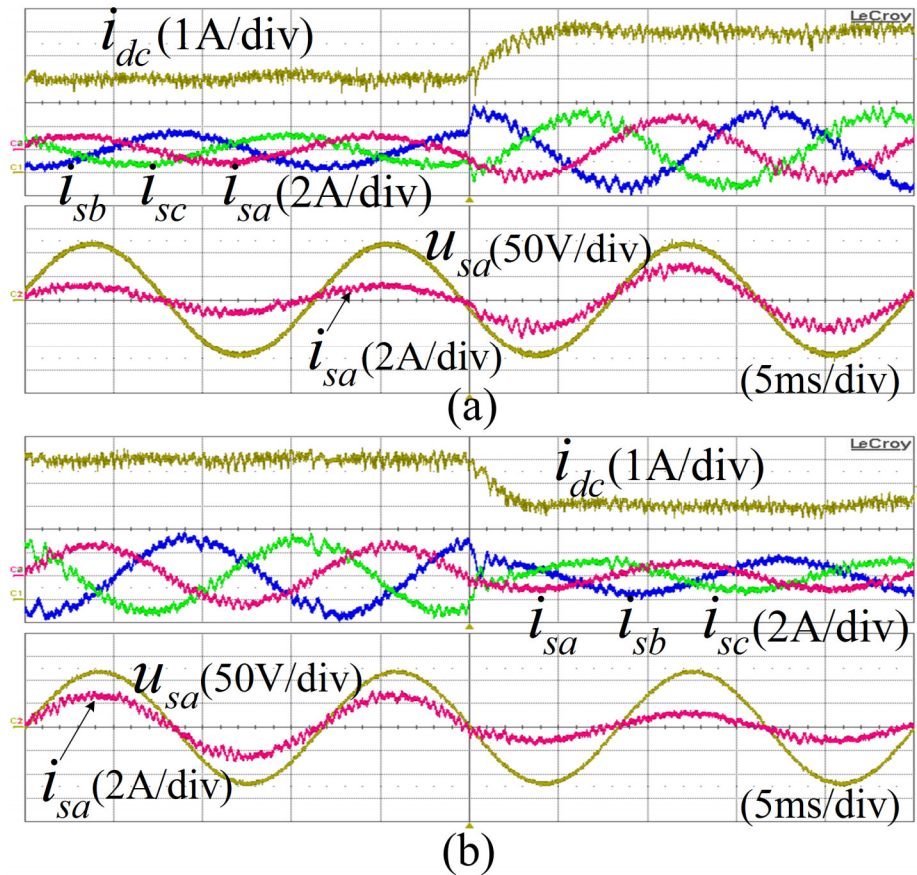
Figure 6.13 Dynamic responses of the I-MPC scheme for output and grid currents as well as the phase-*a* grid voltage and current with output current reference changing: (a) from 4 A to 6 A; (b) from 6 A to 4 A.

6.6   Summary

This chapter proposed an improved MPC scheme for an AC-DC MC by considering the power ripple in the input filter under grid voltage unbalanced conditions. The output current ripple and the grid current harmonic distortion are simultaneously reduced by the grid current controller. The power ripple is calculated based on the grid voltage and its 90 electrical degree delay signal, which are inherently detected for grid current reference generation. Therefore, the computational and control burdens are reduced when compared with previous methods. To reduce grid current distortion, a resonant controller was introduced in the feedback path of the grid current controller to reduce the harmonics in the

grid current reference of the MPC scheme. Simulation and experimental results verified that the grid current controller can effectively reduce grid current distortion and output current ripple without degrading the dynamic performance of the MPC scheme.

Chapter 7

Conclusions and Recommendations for Future Works

7.1   Conclusions

The unbalanced three-phase grid voltage occurs frequently due to various grid faults or disturbances. Unbalanced grid voltage gives rise to ripple on the DC side and low-order harmonics in the grid current, which severely deteriorate the performance of the AC-DC MCs. To solve these problems, this thesis has developed four advanced control strategies to drive the AC-DC MC with high performance in term of the output current and voltage ripples, grid current harmonics, and grid power factor under unbalanced grid voltage conditions. The proposed control strategies have been developed based on SVM and MPC. The achieved results in this thesis can be summarized as follows:

- Firstly, literature review of the research works on AC-DC MC and the frameworks as well as the objectives of this thesis have been presented in Chapter 1. In Chapter 2, the basic operation principles and the hardware implementation problems of the AC-DC MC have been presented.

- Continuously, Chapter 3 has presented an enhanced control strategy based on an independent control scheme for the active and reactive powers along with the SVM. The proposed control strategy achieves a constant DC voltage and current, a sinusoidal grid current, and a near unity grid power factor without using the grid voltage sequence components, so the proposed control strategy is implemented easily without large storage requirements. The main advantage of the control strategy based

on SVM is that the strict knowledge of system parameters is not required. Moreover, the switching frequency of SVM is fixed, which is beneficial to the filter design.

- Chapters 4 and 5 have presented two simplified MPC schemes to improve the steady-state performance of the grid current by shortening the sampling period and increasing the number of the current vectors, respectively. In addition, a novel method is developed to realize the active damping function without increasing the computational burden in Chapter 4. Furthermore, the VF-based grid voltage estimation technique is properly adopted in Chapter 5 to eliminate the grid voltage sensor in the MPC of AC-DC MC, which results in the volume and cost reduction and the system reliability improvement. Even though two simplified MPC schemes have higher switching losses, these two schemes are still effective when the high waveform quality is expected.

- Although a good performance can be achieved by two MPC schemes in Chapters 4 and 5, the effects of input filter power ripple in the output and grid current have not been fully addressed. Unfortunately, the power ripple compensation for ripple-free output current may cause grid current distortions. Chapter 6 has presented an improved MPC scheme to simultaneously compensate the input filter power ripple and reduce grid current distortions. The power ripple is calculated based on the grid voltage and its 90° lagging signal, which makes the implementation simple without grid voltage components extraction or digital filter design. In addition, a closed-loop current controller is developed to reduce the harmonic distortion of the grid current. The improved MPC scheme provides an effective way to flexibly control the output and grid current of AC-DC MC under unbalanced grid voltage conditions.

- The performance of the proposed control strategies have been verified by simulation in PSIM and experiments on a prototype AC-DC MC. The effectiveness of the proposed control strategies have also demonstrated by comparing with the conventional and other related control strategies.

According to the sistuation and control objective, an appropriate method should be selected to drive the AC-DC MC under unbalaced grid voltage conditions. A brief guideline is provided to select an appropriate method:

- When the exact system parameters are unknown, the SVM-based method in chapter

3 is the best selection.

▪ When the system parameters are known, the MPC-based methods is easy to implement.

▪ Thanks to the low computational burden, the method in chapter 4 improves the waveform quality by shortening the control period.

▪ The method in chapter 5 is an enhancement from the method in chapter 4. The features in chapter 4 are involved in chapter 5. In addition, chapter 5 presentes two more advanced features such as the number of voltage sensor is reduce by half, and the waveform quality is further improved by the proposed virtual current vector. However, the switching loss of the method in chapter 5 is higher than that in chapter 4. Thus, a trade-off between the low switching loss and the high quality waveform should be considered to select a proper method.

▪ The method in chapter 6 is an additional selection for the methods in chapter 4 and 5. Although the control complexity is increased, the method in chapter 6 provides a flexible capability to control the output current ripple and the grid current harmonics.

7.2 Recommendations for Future Works

Although unbalanced grid voltage problems have been successfully addressed in this thesis, three are some opportunities for extending the scope of this thesis in the future research. The following are some of attractive topics:

▪ Development a voltage sensorless MPC scheme to eliminate all voltage sensors in the input side of AC-DC MC.

▪ Development a robustness method to estimate the grid and input voltage for the MPC of AC-DC MC under unbalanced and distorted grid voltage conditions.

Bibliography

[1]   S. Vazquez, S. M. Lukic, E. Galvan, L. G. Franquelo, and J. M. Carrasco, "Energy Storage Systems for Transport and Grid Applications," *IEEE Trans. Ind. Electron.*, vol. 57, no. 12, pp. 3881–3895, 2010.

[2]   M. Parvez Akter, S. Mekhilef, N. Mei Lin Tan, and H. Akagi, "Modified Model Predictive Control of a Bidirectional AC–DC Converter Based on Lyapunov Function for Energy Storage Systems," *IEEE Trans. Ind. Electron.*, vol. 63, no. 2, pp. 704–715, 2016.

[3]   S. Haghbin, S. Lundmark, M. Alakula, and O. Carlson, "Grid-Connected Integrated Battery Chargers in Vehicle Applications: Review and New Solution," *IEEE Trans. Ind. Electron.*, vol. 60, no. 2, pp. 459–473, Feb. 2013.

[4]   M. Yilmaz and P. T. Krein, "Review of Battery Charger Topologies, Charging Power Levels, and Infrastructure for Plug-In Electric and Hybrid Vehicles," *IEEE Trans. Power Electron.*, vol. 28, no. 5, pp. 2151–2169, May 2013.

[5]   C. G. C. Branco, R. P. Torrico-Bascope, C. M. T. Cruz, and F. K. de A. Lima, "Proposal of Three-Phase High-Frequency Transformer Isolation UPS Topologies for Distributed Generation Applications," *IEEE Trans. Ind. Electron.*, vol. 60, no. 4, pp. 1520–1531, 2013.

[6]   P. Yang, Y. Xia, M. Yu, W. Wei, and Y. Peng, "A Decentralized Coordination Control Method for Parallel Bidirectional Power Converters in a Hybrid AC–DC Microgrid," *IEEE Trans. Ind. Electron.*, vol. 65, no. 8, pp. 6217–6228, Aug. 2018.

[7]   G. Buja, M. Bertoluzzo, and C. Fontana, "Reactive Power Compensation Capabilities of V2G-Enabled Electric Vehicles," *IEEE Trans. Power Electron.*, vol. 32, no. 12, pp. 9447–9459, Dec. 2017.

[8]   N. M. L. Tan, T. Abe, and H. Akagi, "Design and Performance of a Bidirectional Isolated DC-DC Converter for a Battery Energy Storage System," *IEEE Trans. Power Electron.*, vol. 27, no. 3, pp. 1237–1248, Mar. 2012.

[9] H. Wang and F. Blaabjerg, "Reliability of Capacitors for DC-Link Applications in Power Electronic Converters - An Overview," *IEEE Trans. Ind. Appl.*, vol. 50, no. 5, pp. 3569–3578, Sep. 2014.

[10] D. G. Holmes and T. A. Lipo, "Implementation of a controlled rectifier using AC-AC matrix converter theory," *IEEE Trans. Power Electron.*, vol. 7, no. 1, pp. 240–250, Jan. 1992.

[11] K. You, D. Xiao, M. F. Rahman, and M. N. Uddin, "Applying Reduced General Direct Space Vector Modulation Approach of AC-AC Matrix Converter Theory to Achieve Direct Power Factor Controlled Three-Phase AC-DC Matrix Rectifier," *IEEE Trans. Ind. Appl.*, vol. 50, no. 3, pp. 2243–2257, May 2014.

[12] T. Nguyen and H. Lee, "A Space Vector Modulation Method to Reduce Output Current Ripple at Unity Grid Power Factor for AC/DC Matrix Converters," in *IECON 2019 - 45th Annual Conference of the IEEE Industrial Electronics Society*, 2019, vol. 1, pp. 1561–1566.

[13] M. Su, H. Wang, Y. Sun, J. Yang, W. Xiong, and Y. Liu, "AC/DC Matrix Converter With an Optimized Modulation Strategy for V2G Applications," *IEEE Trans. Power Electron.*, vol. 28, no. 12, pp. 5736–5745, Dec. 2013.

[14] G. Rizzoli *et al.*, "Comparison between an AC-DC matrix converter and an interleaved DC-dc converter with power factor corrector for plug-in electric vehicles," in *2014 IEEE International Electric Vehicle Conference (IEVC)*, 2014, pp. 1–6.

[15] P. W. Wheeler, J. Rodriguez, J. C. Clare, L. Empringham, and A. Weinstein, "Matrix converters: a technology review," *IEEE Trans. Ind. Electron.*, vol. 49, no. 2, pp. 276–288, 2002.

[16] Laszlo Gyugyi and B. R. Pelly, *Static Power Frequency Changers: Theory, Performance, and Application*. Wiley, 1976.

[17] M. Venturini and A. Alesina, "The generalised transformer: A new bidirectional, sinusoidal waveform frequency converter with continuously adjustable input power factor," in *1980 IEEE Power Electronics Specialists Conference*, 1980, pp. 242–252.

[18]   A. Alesina and M. Venturini, "Solid-state power conversion: A Fourier analysis approach to generalized transformer synthesis," *IEEE Trans. Circuits Syst.*, vol. 28, no. 4, pp. 319–330, 1981.

[19]   S. Liu, Xiao; Zhang, Qingfan; Hou, Dianli; Wang, "Improved space vector modulation strategy for AC-DC matrix converters," *J. Power Electron.*, vol. 13, no. 4, pp. 647–655, 2013.

[20]   B. Feng, H. Lin, and X. Wang, "Modulation and control of ac/dc matrix converter for battery energy storage application," *IET Power Electron.*, vol. 8, no. 9, pp. 1583–1594, 2015.

[21]   H. Feng, Bo; Lin, "Finite Control Set Model Predictive Control of AC / DC Matrix Converter for Grid-Connected Battery Energy Storage Application," *J. Power Electron.*, vol. 15, no. 4, pp. 1006–1017, 2015.

[22]   A. K. Singh, E. Jeyasankar, P. Das, and S. K. Panda, "A Matrix-Based Nonisolated Three-Phase AC–DC Rectifier With Large Step-Down Voltage Gain," *IEEE Trans. Power Electron.*, vol. 32, no. 6, pp. 4796–4811, 2017.

[23]   K. You and M. F. Rahman, "A Matrix Z-Source Converter With AC-DC Bidirectional Power Flow for an Integrated Starter Alternator System," *IEEE Trans. Ind. Appl.*, vol. 45, no. 1, pp. 239–248, Jan. 2009.

[24]   K. You and F. Rahman, "Over-voltage protection using power Zener diode for matrix converter and matrix-Z-source converter," in *2009 International Conference on Power Electronics and Drive Systems (PEDS)*, 2009, pp. 193–197.

[25]   M. A. Sayed, K. Suzuki, T. Takeshita, and W. Kitagawa, "PWM Switching Technique for Three-Phase Bidirectional Grid-Tie DC–AC–AC Converter With High-Frequency Isolation," *IEEE Trans. Power Electron.*, vol. 33, no. 1, pp. 845–858, Jan. 2018.

[26]   S. Ratanapanachote, Han Ju Cha, and P. N. Enjeti, "A digitally controlled switch mode power supply based on matrix converter," *IEEE Trans. Power Electron.*, vol. 21, no. 1, pp. 124–130, Jan. 2006.

[27]   Z. Yan, K. Zhang, J. Li, and W. Wu, "A Novel Absolute Value Logic SPWM

Control Strategy Based on De-Re-Coupling Idea for High Frequency Link Matrix Rectifier," *IEEE Trans. Ind. Informatics*, vol. 9, no. 2, pp. 1188–1198, 2013.

[28] J. Afsharian, D. David Xu, B. Gong, and Z. Yang, "Space vector demonstration and analysis of zero-voltage switching transitions in three-phase isolated PWM rectifier," in *2015 IEEE Energy Conversion Congress and Exposition (ECCE)*, 2015, pp. 2477–2484.

[29] J. Afsharian, D. Xu, B. Wu, B. Gong, and Z. Yang, "The Optimal PWM Modulation and Commutation Scheme for a Three-Phase Isolated Buck Matrix-Type Rectifier," *IEEE Trans. Power Electron.*, vol. 33, no. 1, pp. 110–124, 2018.

[30] J. Afsharian, D. Xu, B. Wu, B. Gong, and Z. Yang, "A New PWM and Commutation Scheme for One Phase Loss Operation of Three-Phase Isolated Buck Matrix-Type Rectifier," *IEEE Trans. Power Electron.*, vol. 33, no. 11, pp. 9854–9865, 2018.

[31] D. Lan, P. Das, and S. K. Sahoo, "A High-Frequency Link Matrix Rectifier With a Pure Capacitive Output Filter in a Discontinuous Conduction Mode," *IEEE Trans. Ind. Electron.*, vol. 67, no. 1, pp. 4–15, 2020.

[32] A. R. Prabu, A. Sridhar, and N. Weise, "Bidirectional SiC three-phase AC-DC converter with DQ current control," in *2015 IEEE Energy Conversion Congress and Exposition (ECCE)*, 2015, pp. 3474–3481.

[33] M. A. Sayed, T. Takeshita, and W. Kitagawa, "Advanced PWM Switching Technique for Accurate Unity Power Factor of Bidirectional Three-Phase Grid-Tied DC–AC Converters," *IEEE Trans. Ind. Appl.*, vol. 55, no. 6, pp. 7614–7627, 2019.

[34] D. Das, N. Weise, K. Basu, R. Baranwal, and N. Mohan, "A Bidirectional Soft-Switched DAB-Based Single-Stage Three-Phase AC–DC Converter for V2G Application," *IEEE Trans. Transp. Electrif.*, vol. 5, no. 1, pp. 186–199, Mar. 2019.

[35] L. Schrittwieser, M. Leibl, and J. W. Kolar, "99% Efficient Isolated Three-Phase Matrix-Type DAB Buck–Boost PFC Rectifier," *IEEE Trans. Power Electron.*, vol. 35, no. 1, pp. 138–157, 2020.

[36] D. Sha and J. Chen, "Bidirectional three-phase high-frequency ac link dc–ac converter used for energy storage," *IET Power Electron.*, vol. 8, no. 12, pp. 2529–

2536, 2015.

[37] M. A. Sayed, K. Suzuki, T. Takeshita, and W. Kitagawa, "Soft-Switching PWM Technique for Grid-Tie Isolated Bidirectional DC–AC Converter With SiC Device," *IEEE Trans. Ind. Appl.*, vol. 53, no. 6, pp. 5602–5614, 2017.

[38] D. Varajão, R. E. Araújo, L. M. Miranda, and J. A. P. Lopes, "Modulation Strategy for a Single-Stage Bidirectional and Isolated AC–DC Matrix Converter for Energy Storage Systems," *IEEE Trans. Ind. Electron.*, vol. 65, no. 4, pp. 3458–3468, Apr. 2018.

[39] F. Fang and Y. W. Li, "Modulation and control method for bidirectional isolated AC/DC matrix based converter in hybrid AC/DC microgrid," in *2017 IEEE Energy Conversion Congress and Exposition (ECCE)*, 2017, pp. 37–43.

[40] M. Mengoni, L. Zarri, A. Tani, G. Rini, G. Serra, and D. Casadei, "Modulation strategy with minimum switching losses for three-phase AC-DC matrix converters," in *2014 16th European Conference on Power Electronics and Applications*, 2014, pp. 1–10.

[41] M. Mengoni, L. Zarri, A. Tani, G. Rizzoli, G. Serra, and D. Casadei, "Modulation strategies for three-phase AC-DC matrix converters: A comparison," in *2016 IEEE Energy Conversion Congress and Exposition (ECCE)*, 2016, pp. 1–7.

[42] F. Fang, H. Tian, and Y. Li, "An Improved SVM Strategy to Reduce DC Current Ripple for AC-DC Matrix Converter," in *2020 IEEE Applied Power Electronics Conference and Exposition (APEC)*, 2020, pp. 1929–1935.

[43] B. Feng, H. Lin, X. Wang, X. An, and B. Liu, "Optimal zero-vector configuration for space vector modulated AC-DC matrix converter," in *2012 IEEE Energy Conversion Congress and Exposition (ECCE)*, 2012, pp. 291–297.

[44] J. D. Zhu, Z. Xu, B. H. Jiang, and C. H. Zhang, "Close-loop control of an AC-DC matrix converter for automotives," in *2011 IEEE Electrical Power and Energy Conference*, 2011, pp. 426–431.

[45] X. Liu, Q. Zhang, and D. Hou, "One-Cycle Control Strategy with Active Damping for AC-DC Matrix Converter," *J. Power Electron.*, vol. 14, no. 4, pp. 778–787, 2014.

[46] Z. Wang, Y. Mao, Z. Hu, and Y. Xie, "A Sliding Mode Control Design based on the Reaching Law for Matrix Rectifiers," *J. Power Electron.*, vol. 16, no. 3, pp. 1122–1130, 2016.

[47] Z. Hu, W. Hu, Z. Wang, Y. Mao, and C. Hei, "Global Sliding Mode Control based on a Hyperbolic Tangent Function for Matrix Rectifier," *J. Power Electron.*, vol. 17, no. 4, pp. 991–1003, 2017.

[48] R. Metidji, B. Metidji, and B. Mendil, "Design and Implementation of a Unity Power Factor Fuzzy Battery Charger using an Ultrasparse Matrix Rectifier," *IEEE Trans. Power Electron.*, vol. 28, no. 5, pp. 2269–2276, May 2013.

[49] F. Fang, H. Tian, and Y. Li, "Finite Control Set Model Predictive Control for AC-DC Matrix Converter with Virtual Space Vectors," *IEEE J. Emerg. Sel. Top. Power Electron.*, p. 1, 2019.

[50] T. Nguyen, H. Nguyen, T. D. Nguyen, and H. Lee, "Simplified Model Predictive Control for AC/DC Matrix Converters with Fixed Switching Frequency," in *2019 10th International Conference on Power Electronics and ECCE Asia (ICPE 2019 - ECCE Asia)*, 2019, pp. 1–6.

[51] V. Vekhande, K. V. K., and B. G. Fernandes, "Control of Three-Phase Bidirectional Current-Source Converter to Inject Balanced Three-Phase Currents Under Unbalanced Grid Voltage Condition," *IEEE Trans. Power Electron.*, vol. 31, no. 9, pp. 6719–6737, 2016.

[52] T. L. Nguyen, T. D. Nguyen, and H. H. Lee, "Resonant compensators to suppress input current harmonics for AC/DC matrix converters under unbalanced input voltages," in *IECON 2017 - 43rd Annual Conference of the IEEE Industrial Electronics Society*, 2017, pp. 7354–7359.

[53] Zhiping Wang, Yunxiang Xie, and Yu Wang, "Feedback control strategy for matrix rectifier," in *Proceedings of The 7th International Power Electronics and Motion Control Conference*, 2012, vol. 3, pp. 2002–2006.

[54] D. Casadei, G. Serra, and A. Tani, "Reduction of the input current harmonic content in matrix converters under input/output unbalance," *IEEE Trans. Ind. Electron.*, vol.

45, no. 3, pp. 401–411, Jun. 1998.

[55] F. Blaabjerg, D. Casadei, C. Klumpner, and M. Matteini, "Comparison of two current modulation strategies for matrix converters under unbalanced input voltage conditions," *IEEE Trans. Ind. Electron.*, vol. 49, no. 2, pp. 289–296, Apr. 2002.

[56] X. Wang, H. Lin, H. She, and B. Feng, "A Research on Space Vector Modulation Strategy for Matrix Converter Under Abnormal Input-Voltage Conditions," *IEEE Trans. Ind. Electron.*, vol. 59, no. 1, pp. 93–104, Jan. 2012.

[57] Y. Yan, H. An, T. Shi, and C. Xia, "Improved double line voltage synthesis of matrix converter for input current enhancement under unbalanced power supply," *IET Power Electron.*, vol. 6, no. 4, pp. 798–808, Apr. 2013.

[58] J. D. Dasika and M. Saeedifard, "An Online Modulation Strategy to Control the Matrix Converter Under Unbalanced Input Conditions," *IEEE Trans. Power Electron.*, vol. 30, no. 8, pp. 4423–4436, Aug. 2015.

[59] J. Lei, B. Zhou, J. Bian, X. Qin, and J. Wei, "A Simple Method for Sinusoidal Input Currents of Matrix Converter Under Unbalanced Input Voltages," *IEEE Trans. Power Electron.*, vol. 31, no. 1, pp. 21–25, Jan. 2016.

[60] J. Lei *et al.*, "Feedback Control Strategy to Eliminate the Input Current Harmonics of Matrix Converter Under Unbalanced Input Voltages," *IEEE Trans. Power Electron.*, vol. 32, no. 1, pp. 878–888, Jan. 2017.

[61] P. Wheeler and D. Grant, "Optimised input filter design and low-loss switching techniques for a practical matrix converter," *IEE Proc. - Electr. Power Appl.*, vol. 144, no. 1, pp. 53–60, 1997.

[62] T. Kume *et al.*, "Integrated Filters and Their Combined Effects in Matrix Converter," *IEEE Trans. Ind. Appl.*, vol. 43, no. 2, pp. 571–581, 2007.

[63] H. She, H. Lin, X. Wang, and L. Yue, "Damped input filter design of matrix converter," in *2009 International Conference on Power Electronics and Drive Systems (PEDS)*, 2009, pp. 672–677.

[64] A. Dasgupta and P. Sensarma, "An integrated filter and controller design for direct

matrix converter," in *2011 IEEE Energy Conversion Congress and Exposition*, 2011, pp. 814–821.

[65] A. Dasgupta and P. Sensarma, "Filter Design of Direct Matrix Converter for Synchronous Applications," *IEEE Trans. Ind. Electron.*, vol. 61, no. 12, pp. 6483–6493, 2014.

[66] A. K. Sahoo, K. Basu, and N. Mohan, "Systematic Input Filter Design of Matrix Converter by Analytical Estimation of RMS Current Ripple," *IEEE Trans. Ind. Electron.*, vol. 62, no. 1, pp. 132–143, 2015.

[67] M. Rivera, C. Rojas, J. Rodríguez, P. Wheeler, B. Wu, and J. Espinoza, "Predictive Current Control With Input Filter Resonance Mitigation for a Direct Matrix Converter," *IEEE Trans. Power Electron.*, vol. 26, no. 10, pp. 2794–2803, Oct. 2011.

[68] M. Rivera, J. Rodriguez, B. Wu, J. R. Espinoza, and C. A. Rojas, "Current Control for an Indirect Matrix Converter With Filter Resonance Mitigation," *IEEE Trans. Ind. Electron.*, vol. 59, no. 1, pp. 71–79, Jan. 2012.

[69] J. Lei *et al.*, "Predictive Power Control of Matrix Converter With Active Damping Function," *IEEE Trans. Ind. Electron.*, vol. 63, no. 7, pp. 4550–4559, Jul. 2016.

[70] H. Gao, B. Wu, D. Xu, M. Pande, and R. P. Aguilera, "Model predictive control scheme with active damping function for current source rectifiers," *IET Power Electron.*, vol. 10, no. 7, pp. 717–725, 2017.

[71] H. Gao, B. Wu, D. Xu, and N. R. Zargari, "A Model Predictive Power Factor Control Scheme With Active Damping Function for Current Source Rectifiers," *IEEE Trans. Power Electron.*, vol. 33, no. 3, pp. 2655–2667, Mar. 2018.

[72] L. Empringham, J. W. Kolar, J. Rodriguez, P. W. Wheeler, and J. C. Clare, "Technological Issues and Industrial Application of Matrix Converters: A Review," *IEEE Trans. Ind. Electron.*, vol. 60, no. 10, pp. 4260–4271, 2013.

[73] J. Mahlein, J. Igney, J. Weigold, M. Braun, and O. Simon, "Matrix converter commutation strategies with and without explicit input voltage sign measurement," *IEEE Trans. Ind. Electron.*, vol. 49, no. 2, pp. 407–414, 2002.

[74]   K. Kato and J. Itoh, "Improvement of Input Current Waveforms for a Matrix Converter Using a Novel Hybrid Commutation Method," in *2007 Power Conversion Conference - Nagoya*, 2007, pp. 763–768.

[75]   H. She, H. Lin, B. He, X. Wang, L. Yue, and X. An, "Implementation of Voltage-Based Commutation in Space-Vector-Modulated Matrix Converter," *IEEE Trans. Ind. Electron.*, vol. 59, no. 1, pp. 154–166, 2012.

[76]   H. Nguyen and H. Lee, "A Modulation Scheme for Matrix Converters With Perfect Zero Common-Mode Voltage," *IEEE Trans. Power Electron.*, vol. 31, no. 8, pp. 5411–5422, 2016.

[77]   Nguyen Huu Nhan, "High Performance Space Vector Modulation Techniques for Matrix Converters," Ph.D. Thesis, University of Ulsan, 2017.

[78]   P. Nielsen, F. Blaabjerg, and J. K. Pedersen, "Space vector modulated matrix converter with minimized number of switchings and a feedforward compensation of input voltage unbalance," in *Proceedings of International Conference on Power Electronics, Drives and Energy Systems for Industrial Growth*, 1996, vol. 2, pp. 833–839 vol.2.

[79]   M. Hamouda, H. F. Blanchette, and K. Al-Haddad, "Unity Power Factor Operation of Indirect Matrix Converter Tied to Unbalanced Grid," *IEEE Trans. Power Electron.*, vol. 31, no. 2, pp. 1095–1107, Feb. 2016.

[80]   Z. Li, Y. Li, P. Wang, H. Zhu, C. Liu, and W. Xu, "Control of Three-Phase Boost-Type PWM Rectifier in Stationary Frame Under Unbalanced Input Voltage," *IEEE Trans. Power Electron.*, vol. 25, no. 10, pp. 2521–2530, Oct. 2010.

[81]   Y. Zhang, J. Gao, and C. Qu, "Relationship Between Two Direct Power Control Methods for PWM Rectifiers Under Unbalanced Network," *IEEE Trans. Power Electron.*, vol. 32, no. 5, pp. 4084–4094, May 2017.

[82]   P. Rodriguez, A. V Timbus, R. Teodorescu, M. Liserre, and F. Blaabjerg, "Flexible Active Power Control of Distributed Power Generation Systems During Grid Faults," *IEEE Trans. Ind. Electron.*, vol. 54, no. 5, pp. 2583–2592, Oct. 2007.

[83]   "IEEE Recommended Practice and Requirements for Harmonic Control in Electric

Power Systems," *IEEE Std 519-2014 (Revision IEEE Std 519-1992)*, pp. 1–29, Jun. 2014.

[84] P. Cortes, M. P. Kazmierkowski, R. M. Kennel, D. E. Quevedo, and J. Rodriguez, "Predictive Control in Power Electronics and Drives," *IEEE Trans. Ind. Electron.*, vol. 55, no. 12, pp. 4312–4324, 2008.

[85] S. Kouro, P. Cortes, R. Vargas, U. Ammann, and J. Rodriguez, "Model Predictive Control—A Simple and Powerful Method to Control Power Converters," *IEEE Trans. Ind. Electron.*, vol. 56, no. 6, pp. 1826–1838, Jun. 2009.

[86] M. Gokdag and O. Gulbudak, "Model predictive control of AC-DC matrix converter with unity input power factor," in *2018 IEEE 12th International Conference on Compatibility, Power Electronics and Power Engineering (CPE-POWERENG 2018)*, 2018, pp. 1–5.

[87] H. Dan, Q. Zhu, T. Peng, S. Yao, and P. Wheeler, "Preselection algorithm based on predictive control for direct matrix converter," *IET Electr. Power Appl.*, vol. 11, no. 5, pp. 768–775, 2017.

[88] M. Siami, D. A. Khaburi, M. Rivera, and J. Rodríguez, "A Computationally Efficient Lookup Table Based FCS-MPC for PMSM Drives Fed by Matrix Converters," *IEEE Trans. Ind. Electron.*, vol. 64, no. 10, pp. 7645–7654, Oct. 2017.

[89] C. Xia, T. Liu, T. Shi, and Z. Song, "A Simplified Finite-Control-Set Model-Predictive Control for Power Converters," *IEEE Trans. Ind. Informatics*, vol. 10, no. 2, pp. 991–1002, May 2014.

[90] M. Siami, D. A. Khaburi, and J. Rodriguez, "Simplified Finite Control Set-Model Predictive Control for Matrix Converter-Fed PMSM Drives," *IEEE Trans. Power Electron.*, vol. 33, no. 3, pp. 2438–2446, Mar. 2018.

[91] M. Siami, M. Amiri, H. K. Savadkuhi, R. Rezavandi, and S. Valipour, "Simplified Predictive Torque Control for a PMSM Drive Fed by a Matrix Converter with imposed input current," *IEEE J. Emerg. Sel. Top. Power Electron.*, p. 1, 2018.

[92] Q. Trinh and H. Lee, "An Advanced Current Control Strategy for Three-Phase Shunt Active Power Filters," *IEEE Trans. Ind. Electron.*, vol. 60, no. 12, pp. 5400–5410,

Dec. 2013.

[93] M. Rivera, C. Rojas, J. Rodriguez, and J. Espinoza, "Methods of source current reference generation for predictive control in a direct matrix converter," *IET Power Electron.*, vol. 6, no. 5, pp. 894–901, May 2013.

[94] M. Rivera, C. Uribe, L. Tarisciotti, P. Wheeler, and P. Zanchetta, "Predictive control of an indirect matrix converter operating at fixed switching frequency and unbalanced AC-supply," in *2015 IEEE International Symposium on Predictive Control of Electrical Drives and Power Electronics (PRECEDE)*, 2015, pp. 38–43.

[95] C. Rojas *et al.*, "Predictive control of a direct matrix converter operating under an unbalanced AC source," in *2010 IEEE International Symposium on Industrial Electronics*, 2010, pp. 3159–3164.

[96] P. Cortes, J. Rodriguez, C. Silva, and A. Flores, "Delay Compensation in Model Predictive Current Control of a Three-Phase Inverter," *IEEE Trans. Ind. Electron.*, vol. 59, no. 2, pp. 1323–1325, Feb. 2012.

[97] X. Guo, W. Liu, and Z. Lu, "Flexible Power Regulation and Current-Limited Control of the Grid-Connected Inverter Under Unbalanced Grid Voltage Faults," *IEEE Trans. Ind. Electron.*, vol. 64, no. 9, pp. 7425–7432, Sep. 2017.

[98] H. Dehghani Tafti, A. I. Maswood, G. Konstantinou, J. Pou, and P. Acuna, "Active/reactive power control of photovoltaic grid-tied inverters with peak current limitation and zero active power oscillation during unbalanced voltage sags," *IET Power Electron.*, vol. 11, no. 6, pp. 1066–1073, 2018.

[99] A. Camacho, M. Castilla, J. Miret, A. Borrell, and L. G. de Vicuña, "Active and Reactive Power Strategies With Peak Current Limitation for Distributed Generation Inverters During Unbalanced Grid Faults," *IEEE Trans. Ind. Electron.*, vol. 62, no. 3, pp. 1515–1525, 2015.

[100] M. M. Shabestary and Y. A. I. Mohamed, "An Analytical Method to Obtain Maximum Allowable Grid Support by Using Grid-Connected Converters," *IEEE Trans. Sustain. Energy*, vol. 7, no. 4, pp. 1558–1571, 2016.

[101] R. Vargas, U. Ammann, and J. Rodríguez, "Predictive Approach to Increase

Efficiency and Reduce Switching Losses on Matrix Converters," *IEEE Trans. Power Electron.*, vol. 24, no. 4, pp. 894–902, 2009.

[102] M. Rivera, J. Rodriguez, J. R. Espinoza, and H. Abu-Rub, "Instantaneous Reactive Power Minimization and Current Control for an Indirect Matrix Converter Under a Distorted AC Supply," *IEEE Trans. Ind. Informatics*, vol. 8, no. 3, pp. 482–490, Aug. 2012.

[103] J. Lei, S. Feng, P. Wheeler, B. Zhou, and J. Zhao, "Steady-State Error Suppression and Simplified Implementation of Direct Source Current Control for Matrix Converter With Model Predictive Control," *IEEE Trans. Power Electron.*, vol. 35, no. 3, pp. 3183–3194, 2020.

[104] T. Nguyen and H. Lee, "Simplified Model Predictive Control for AC/DC Matrix Converters With Active Damping Function Under Unbalanced Grid Voltage," *IEEE J. Emerg. Sel. Top. Power Electron.*, vol. 8, no. 3, pp. 2907–2917, 2020.

[105] M. Vijayagopal, P. Zanchetta, L. Empringham, L. de Lillo, L. Tarisciotti, and P. Wheeler, "Control of a Direct Matrix Converter With Modulated Model-Predictive Control," *IEEE Trans. Ind. Appl.*, vol. 53, no. 3, pp. 2342–2349, May 2017.

[106] L. Tarisciotti *et al.*, "Modulated Predictive Control for Indirect Matrix Converter," *IEEE Trans. Ind. Appl.*, vol. 53, no. 5, pp. 4644–4654, Sep. 2017.

[107] M. Malinowski, M. P. Kazmierkowski, S. Hansen, F. Blaabjerg, and G. D. Marques, "Virtual-flux-based direct power control of three-phase PWM rectifiers," *IEEE Trans. Ind. Appl.*, vol. 37, no. 4, pp. 1019–1027, Jul. 2001.

[108] L. A. Serpa, S. Ponnaluri, P. M. Barbosa, and J. W. Kolar, "A Modified Direct Power Control Strategy Allowing the Connection of Three-Phase Inverters to the Grid Through LCL Filters," *IEEE Trans. Ind. Appl.*, vol. 43, no. 5, pp. 1388–1400, 2007.

[109] J. G. Norniella *et al.*, "Improving the Dynamics of Virtual-Flux-Based Control of Three-Phase Active Rectifiers," *IEEE Trans. Ind. Electron.*, vol. 61, no. 1, pp. 177–187, Jan. 2014.

[110] Y. Cho and K. Lee, "Virtual-Flux-Based Predictive Direct Power Control of Three-

Phase PWM Rectifiers With Fast Dynamic Response," *IEEE Trans. Power Electron.*, vol. 31, no. 4, pp. 3348–3359, Apr. 2016.

[111] H. Li, M. Lin, M. Yin, J. Ai, and W. Le, "Three-Vector-Based Low-Complexity Model Predictive Direct Power Control Strategy for PWM Rectifier Without Voltage Sensors," *IEEE J. Emerg. Sel. Top. Power Electron.*, vol. 7, no. 1, pp. 240–251, Mar. 2019.

[112] M. Cichowlas, M. Malinowski, M. P. Kazmierkowski, D. L. Sobczuk, P. Rodriguez, and J. Pou, "Active filtering function of three-phase PWM boost rectifier under different line voltage conditions," *IEEE Trans. Ind. Electron.*, vol. 52, no. 2, pp. 410–419, Apr. 2005.

[113] J. A. Suul, A. Luna, P. Rodríguez, and T. Undeland, "Virtual-Flux-Based Voltage-Sensor-Less Power Control for Unbalanced Grid Conditions," *IEEE Trans. Power Electron.*, vol. 27, no. 9, pp. 4071–4087, Sep. 2012.

[114] J. A. Suul, A. Luna, P. Rodriguez, and T. Undeland, "Voltage-Sensor-Less Synchronization to Unbalanced Grids by Frequency-Adaptive Virtual Flux Estimation," *IEEE Trans. Ind. Electron.*, vol. 59, no. 7, pp. 2910–2923, Jul. 2012.

[115] D. Casadei, G. Serra, and K. Tani, "Implementation of a direct control algorithm for induction motors based on discrete space vector modulation," *IEEE Trans. Power Electron.*, vol. 15, no. 4, pp. 769–777, Jul. 2000.

[116] H. Moon, J. Lee, and K. Lee, "A Robust Deadbeat Finite Set Model Predictive Current Control Based on Discrete Space Vector Modulation for a Grid-Connected Voltage Source Inverter," *IEEE Trans. Energy Convers.*, vol. 33, no. 4, pp. 1719–1728, 2018.

[117] J. Lee, J. Lee, H. Moon, and K. Lee, "An Improved Finite-Set Model Predictive Control Based on Discrete Space Vector Modulation Methods for Grid-Connected Three-Level Voltage Source Inverter," *IEEE J. Emerg. Sel. Top. Power Electron.*, vol. 6, no. 4, pp. 1744–1760, Dec. 2018.

[118] T. He, J. Zhu, D. D. Lu, and L. Zheng, "Modified Model Predictive Control for Bidirectional Four-Quadrant EV Chargers With Extended Set of Voltage Vectors,"

IEEE J. Emerg. Sel. Top. Power Electron., vol. 7, no. 1, pp. 274–281, Mar. 2019.

[119] Y. Zhang, J. Liu, H. Yang, and J. Gao, "Direct Power Control of Pulsewidth Modulated Rectifiers Without DC Voltage Oscillations Under Unbalanced Grid Conditions," *IEEE Trans. Ind. Electron.*, vol. 65, no. 10, pp. 7900–7910, Oct. 2018.

[120] Y. Zhang, J. Jiao, and J. Liu, "Direct Power Control of PWM Rectifiers With Online Inductance Identification Under Unbalanced and Distorted Network Conditions," *IEEE Trans. Power Electron.*, vol. 34, no. 12, pp. 12524–12537, Dec. 2019.

[121] Y. Zhang, J. Jiao, J. Liu, and J. Gao, "Direct Power Control of PWM Rectifier With Feedforward Compensation of DC-Bus Voltage Ripple Under Unbalanced Grid Conditions," *IEEE Trans. Ind. Appl.*, vol. 55, no. 3, pp. 2890–2901, May 2019.

[122] Z. Wang, B. Wu, D. Xu, M. Cheng, and L. Xu, "DC-Link Current Ripple Mitigation for Current-Source Grid-Connected Converters Under Unbalanced Grid Conditions," *IEEE Trans. Ind. Electron.*, vol. 63, no. 8, pp. 4967–4977, Aug. 2016.

[123] S. Feng, J. Lei, J. Zhao, W. Chen, and F. Deng, "Improved Reference Generation of Active and Reactive Power for Matrix Converter With Model Predictive Control Under Input Disturbances," *IEEE Access*, vol. 7, pp. 97001–97012, 2019.

[124] N. Jin, C. Gan, and L. Guo, "Predictive Control of Bidirectional Voltage Source Converter With Reduced Current Harmonics and Flexible Power Regulation Under Unbalanced Grid," *IEEE Trans. Energy Convers.*, vol. 33, no. 3, pp. 1118–1131, 2018.

Publications

Journal papers

[J1]   **Thanh-Luan Nguyen** and Hong-Hee Lee, "An Enhanced Control Strategy for AC–DC Matrix Converters under Unbalanced Grid Voltage," *IEEE Transactions on Industrial Electronics,* vol. 67, no. 3, pp. 1718–1727, Mar. 2020.

[J2]   **Thanh-Luan Nguyen** and Hong-Hee Lee, "Simplified Model Predictive Control for AC/DC Matrix Converters with Active Damping Function under Unbalanced Grid Voltage," *IEEE Journal of Emerging and Selected Topics in Power Electronics,* vol. 8, no. 3, Sep. 2020.

[J3]   **Thanh-Luan Nguyen** and Hong-Hee Lee, "Improved Model Predictive Control Scheme for AC/DC Matrix Converter by Considering Input Filter Power Ripple under Imbalanced Grid Voltage Conditions," *Journal of Power Electronics,* p. 1, 2020.

[J4]   **Thanh-Luan Nguyen** and Hong-Hee Lee, "Grid Voltage Sensorless Model Predictive Control with Virtual Current Vectors for AC/DC Matrix Converters under Unbalanced Grid Voltages," *IEEE Transactions on Transportation Electrification*, 2020 (*under review*).

Conference papers

[C1] **Thanh-Luan Nguyen**, and Hong-Hee Lee, "Flexible Source Current Reference Generation for Predictive Current Control of Matrix Converter under Unbalanced Input Voltages," *2016 Power Electronics Annual Conference* (KIPE 2012), South Korea, pp. 359-360, July 2016.

[C2] **Thanh-Luan Nguyen**, Hong-Hee Lee, and Tae-Won Chun, "A simplified predictive current control for matrix converters with reduced common-mode voltage," in *Proc. 2nd World Congress on Electrical Engineering and Computer Systems and Science* (EECSS'16), Budapest, Hungary – August 16 – 17, 2016.

[C3] **Thanh-Luan Nguyen**, and Hong-Hee Lee, "A Control Strategy to Reduce the Input Current Harmonics of AC/DC Matrix Converter under Unbalanced Input Voltages," in *Proceedings of International Forum on Strategic Technology* (IFOST), Ulsan, Korea, May 2017.

[C4] **Thanh-Luan Nguyen**, Hong-Hee Lee, "A predictive current control for coordinate control of current and power of matrix converter under unbalanced input voltages", in *Proc. 4th International Conference on Mobile and Wireless Technology* (ICMWT), pp. 528-538, Jun. 2017.

[C5] **Thanh-Luan Nguyen**, Dinh-Tuyen Nguyen, and Hong-Hee Lee, "Resonant compensators to suppress input current harmonics for AC/DC matrix converters under unbalanced input voltages," in *IECON 2017 - 43rd Annual Conference of the IEEE Industrial Electronics Society*, 2017, pp. 7354–7359.

[C6] **Thanh-Luan Nguyen**, and Hong-Hee Lee, "A Control Strategy to Obtain Sinusoidal Input Currents of Matrix Converter under Unbalanced Input Voltages," *2018 Power Electronics Annual Conference* (KIPE 2018*)*, Korea, pp. 114-116, July 2018.

[C7] **Thanh-Luan Nguyen**, Huu-Nhan Nguyen, Dinh-Tuyen Nguyen, and Hong-Hee Lee, "Simplified Model Predictive Control for AC/DC Matrix Converters with Fixed Switching Frequency," in *2019 10th International Conference on Power Electronics - ECCE Asia* (ICPE 2019 - ECCE Asia), 2019, pp. 1–6.

[C8] Huu-Nhan Nguyen, Dinh-Tuyen Nguyen, **Thanh-Luan Nguyen**, and Hong-Hee Lee, "A Simple SVM Technique to Eliminate Common-mode Voltage for Matrix Converters," in *2019 10th International Conference on Power Electronics - ECCE Asia* (ICPE 2019 - ECCE Asia), 2019, pp. 2290-2295.

[C9] **Thanh-Luan Nguyen**, and Hong-Hee Lee, "A Space Vector Modulation Method to Reduce Output Current Ripple at Unity Grid Power Factor for AC/DC Matrix Converters," in *IECON 2019 - 45rd Annual Conference of the IEEE Industrial Electronics Society*, 2019, pp. 1561-1566.

[C10] **Thanh-Luan Nguyen**, Huu-Cong Vu, Quoc-Hoan Tran and Hong-Hee Lee, "Voltage Sensorless Model Predictive Control of AC/DC Matrix Converters," in *2020 11th International Conference on Power Electronics - ECCE Asia* (IPEMC 2020 - ECCE Asia), 2020.